Spatial Resolution of Equatorial Plasma Depletions Using Variable-Range Time-Delay Integration

Andrew Webster Napiecek

Thesis submitted to the Faculty of the
Virginia Polytechnic Institute and State University
in partial fulfillment of requirements for the degree of

Master of Science
In
Aerospace Engineering

Scott L. England, Committee Chair
Jonathan Black
Bhuvana Srinivasan

April 24, 2019
Blacksburg, Virginia

Keywords: Time-Delay Integration, Plasma Bubbles, Plasma Imaging

Spatial Resolution of Equatorial Plasma Depletions Using Variable-Range Time-Delay Integration

Andrew Webster Napiecek

ABSTRACT

Previous plasma imaging missions have used time-delay integration techniques that correct for uniform motion blur during integration. This was due to the assumed constant range-to-target of each pixel in the observed scene. ICON's low orbital altitude and twelve second integration time create non-uniform motion blur across the observed scene and necessitate a novel variable-range time-delay integration (TDI) algorithm be used to spatially resolve the two-dimensional images. The variable-range TDI algorithm corrects for each pixel moving at a different angular rate throughout image integration and transforms each raw image onto a surface where the spacecraft is moving at a constant angular rate with respect to every pixel in the image. Then as the raw images are co-added together the non-uniform motion of the observed scene is accounted for and will not geographically distort the final images, or any features seen within them. Through simulation using output from the SAMI3 model during plasma depletion formation it was determined that the structuring and gradients of plasma depletions can be recovered using this technique. Additionally, the effects of depletion width, solar activity level, and misalignment of the field-of-view with the local magnetic field were investigated. The variable-range TDI technique is able to recover the overall shape and depth of depletion of the depletions in all cases, however the determination of gradients observed at depletion walls is significantly degraded for very narrow plasma depletions and during periods of low solar activity. All simulated model conditions were shown to be representative of current ionospheric conditions.

Spatial Resolution of Equatorial Plasma Depletions Using Variable-Range Time-Delay Integration

Andrew Webster Napiecek

GENERAL AUDIENCE ABSTRACT

Equatorial spread-F, also termed plasma bubbles, is a phenomenon that occurs in the equatorial region of Earth's ionosphere, the charged region of Earth's atmosphere. Plumes of less dense plasma, the charged material of the Ionosphere, rise through regions of higher density plasma. This causes disturbances to radio signals that travel through this region, which can lead to GPS range errors or loss of signal. ICON is a NASA Explorer mission aimed at, in part, understanding the sources of variability in the ionosphere. One instrument onboard ICON to accomplish this goal is the Far-Ultraviolet Imager which images airglow in the far-ultraviolet range. During nighttime, the FUV imager can observe plasma bubbles to study the instability and the mechanisms that produce it. This thesis looks at the ability of the variable-range time-delay integration (TDI) algorithm, used to produce images from ICON's Far-ultraviolet imager, to spatially resolve the structure and gradients of observed plasma bubbles. However, due to the viewing geometry of ICON's FUV imager, each pixel across the observed scene experiences a different angular rate of motion blur. The variable-range TDI algorithm removes this non-uniform motion blur by transforming each raw image onto a surface where the spacecraft moves at a constant angular rate with respect to every pixel in the image. Then raw images are integrated together such that the observed scene is not geographically distorted. It was concluded that the TDI process is able to spatially resolve a wide variety of plasma bubbles under various ionospheric conditions and imager configurations.

Acknowledgements

I would like to thank Dr. Scott England for his support and guidance throughout this entire process. I would also like to thank Dr. Jonathan Black and Dr. Bhuvana Srinivasan for serving on my Advisory Committee. Additionally, I would like to thank Dr. Joseph Huba for providing the SAMI3 model data. The ICON Ancillary and Level 1 FUV data files used in this study were generated for testing purposes and made available by the ICON FUV team. These files do not come from actual flight data. The ICON mission is supported by NASA's Explorer's office through contract NNG12FA45C. The GOLD Level 1C data used in this study are publicly available from the GOLD website at gold.cs.ucf.edu. GOLD is supported by NASA's Explorer's office.

Table of Contents

List of Figures

List of Tables

1 Introduction

The ionosphere is a highly dynamic environment that couples Earth's atmosphere to space. Conditions in the ionosphere are extremely variable, so much so that conditions in the ionosphere are different from day to day with seemingly identical external conditions and inputs. The increasingly technological world we live in is becoming more and more reliant on the ionosphere. Signals we use to communicate and navigate are constantly passing through or reflecting off the ionosphere. Therefore, understanding the variability of the ionosphere and the forces and processes that shape it are a science objective of NASA (Immel et al., 2017). One unpredictable phenomenon in the ionosphere that causes disruption of these signals our society relies on is equatorial spread-F. It is important to understand more about this phenomenon to better characterize when are where scintillation of radio signals can occur.

This chapter will serve as an introduction to Earth's atmosphere and the phenomenon of equatorial spread-F. It will also formulate the structure and objectives of this thesis. Section 1.1 gives an overview of Earth's atmosphere and the regions within it, section 1.2 introduces the part of Earth's atmosphere that is ionized, the ionosphere. Section 1.3 summarizes the known characteristics of equatorial spread-F and processes that drive it, while section 1.4 presents previous research and discoveries on equatorial spread-F through the use of airglow emissions. Finally, section 1.5 reviews the pertinent science goals and design of the ICON mission.

1.1 Earth's Atmosphere

The Earth's atmosphere is a complex and dynamic region surrounding the planet that plays many vital roles. At low altitudes it contains the oxygen most organisms need to survive and at higher altitudes it absorbs harmful radiation from the Sun. Density and pressure decrease exponentially from the surface of the Earth to a near vacuum at the edge of space. The temperature, however, undergoes a more complex transition from surface temperatures to in excess of 1000K in the exosphere. Based on regions of heating and cooling the atmosphere is divided into four primary layers. The troposphere is the lowest region that extends from the surface to an altitude of roughly 12 km, and is where most of human activities take place including commercial air travel. This region is characterized by decreasing temperature with altitude. The stratosphere is the next highest in altitude at roughly 12-50 km and this is where temperature in the atmosphere starts to increase again due to absorption of mid-UV in the ozone layer. The mesosphere is next at an altitude of roughly 50-80 km and is the coldest region of Earth's atmosphere. Finally, there is the thermosphere, which ranges in altitude from roughly 80km to the exobase, which can vary in altitude from 350-800 km depending on the solar conditions. This region is characterized by a rapid increase in temperature until the temperature reaches that in the exosphere. The exosphere is the region of atmosphere beyond these four layers where the density is so low the particles can no longer be treated as a gas.

The atmosphere near the surface is comprised of mostly molecular nitrogen and oxygen, with a small fraction of Argon and other gases. As altitude increases, atomic oxygen becomes the dominant species in the thermosphere, which gives way to hydrogen and helium in the exosphere. A vertical profile of how temperature and composition of Earth's atmosphere change with altitude can be seen in Figure 1.

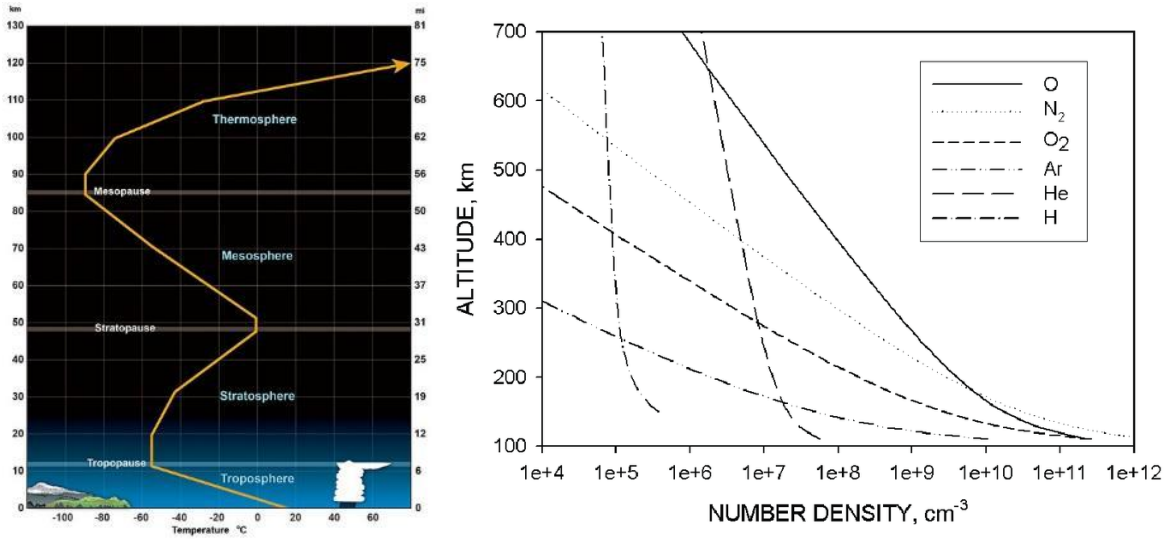

Figure 1: Vertical profile of the a) temperature and b) neutral composition of Earth's atmosphere. Figure a) from https://www.weather.gov/jetstream/layers and figure b) from U.S. Standard Atmosphere (1976).

1.1.1 Earth's Upper Atmosphere

The upper atmosphere is characterized by low mass density, high temperature, and large scale molecular diffusion. The majority of spacecraft reside here in Low Earth Orbit. This region is highly variable and heated and cooled by many sources and mechanisms. The primary source of heating is short wavelength radiation from the Sun, but there are also contributions from atmospheric waves propagating up from the lower atmosphere and Joule heating from currents flowing to the polar regions. Cooling mechanisms include conduction of heat to lower parts of the atmosphere and radiation in the form of infrared emissions.

The solar radiation that heats the upper atmosphere can also break apart some atoms and molecules, ionizing them. The atmosphere above 90 kilometers has a consistent fraction of its components in a state of ionization, this is called the ionosphere. A profile of the electron density in this region during the day and night, as well as during solar minimum and maximum can be seen in Figure 2 and will be discussed further in the next section.

1.2 Earth's Ionosphere

The Earth's ionosphere consists of three regions characterized by different compositions and densities. Increasing in altitude there is the D-region, E-region, and F-region. The D-region consists of primarily molecular ions and some heavy metal ions from meteors. This region is the

lowest in altitude of the ionosphere and has a density during the day on the order of 10^4 e^-/cm^3 and nearly vanishes during the night. The E-region also consists of primarily molecular ions and has an altitude range from about 90 kilometers to as high as 150 kilometers. The density in this region ranges from 10^5 e^-/cm^3 during the day to 10^3 e^-/cm^3 during the night. The F-region is highest region in terms of altitude and electron density and is comprised of predominantly atomic oxygen ions. Characteristics of each region of the Earth's ionosphere are shown in Table 1.

	Altitude Range (km)	Dominate Ions	Density Values (e^-/cm^3) Day (Night)	Ionization Source
D-region	70-90	O_2^+, NO^+, metal ions	10^4 (~0)	X-ray, Lyman-α
E-region	90-150	O_2^+, NO^+	10^5 (10^3)	X-ray, EUV
F-region	150-500	O^+	10^6 (10^5)	X-ray, EUV

Table 1: Altitude, dominate ion, electron density, and primary ionization source of ionospheric regions.

There are two main sources of ionization in the ionosphere, photo-ionization and ionization from high energy particles. Photo-ionization results primarily from Extreme Ultraviolet (EUV) emissions from the Sun, and high energy particles can include cosmic rays, solar energetic particles, radiation belt particles streaming in along field lines, meteors, and many more. Both of these processes require that the impacting medium have greater energy than the ionization potential of the atom or molecule it is ionizing. Incoming photons and particles lose energy when ionizing atoms or molecules, however, some high energy photons and particles have enough energy to keep penetrating the atmosphere to ionize atoms and molecules at a lower altitude. The density of neutrals available for ionization also increases exponentially with decreasing altitude. This creates the classic Chapman profiles due to an exponentially decreasing number of particles and photons with enough energy to ionize and an exponentially increasing density of neutrals with decreasing altitude (Chapman, 1931). The primary source of ionization on the dayside of the ionosphere, except in the polar regions is through photo-ionization. The higher energy X-ray emissions from the Sun ionize all layers of the ionosphere, including penetrating to the D-region. The D-region is also ionized by hydrogen's Lyman-α emission. The E-region is ionized by high enough energy EUV emissions from the Sun that make it through the F-region, as well as X-rays. Finally, the F-region is ionized by lower energy EUV emissions or higher energy EUV emissions that carry on to lower altitudes and X-rays. This creates a peak in ion and electron density in the F-region of the ionosphere, known as the F-peak, that can vary greatly from around 250-500 km depending on the solar activity and whether it is day or night (Adeniyi et al., 2003).

$$O^+ + e^- = O + hv \qquad \text{Radiative Recombination} \qquad (1)$$

$$O^+ + N_2 = NO^+ + N \qquad \text{Rearrangement} \qquad (2)$$

$$NO^+ + e^- = N^* + O^* \qquad \text{Molecular Dissociation} \qquad (3)$$

In the ionosphere there are two main loss mechanisms that dictate the distribution of electrons and vertical ion profile of the ionosphere. The first method is through radiative recombination in which an atomic ion combines with an electron to produce a neutral atom and photon. A sample reaction with atomic oxygen is shown in Equation 1. This process is slow compared to molecular dissociation where a molecular ion combines with an electron to produce two neutral atoms. This process is much more frequent in the atmosphere because momentum does not have to be converted to a photon to satisfy the laws of conservation. Atomic ions can become molecular ions through the process of rearrangement. A sample reaction is shown in Equation 2, where an atomic oxygen ion reacts with molecular nitrogen to form a molecular ion and an atomic neutral. This reaction is very fast because its rate is proportional to the density of atomic ions and neutrals in the atmosphere, which far outnumber ions at lower altitudes. Loss through rearrangement and molecular dissociation occurs at a faster rate than radiative recombination for most of the ionosphere, until the density of neutrals in the upper parts of the ionosphere starts to limit this process. In the lower regions of the ionosphere where the density of neutrals is higher and molecular ions dominate, the loss of ionized particles is more pronounced. However, above the F-peak there are less molecules for the dominant atomic oxygen ion to rearrange with and as a result the loss in this region is slower. This causes the density of electrons in the ionosphere to decrease dramatically below the F-peak and subside less intensely above the F-peak. The shape of the vertical profile of the ionosphere can be seen in Figure 2.

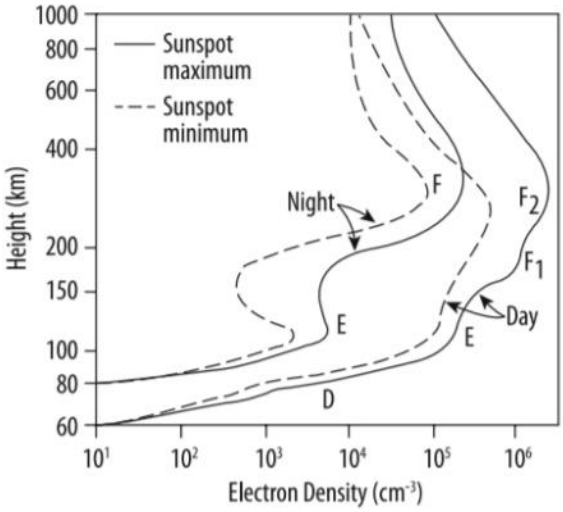

Figure 2: Figure from (Hargreaves, 1992) showing plasma density profiles for the day and night at solar minimum and maximum conditions at a mid-latitude location.

1.2.1 Equatorial Region of Earth's Ionosphere

Photoionization is the most intense during the daytime at the equatorial region. Therefore, the density of plasma in this region is the greatest, although it does not occur directly at the magnetic equator. The perpendicular forces exerted on the charged particles in the plasma at the magnetic equator from Earth's magnetic field and wind driven electric fields create an upward drift in the ions and electrons. This is referred to as the E x B drift in plasma physics. These ions produced at

the magnetic equator get forced upward and then due to gravity and pressure forces fall off to either side of the magnetic equator. This effect, similar to a fountain, creates two bands of enhanced plasma at about ±15° magnetic latitude on either side of the magnetic equator, known as the Equatorial Ionization anomaly. Figure 3 shows the resulting bright bands of high density plasma seen from the GUVI instrument in the 135.6nm wavelength, which is produced by radiative recombination of atomic oxygen ions.

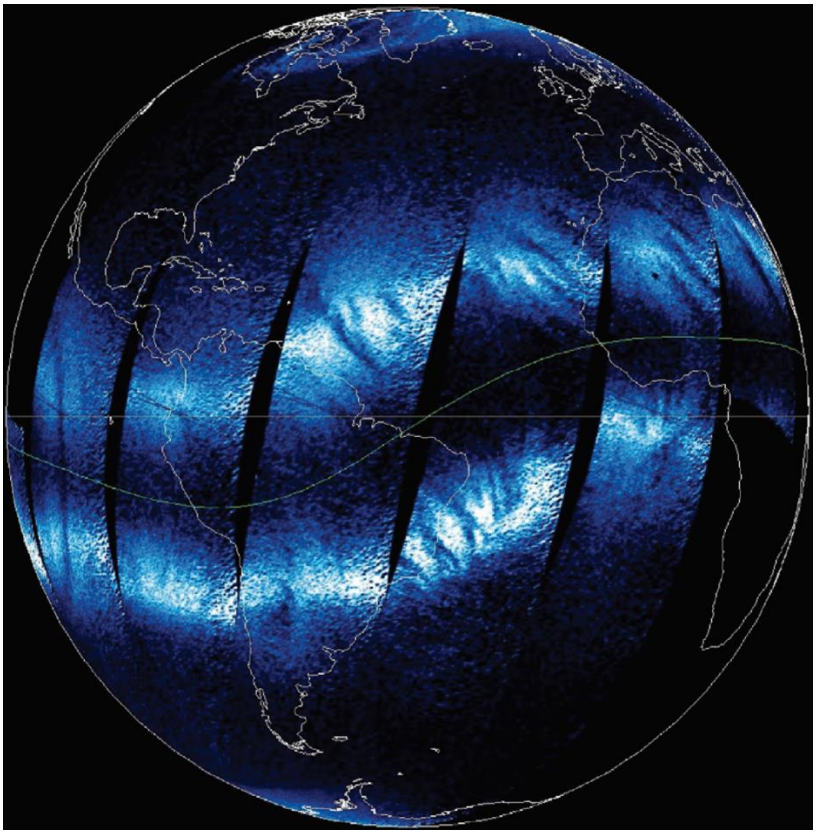

Figure 3: Figure after Comberiate et al. (2007) that shows the Equatorial Ionization Anomaly seen in the 135.6nm wavelength range from the GUVI instrument onboard TIMED. The curved line at the center is the magnetic equator and the bright bands on either side are EIA.

Many different forms of plasma drifts occur during day and night in the equatorial F-region of the ionosphere, and are also the result of E x B drifts. The electric fields that cause these drifts are set up by a process known as the F-region and E-region dynamos, where winds and tides in the neutral atmosphere drive the divergence of current and polarization electric fields are created (Kelley, 2009). Vertical plasma drifts are the result of zonal electric fields and zonal plasma drifts are the result of vertical electric fields. These drifts can have a high degree of variability from day to day. The average variation in vertical and zonal plasma drifts over Jicamarca Radio Observatory with respect to season, solar activity and magnetic activity were examined by (Fejer et al., 1991). The daytime westward zonal plasma drifts are independent of season, solar activity, and magnetic activity, while the nighttime eastward zonal plasma drifts are typically stronger and were shown to increase with solar activity and decrease with magnetic activity (Fejer et al., 1991). The vertical

plasma drifts during the day are upward and vary with season, being strongest near the equinoxes and weakest near the summer solstice. The daytime vertical plasma drifts do not vary much with solar activity but tend to decrease with an increase in magnetic activity (Fejer et al., 1991). Nighttime vertical plasma drifts are downward and strongly increase with solar activity. They also tend to have a dependence on magnetic activity during solar minimum, but not as much during solar maximum (Fejer et al., 1991). There is also a phenomenon known as prereversal enhancement of the vertical plasma drift, where shortly after sunset the upward drift of the plasma is greatly enhanced just before it turns downward. In his paper, Fejer et al. (1991) also examined the occurrence and magnitude of prereversal enhancement with respect to season, solar activity and magnetic activity. The maximum average prereversal vertical drifts seen were highest during equinox and varied linearly with solar activity level, except in winter when drift speeds seem to saturate at a high solar activity (Fejer et al., 1991). During equinox, magnetic activity tends to decreases the maximum prereversal vertical drift speed, however, in the winter magnetic activity increases the maximum prereversal vertical drift speed observed (Fejer et al., 1991).

The main source of electric fields seen in the F-region away from the terminator are those produced by the E-region dynamo and then mapped to the F-region. This is because the magnetic field lines are essentially equipotentials and the high conductivity of the E-region during the day prevents any polarization electric fields from forming in the F-region (Kelley, 2009). Global tides and thermospheric winds are the main drivers of these electric fields developed in the E-region and are the result of pressure gradients in the atmosphere created by the temperature bulge on the sun-facing side of the earth (Kelley, 2009). This leads to a charge build-up at the dusk and dawn terminators, and subsequently a global zonal electric field that is present in the E and F regions of the ionosphere. This produces upward plasma drifts during the day and the downward plasma drifts seen at night. The winds in the E-region also produce small meridional polarization electric fields at latitudes not on the magnetic equator that are then mapped to the F-region of the ionosphere as vertical electric fields (Kelley, 2009). These vertical electric fields are responsible for the westward plasma drifts during the day and eastward plasma drifts the night.

At night there is an enhancement of the zonal plasma drift speeds, which corresponds to an enhancement in the vertical electric field in the F-region. This is again due to thermospheric winds. In the F-region the zonal winds predominately produce motion of the plasma along the field lines (King and Kohl, 1965), however, they also produce a small drift in the ions in a direction perpendicular to both the magnetic field and wind (Rishbeth, 1971 a,b). This is due to interactions between the neutral particles blown by the wind and ions gyrating around field lines. For electrons, collisions with neutrals happen much less frequently compared to their gyrofrequency, and therefore do not drift in this direction and an electric current is set up in the vertical direction by the neutral wind, known as the F-region dynamo (Rishbeth, 1971a). At night, the conductivity in the E-region is severely reduced and this current is no longer able to be dissipated along filed lines by the E-region and a polarization electric field is set up in the F-region (Risbeth, 1971b). This

additional vertical electric field produced in the F-region results in stronger eastern plasma drifts during the night than western plasma drifts during the day.

The prereversal enhancement of the vertical upward plasma drift shortly after sunset, and thus the zonal electric field, can also be attributed to the F-region dynamo. As the sunset terminator is approached, the conductivity in the E-region in at least one end of the magnetic field lines passing through the F-region starts to be reduced. This prevents the F-region dynamo talked about previously from being shorted-out and allows the vertical polarization electric field to start to develop (Farley et al., 1986). This electric field is mapped down to the E-region where is becomes a meridional electric field and since the Hall conductivity in the E-region is not negligible, drives a westward zonal current away from the terminator (Farley et al., 1986). The E-region on the night side of the terminator is not as conductive and therefore a negative charge is built up at the terminator and an eastward polarization electric field is developed on the day side and a westward electric field is developed on the night side (Farley et al., 1986). This leads to an enhancement in the upward plasma drift and then the reversal of the vertical plasma drift to downward at night (Farley et al., 1986). Prereversal enhancement of the vertical plasma drift is linked to the occurrence of equatorial spread-F (Fejer and Kelley, 1980), which will be discussed further in the next section.

1.3 Equatorial Spread-F

Equatorial spread-F (ESF) are irregularities in the F-region of the ionosphere that usually occur shortly after sunset and first got their name from ionograms that were "spread" in range or frequency (Berkner and Wells, 1934). This phenomenon is now known to be the result of plasma instabilities that lead to irregularities in the density of the plasma (Hysell, 2000). This is of particular interest to study and predict because these irregularities in plasma density can cause changes to the amplitude and phase of radio signals (Hey et al., 1946). These are known as scintillations and among other side effects, can lead to GPS range errors or loss of signal between satellites and the ground. Much of the early study of ESF was done at Jicamarca Radio Observatory using coherent scatter radar to produce range-time-intensity plots like the one shown in Figure 4 from (Hysell, 2000). Now techniques such as scanning Altair incoherent scatter radar, in-beam radar imaging techniques, sounding rocket in-situ data, and observations of airglow emissions from satellites which will be discussed in the next section, are used to study ESF.

There are three classifications of ESF; bottom-type, bottom-side, and top-side. Bottom-type equatorial spread-F is a relatively thin layer of instabilities in the plasma at low altitudes of the F-region of the ionosphere (Hysell, 2000). It is nearly ubiquitous in the nighttime ionosphere after sunset and is generally controlled by the E-region dynamo (Hysell, 2000). Some of the time this layer drifts downward with the ambient plasma and becomes damped out, however, it is also possible that the F-region dynamo takes control of this region and allows the instabilities to grow becoming bottom-side equatorial spread-F (Hysell, 2000). This leads to irregularities in the plasma density that can grow in amplitude and result in large plumes of depleted plasma, known as top-

side equatorial spread-F (Hysell, 2000). Regions of higher density plasma are also forced downward, but the less dense regions of plasma bubbling up to the top of the F-region ionosphere is why ESF is also referred to as plasma bubbles. The large scale depletions that result from plasma bubbles can be seen from spacecraft in the form of airglow emissions.

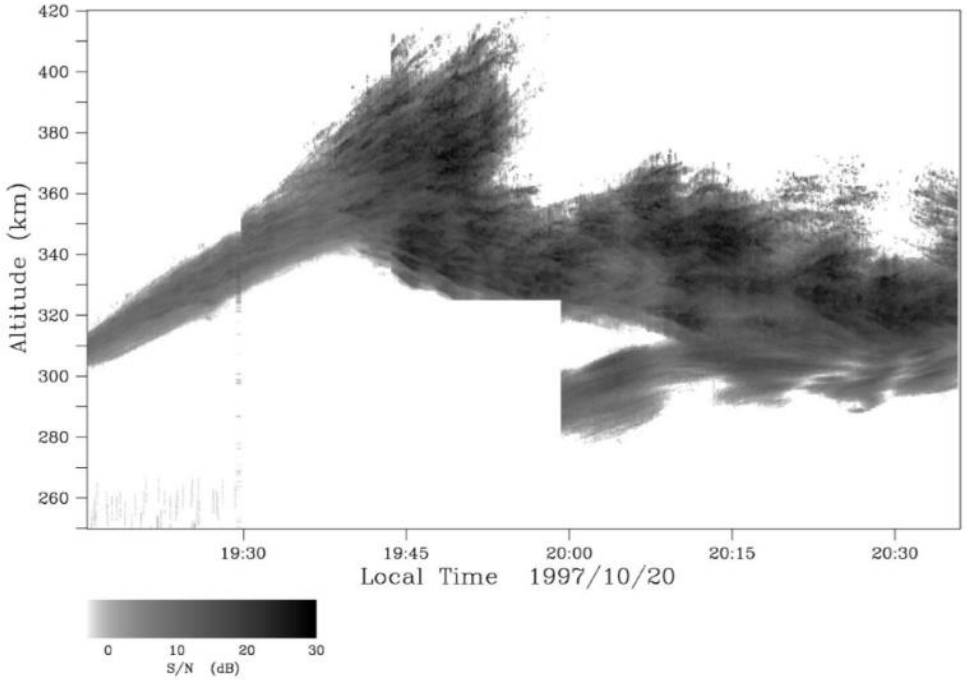

Figure 4: Figure from (Hysell, 2000) of a Jicamarca radar range-time-intensity plot depicting a bottom-type layer rising and abruptly transforming into a bottom-side layer.

Shortly after sunset, the D and E regions of the ionosphere start to disappear due to a lack of constant ionization from the Sun and a high density of neutral species to recombine with. The F-region also loses production via ionization from the Sun, however a much lower density of neutrals at high altitudes allows this region of the ionosphere to remain for much of the night. This leaves a dense region of plasma suspended over an increasingly less dense region of plasma. Small perturbations in this boundary can form as a result of the bottom-type equatorial spread-F or other seed mechanisms and grow into plasma bubbles via the magnetized Rayleigh-Taylor instability. A main mechanism thought to act as a seed in the formation of plasma bubbles is gravity waves (Kelley et al., 1981). If the phase velocity of the gravity wave is comparable to the drift speed of the plasma, then this modulation in plasma density acts on the same region of plasma and can generate the observed initial growth rates, not thought to be possible by the Rayleigh-Taylor instability alone (Kelley, 2009). Additional mechanisms such as, prereversal enhancement of the vertical plasma drift speed, turbulence in the mesosphere, and thermal fluctuations are also thought to contribute to the initiation of equatorial spread-F (Hysell, 2000).

The Rayleigh-Taylor instability was first proposed as the process producing equatorial spread-F by Dungey (1956). The Rayleigh-Taylor instability forms when the higher density plasma of the F-region is suspended over lower density plasma in the presence of gravity. A current is driven

throughout the plasma due to the perpendicular forces of gravity and the magnetic field. At the equator after sunset this current flows eastward along the boundary between high and low density plasma. The magnitude of this current is proportional to the density of the plasma it is flowing through. Thus, the small perturbations at the boundary of high and low density plasma will cause charge to build up at the edges of pockets of low and high density plasma. This will in turn create small electric fields at the boundary that cause the pockets of low density plasma to drift upward and the pockets of high density plasma to drift downward. This only makes the perturbations grow larger and the process is amplified forcing regions of low density plasma higher and higher. The current from gravitational forces is not the only one responsible for this instability. An eastward Pederson current resulting from the eastward zonal electric field shortly after sunset, currents from vertical neutral winds, and horizontal plasma density gradients can also lead to charge build-up in the perturbations of the boundary between high and low density plasma (Kelley, 2009). These all act as destabilizing sources of the magnetized Rayleigh-Taylor instability that leads to plasma bubbles. Plasma bubbles are particularly prone to happen in Equatorial Ionization Anomaly because the density of plasma in the F-region is higher in this region and allows for the magnetized Rayleigh-Taylor instability to form more prevalently.

$$\gamma = \frac{g}{n_0 \nu_{in}} \frac{\partial n_0}{\partial z} \tag{4}$$

The growth of the magnetized Rayleigh-Taylor instability is affected by many factors and a general equation for the growth rate that depends on gravity, the collision frequency between ions and neutrals, and the gradient scale length of the plasma is shown in Equation 4 (Kelley, 2009). This linear approximation does not take into account field-aligned integrated conductivities, that are required since the magnetic field lines are treated as equipotentials. At lower altitudes the collision-dominated regime is governing, however as the bubble grows and the altitude is increased the inertial regime starts to take over (Ott, 1978). The height this occurs at increases with bubbles size (Ott, 1978). Additional influences such as recombination rates, neutral winds, and ambient electric fields can all affect how plasma bubbles grow in the nighttime ionosphere (Sultan, 1996). Recombination rates can suppress the growth of equatorial spread-F if they are larger than the growth rate of the instability (Sultan, 1996). Vertical neutral winds can directly affect the grow rate, or meridional and transeuqatorial winds can work to redistribute plasma to areas of higher or lower conductivity in the ionosphere thus affecting the growth rate of the bubble (Sultan, 1996). The zonal ambient electric field drives plasma drifts in the vertical direction and can directly impact the growth rate of the magnetized Rayleigh-Taylor instability similarly to a vertical neutral wind (Sultan, 1996).

It is believed that plasma bubbles tend to occur at a higher rate during solar maximum conditions compared to solar minimum conditions and they also extend to higher altitudes and latitudes during periods of high solar activity (Sahia et al., 2000). Plasma bubble occurrence rates also have seasonal and longitudinal variations. Much of the plasma bubble activity seen occurs over the African and Western Pacific regions (Hei et al., 2005). While there are generally upticks in activity

during the equinoxes for most longitudes, the month of maximum occurrence depends on longitude (Su et al., 2008).

The irregularities in plasma density can have scale sizes of centimeters up to over 1000 kilometers seen in the large topside plasma bubbles. Topside plasma bubbles generally have zonal widths of 50 to a couple hundred kilometers and have a depletion of 30-50 percent compared to ambient plasma (Makela, 2006). Large topside plasma bubbles can also experience phenomena known as pinching and bifurcation. Pinching is the narrowing of the depleted plasma channel and bifurcation happens when an upwelling plasma depletion splits into two. Hysell (1999) concluded both are the result of secondary instabilities. Mendillo and Tyler (1983) suggested that bifurcation occurs at a mean altitude of 740 km at 2250 LT and decreases by roughly 10 km/h from 2100 to 2400 LT. Additionally, most plasma bubbles exhibit a westward tilt to them that is associated with a vertical shear in the zonal plasma drift speed due to differences in field line-integrated Pederson conductivities (Zalesak et al., 1982). Mendillo and Tyler (1983) found that plasma bubbles had an average tilt to the west of 0.6° longitude/100 km altitude and that tilt increased with local time presumably because the bubbles were older.

Weber et al. (1978) first pointed out that large scale plasma depletions are roughly aligned north-south with geomagnetic meridians. This was later refined to be a progressive west skewness to geomagnetic meridians that increased the farther away from the magnetic equator the depletions were (Mendillo and Baumgardner, 1982). The plasma bubbles also generally drift in the direction of the ambient plasma, both while they are forming and after they have formed. Typical drift speeds are around 100 to 200 m/s and tend to decrease as the evening progresses past local midnight (Makela, 2006). Plasma bubbles drift speeds have been shown to increase with solar activity and decrease with increasing magnetic activity (Immel et al., 2004). Plasma bubbles drift speeds also have some longitudinal dependence as pointed out by Immel et al. (2004).

1.4 Airglow Observations

A common approach to studying equatorial spread-F and what much of the data taken on a global scale and on the movement of plasma bubbles is taken through is airglow observations. This is possible because recombining ions in the ionosphere produce an optical signature that can be registered on the ground and from satellites. Observed airglow emissions are used as a proxy for the plasma density and can be useful in studying large portions of the ionosphere all at once. On the ground most airglow emission images are taken from all-sky imaging systems, while spacecraft can have a variety of imagers that are capable of viewing the entire disk of the Earth. Some typical observations of plasma bubbles using airglow emissions can be seen in Figure 3 and Figure 6. Figure 6 shows four images from ground-based cameras at the 630.0-nm emission wavelength and in Figure 3 you can see dark regions of depleted plasma in the bands of the Equatorial Ionization Anomaly that are plasma bubbles.

A variety of wavelengths resulting from an equally diverse set of chemical processes have been used to study the upper atmosphere and ionosphere. The complexity of the airglow emissions seen at Earth during the day and night in just the ultraviolet range can be seen in Figure 5 from Meier (1991). A few common examples used in the study of equatorial spread-F are OI 630.0-nm, 557.7-nm, OI 777.4-nm, 135.6-nm, and many more. OI 630.0-nm emissions known as the "red line" and 557.7-nm emissions are produced by dissociative recombination of O_2^+. OI 777.4-nm and 135.6-nm emissions are produced by radiative recombination of O^+.

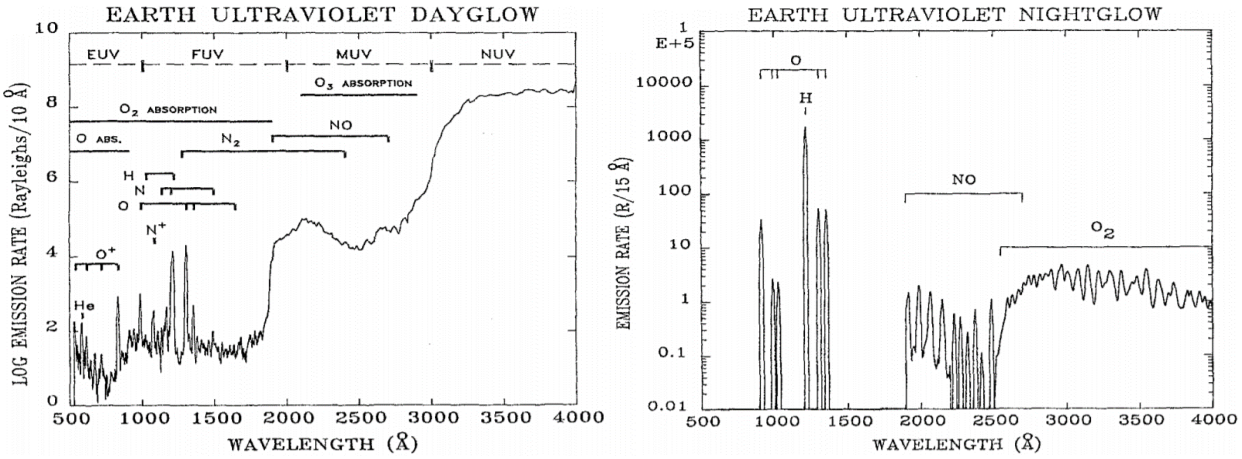

Figure 5: Figures from Meier (1991) of the UV dayglow and nightglow spectrums. All spectral features in the nightglow plot have been smoothed to 15 Å resolution.

OI 135.6-nm emissions will be the emission line of concern for this thesis and has several different atmospheric and ionospheric properties that can be inferred from it. During the day 135.6-nm emissions can be used to infer the atomic oxygen density in the neutral atmosphere. This along with additional emission information for N_2 can be used to determine the O/N_2 ratio, which is commonly used to investigate the neutral composition of the thermosphere. Notably, these observations were performed on the TIMED mission with the GUVI instrument, the GOLD mission, and will be employed on the ICON mission using the FUV instrument. Additionally, temperature of the upper atmosphere (Meier et al., 2015) and solar EUV irradiance (Strickland et al., 1995) can also be inferred from this information and through modeling. Both of these atmospheric properties were calculated from the TIMED/GUVI data. At night, since the O^+ dominated F-region is largely the only layer of the ionosphere left and radiative recombination is the primary loss mechanism due to the lack of neutrals and molecular ions at these altitudes, we can infer the plasma density profile of the ionosphere from the 135.6-nm emissions. This profile is useful in observing plasma depletions that result from equatorial spread-F and several other characteristics of the nighttime ionosphere. Through inversion techniques it is possible to infer the electron density profile of the ionosphere, as was performed by DeMajistre et al. (2004) on the TIMED mission. Important ionospheric properties such as F layer peak electron density (NmF2) and the altitude of this peak (hmF2) can also be extracted from 135.6-nm emissions. Observations of equatorial spread-F using 135.6-nm emission images were performed on the IMAGE and TIMED missions, which will be discussed further in the next chapter. Furthermore, plasma bubbles

have been seen in 135.6-nm emission images from GOLD data that will be presented in Chapter 4 and will be observed using this emission line on the ICON mission.

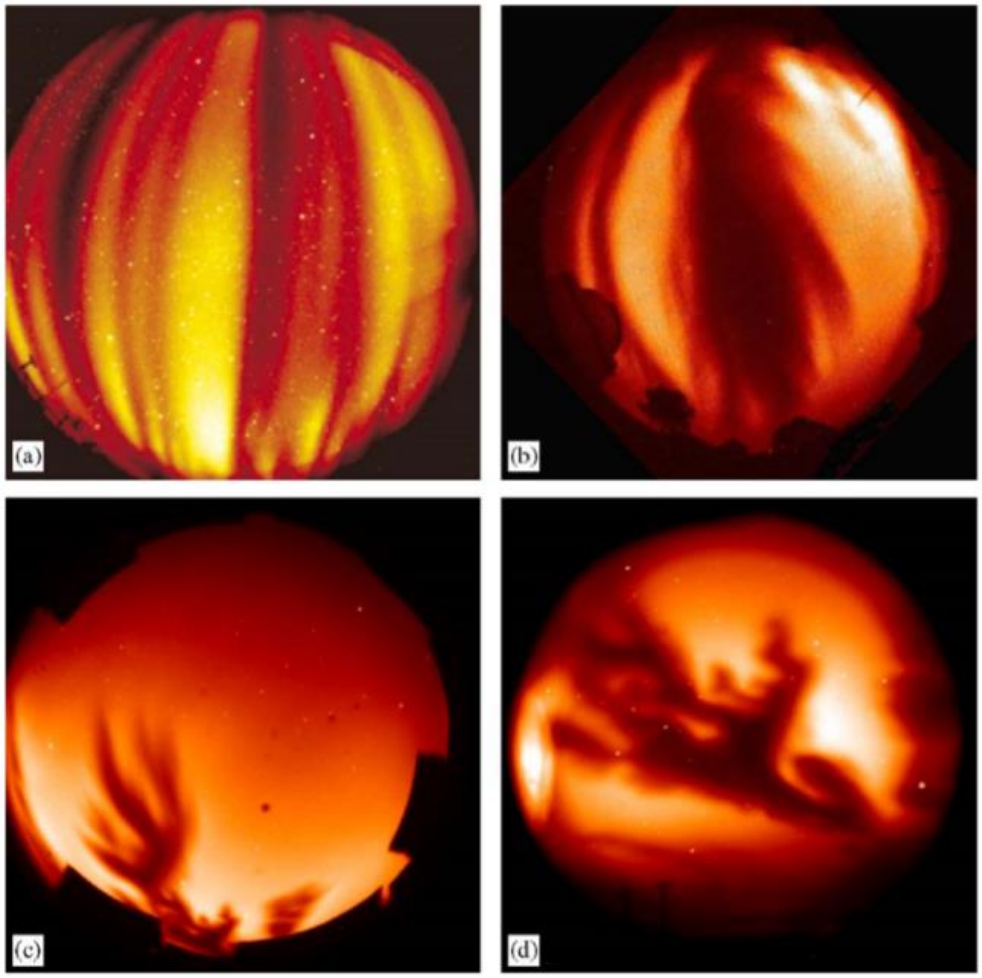

Figure 6: Figure from Makela (2006) shows typical images of equatorial spread-F seen on all-sky imagers, except for d) which is on a narrowfield camera, in the 630.0-nm emission wavelength. Image a) from M. J. Taylor, b) from Y. Sahai.

The use of airglow emissions to study equatorial spread-F has led to many advancements in the understanding of the phenomenon. Airglow observations allow us observe plasma bubbles in at least two dimensions to determine the overall structuring and shape of the depletion. They also give us the opportunity to study large-scale drifts of plasma bubbles for several hours after sunset. Observations from multiple sites and from space have confirmed the existence of geomagnetic conjugate plasma depletions on the opposite side of the magnetic equator.

Combing airglow emission images from multiple sources or with other forms of data has led to even more discoveries and analysis capabilities. Comberiate and Paxton (2010) combined GUVI images of plasma bubbles with SSUSI images to observe the evolution of a single depletion over a long period of time. Kelley et al., (2003) was able to combine observations of the same plasma bubble from the ground and from a satellite using data from GUVI and a Cornell Narrow Field

Imager on top of a volcano in Hawaii. This provides a new way to study equatorial spread-F and more insights can be gained by combining the two different perspectives, one looking from the top down and one looking along the magnetic field line from the ground. Kil et al. (2004) has similarly combined observations of plasma depletions from GUVI with in-situ measurements from ROCSAT-1. Measurements at offset latitudes allowed Kil et al. (2004) to confirm the depletion exists along the entire magnetic flux tube. The coverage provided by airglow emission images is beneficial in combining them with other in-situ measurements, such as shear in plasma drift speeds and composition, to further study plasma bubbles and some the of the still unanswered questions in the future.

1.5 Ionospheric Connection Explorer (ICON)

Ionospheric Connection Explorer (ICON) is a NASA Explorer mission aimed at learning more about how the ionosphere is coupled to the, neutral atmosphere below and deep space above, and the many dynamic processes that constitute this interaction. Summarizing the primary scientific objectives from Immel et al. (2017), ICON is focused on understanding sources of variability in the ionosphere, how energy and momentum is transferred from the Earth's atmosphere to space, and the effects of the solar wind and the magnetosphere on the atmosphere-space system. These objectives will shed light on the inputs that drive the extreme variability seen day-to-day in the ionosphere and how they are coupled together. Measurements to accomplish these goals include, altitude profiles of neutral winds and conductivity in the upper atmosphere, ion drift velocities, and upper atmosphere temperature and composition profiles.

Onboard ICON is a full suite of instruments that are capable of measuring the conditions in the lower thermosphere, as well as, observing the peak of the ionosphere (Immel et al., 2017). The Michelson Interferometer for Global High-Resolution Thermospheric Imaging (MIGHTI) onboard measures wind velocity by measuring the Doppler shift of the airglow emission red and green lines (Immel et al., 2017). MIGHTI can also measures the temperature of the upper atmosphere (Immel et al., 2017). Additionally, two Ion Velocity Meters (IVM), that consist of a Retarding Potential Analyzer and a Drift Meter, provide in-situ measurements of the electric field perpendicular to the magnetic field and the ion motion parallel to the magnetic field (Immel et al., 2017). Two more instruments onboard observe ultraviolet airglow emissions from the limb and disk. The Extreme-Ultraviolet Spectrometer (EUV) measures the altitude profile of ion density during the daytime using two emission profiles of O^+ (Immel et al., 2017). And finally, the Far-Ultraviolet Imager (FUV) measures the thermospheric density profiles of O and N_2 during the daytime and the O^+ density profile during the nighttime (Immel et al., 2017).

ICON's target orbit is a circular orbit with an inclination of 27°, and an altitude of 575 km. This was chosen because of the wide range of latitudes, longitudes, and local times that can be sampled, both in situ and remotely that are magnetically connected (Immel et al., 2017). This allows the instruments onboard to perform the work of what would normally involve observations from two satellites.

In the following chapters I will recreate the variable-range time-delay integration technique that is implemented onboard ICON and test the capabilities of it to spatially resolve plasma bubbles through a series of simulations. Chapter 2 focuses on the recreation of the TDI process and verification of the results with Wilkins et al. (2017). A simulation of observing a modeled plasma bubble using SAMI3 output from ICON's FUV imager geometry is also presented in Chapter 2. Finally, an outline of the code used to process images of observed plasma bubbles and determine their geographic location concludes Chapter 2. Chapter 3 expands this simulation to test three different scenarios that examine the capabilities and range of plasma bubbles that are detectable using this TDI process. Chapter 4 roots the parameters used in these test simulations in current ionospheric conditions using images from the GOLD mission, and Chapter 5 discusses the conclusions we can draw from these simulations.

2 Methods

This chapter details the special circumstances requiring a variable-range time-delay integration technique to be used to observe the nighttime ionosphere from ICON's FUV instrument, as well as the methodology behind the process used to meet ICON's image resolution requirements. The TDI process used onboard the spacecraft and the post-downlink data processing procedures to determine the geodetic coordinates of the observed scene are discussed and will be used on simulated data presented in Chapter 3. TDI images will be tested against the results of (Wilkins et al., 2017), in which the TDI process for ICON was originally described. To demonstrate the effects of the TDI process and the characteristic noise associated with image integration, a simulation of an observed plasma bubble from ICON's FUV spectrographic imager was run using output from the SAMI3 ionospheric model. Finally, metrics will be developed to quantitatively determine the ability of the TDI process to spatially resolve images of the nighttime ionosphere from ICON's FUV Spectrographic Imager.

2.1 FUV Observation Geometry

As detailed in (Mende et al., 2016), The Far-Ultraviolet (FUV) Spectrographic Imager onboard ICON has two wavelength channels, a shortwave channel optimized to observe 135.6 nm light and a longwave channel optimized to observe 157 nm light. The phenomena occurring in the nighttime equatorial ionosphere can be imaged using the shortwave channel of the FUV instrument due to radiative recombination of O^+ producing 135.6 nm wavelength light. The FUV instrument uses a Czerny-Turner spectrograph configuration to separate out the two target wavelengths inside the instrument (Mende et al., 2016). The far-ultraviolet light that passes through the Czerny-Turner spectrograph is converted to electrons through FUV photocathodes which are evaporated onto a stack of two microchannel plates (MCP) that multiply the electron count by a factor of one million (Mende et al., 2016). The microchannel plates are phosphor fiber-optically connected to a charge-coupled device (CCD) that reads out counts to be stored and co-added to form the images we receive on the ground (Mende et al., 2016). A diagram of how incoming light is processed is shown in Figure 7.

The FUV spectrographic imager onboard nominally points 90° from ram out the port side and 20° down from local horizontal to observe far-ultraviolet emissions between 100-450 km above the Earth (Immel et al., 2017). This orientation is used to produce the geometry necessary to sample magnetically connected *in situ*, as well as, remote observations to study the strong variability in the ionosphere. This geometry can be seen in Figure 8. The 135.6 nm airglow observed by the shortwave channel of ICON's FUV spectrographic imager is very dim. Due to these dim emissions from recombining oxygen and significant shot noise from the detector, the images need a twelve second integration time to keep the signal-to-noise ratio at acceptable levels (Mende et al., 2017). During this integration time, the spacecraft is moving horizontally with respect to the observed scene and moves roughly 96 km, which produces a non-negligible motion blur across the observed

scene. The FUV emission in this region is considered to be optically thin, which allows us to make the assumption that the source of the FUV emission comes from the tangent point of a line-of-sight. The tangent point is the location in space where the look vector is tangent to a surface with constant radius from the center of the Earth. Additionally, the emission of 135.6 nm light from recombining O^+ is also assumed to have a peak at 300 km shortly after sunset. Look vectors corresponding to a tangent height less than 300 km are referred to as "sub-limb" observations and the tangent point is considered to be where the look vector intersects a surface 300 km above the surface of the Earth. Pixels with look vectors corresponding to a tangent height greater than 300 km are referred to as the "limb" observations. Figure 9 shows the observational geometry for limb and sub-limb observations.

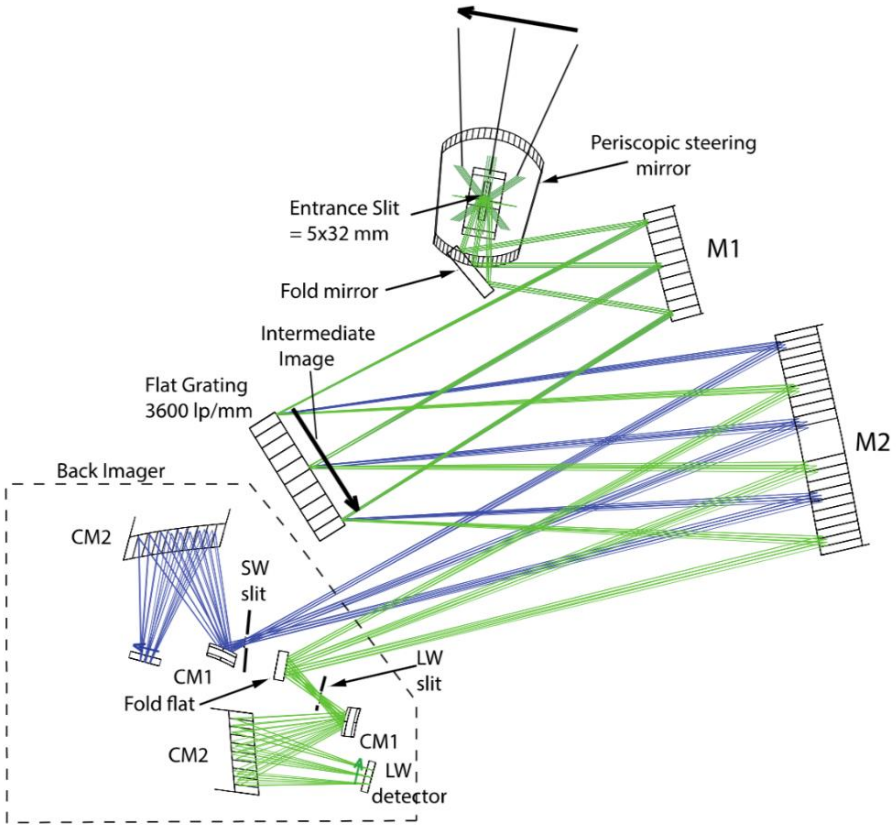

Figure 7: Geometry and configuration of ICON's Far-Ultraviolet Spectrographic Imager. ICON FUV is a Czerny-Turner spectrographic imager. Turret contains a movable steering mirror and a fixed entrance slit. Mirror 1 (M1) focuses the object viewed by the instrument on the grating. This intermediate image is then re-imaged on the detectors by M2 and the back-imager optics. The two wavelength channels are handled by separate exit slits, back imager optics and detectors. Figure from Mende et al. (2017).

The orbital altitude of ICON is unlike previous plasma imaging missions to utilize time-delay integration, at 575 km above the Earth. The low altitude of the spacecraft and long exposure time cause the motion blur to occur at different rates across the entire observed scene, based on the range-to-target for each pixel. Range-to-target is defined as the distance from the spacecraft to the

tangent point for the look vector of that particular pixel. Figure 10 shows the variable range-to-target distances for pixels in a typical observed scene, which is a recreation of Figure 1 in (Wilkins et al., 2017). From Figure 10, it is possible to see that emissions observed at the bottom of the image on the sub-limb are only about 600 km away from the spacecraft, however, emissions near the "horizon" at the intersection between the limb and sub-limb are over 1800 km away from the spacecraft. This wide range of range-to-target distances throughout the observed scene causes the spacecraft to move at a different angular rate with respect to each pixel in the image. This in turn, causes each pixel in the image to move a different amount throughout image integration. Thus, the motion blur across the observed scene will smear the image non-uniformly. For this reason, a novel Time-Delay Integration technique (TDI) with variable range-to-target motion-compensation was developed and is implemented onboard ICON in Field-Programmable Gate Arrays (FPGAs) (Wilkins et al., 2017). This variable-range time-delay integration transforms images onto a surface where the spacecraft is moving at a constant angular rate with respect to every pixel in the image. Then we can perform time-delay integration that will account for the non-uniform motion of the observed scene throughout integration and not distort the image.

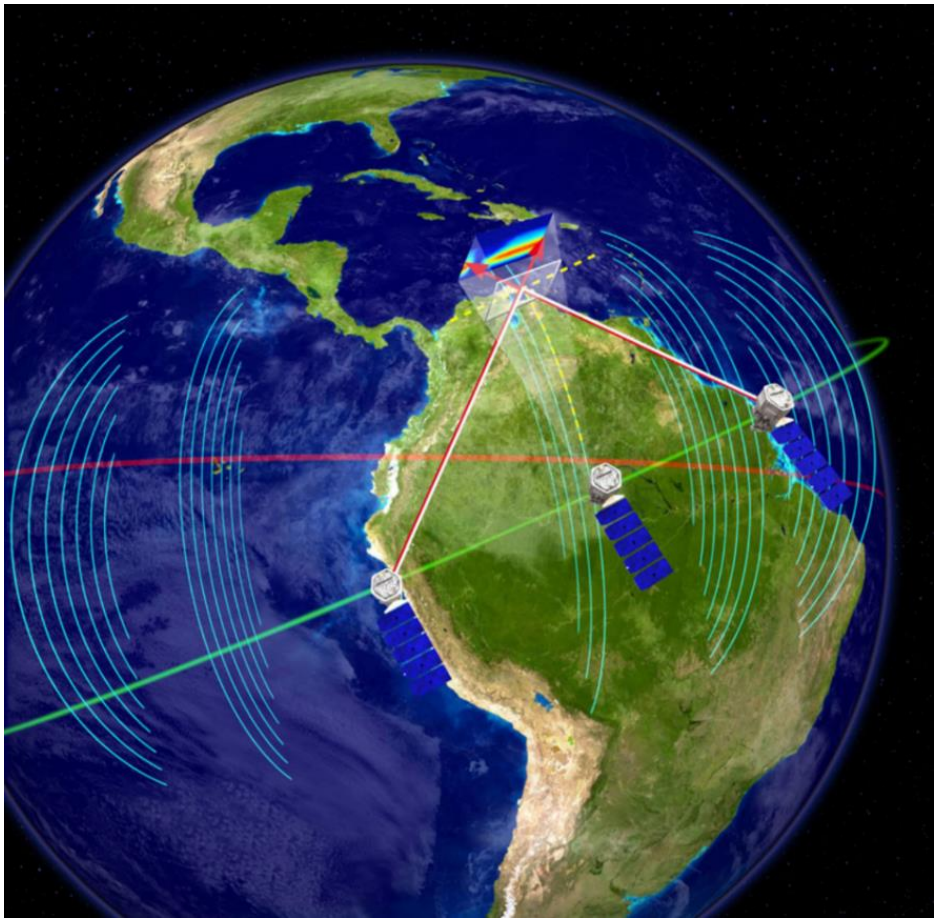

Figure 8: Figure from Immel et al. (2017) shows the observational geometry employed by ICON to observe magnetically-connected remote and *in situ* measurements, to fully characterize the coupling between the ionosphere and thermosphere.

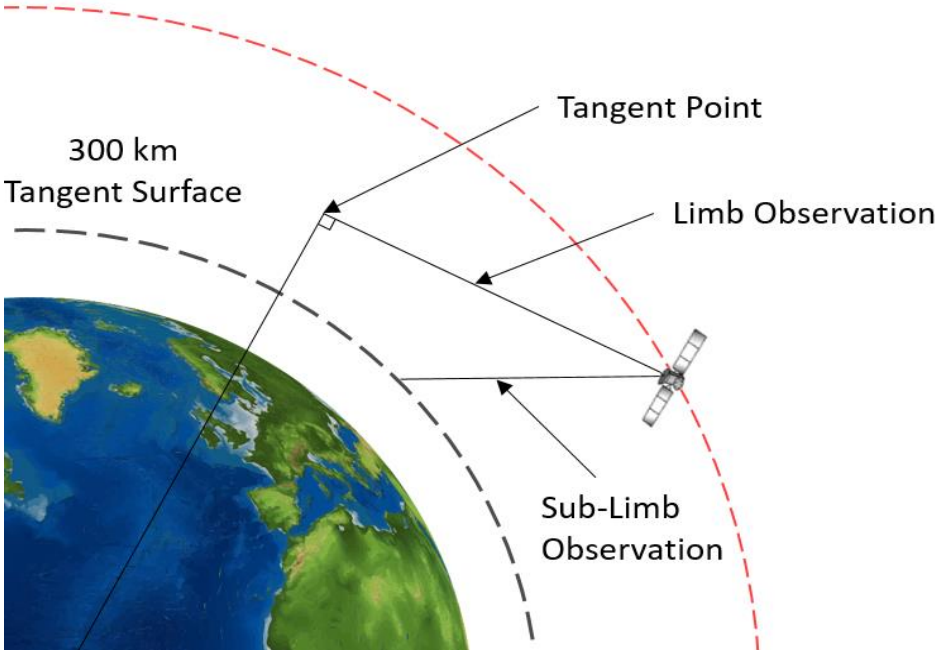

Figure 9: Tangent point geometry of limb and sub-limb pixels. The dashed red line represents the spacecraft's orbit and the black dashed line represents a surface at 300 km that distinguishes limb observations from sub-limb observations.

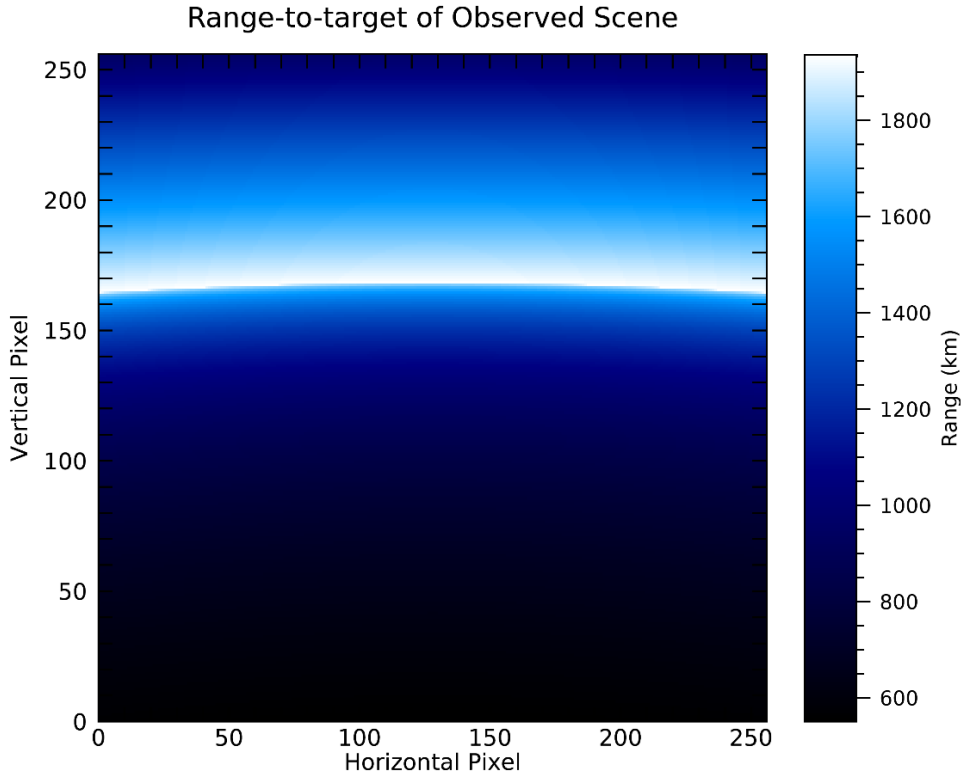

Figure 10: Range-to-target of FUV emissions in typical observed scene. The horizon is visible where the limb and sub-limb meet at an altitude of 300 km. Pixels in this region have a range-to-target three times greater than pixels elsewhere in the image.

2.1.1 Previous Plasma Imaging Missions

Previous missions have used ultraviolet imaging of airglow emissions to recover plasma density profiles of the ionosphere. The first to observe 135.6-nm FUV nightglow from a satellite was the OGO-4 (Barth and Schaffner, 1970). Subsequent missions have aimed at imaging plasma bubbles and other equatorial ionospheric phenomena using 135.6-nm FUV nightglow emissions, most notably on the IMAGE and TIMED missions. The IMAGE spacecraft was launched into a highly elliptical orbit with a period of roughly 14.2 hours and an apogee of 7.2 R_E, leading to consistent imaging of low latitude emission for 6-8 hours per orbit when the latitude of apogee was sufficiently low (Immel et al., 2004). Due to apsidal motion, the spacecraft's latitude at apogee processed from 40° N, through 90° N, and back down to 40° N over the first three years of the mission (Immel et al., 2004). Imaging using the SI-13 channel of the Spectrographic Image (SI) onboard, occurred at a cadence of every two minutes, matching the rotation rate of the spacecraft, and had an integration time of 5 seconds (Immel et al., 2003). Time-Delay Integration was used on the SI-13 channel to account for the rotation of the spacecraft during image integration, however it was just a simple offset in one direction because the entire scene was assumed to be at a fixed distance (Frey et al., 2003) and therefore the spacecraft was moving at a constant angular rate with respect to every pixel in the image. The SI captured images on a 128 x 128 pixel grid with a field of view of 16.3° x 16.3° (Frey et al., 2003). This configuration results in each pixel in the SI-13 channel representing a 100 x 100 km^2 foot print and having a sensitivity of 15.3 counts/kR when the spacecraft is at an altitude of 7 R_E (Frey et al., 2003). Images from the SI-13 channel of the FUV instrument on IMAGE were mapped onto a regular grid of magnetic local time and magnetic latitude and displayed using a keogram to track plasma bubbles as in Immel et al. (2003), or averaged together with less temporal resolution to study larger scale structures such as the Equatorial Anomaly, as in Sagawa et al. (2005). An example of the mapped FUV emissions and keogram used in Immel et al. (2003) can be seen in Figure 11.

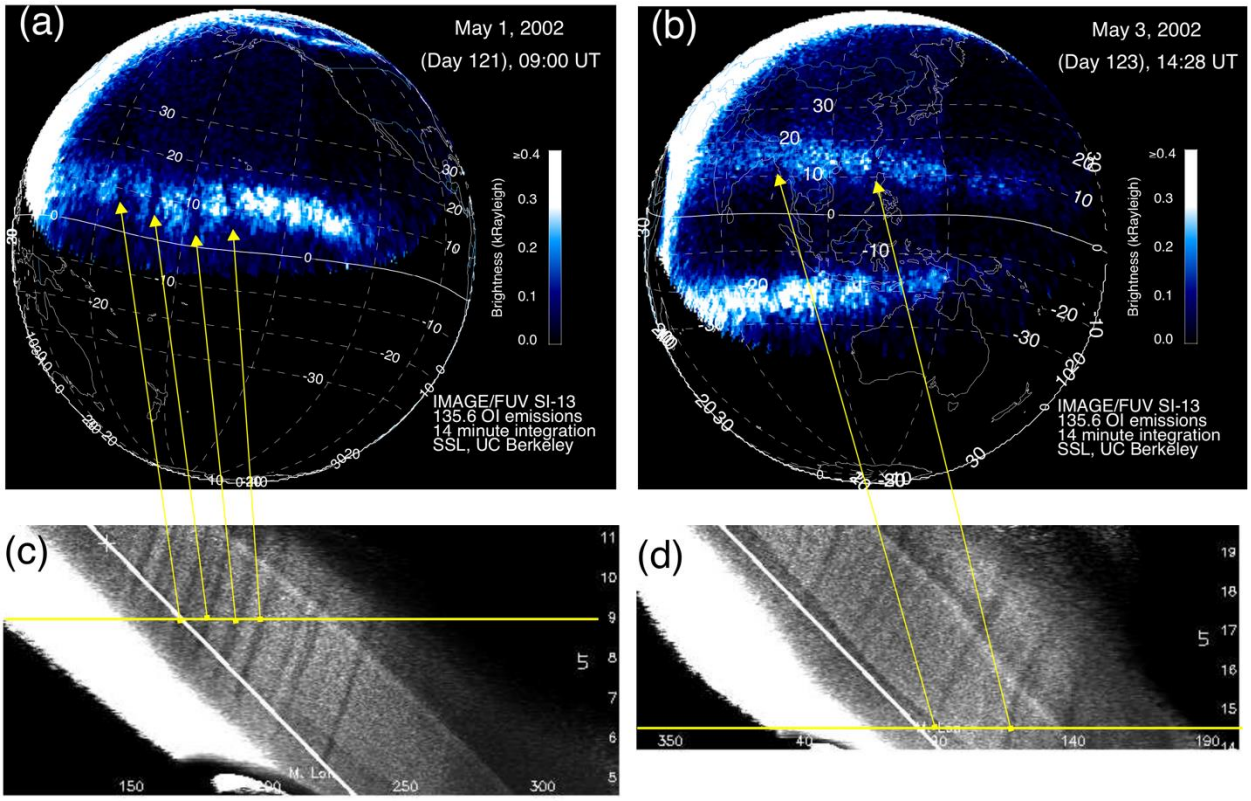

Figure 11: Figure from Immel et al. (2004) showing two integrated images of 5-second SI-13 exposures mapped onto a projection of geographic coordinates and two keograms used to track plasma bubbles.

The TIMED mission is another example of spacecraft-based imaging of the ionosphere using ultraviolet emissions. The Global Ultraviolet Imager (GUVI) instrument onboard uses a tomographic approach to retrieve information about nighttime ionospheric electron density profiles (Comberiate et al., 2007). The nadir pointing GUVI instrument scans 127.2° cross-track for disk images and has an in-track field of view of 11.8° (Comberiate et al., 2007). Images are captured on a 14 x 160 pixel array, with each scan having an integration time of 15 seconds or each pixel having an integration time of 0.064 seconds with a sensitivity of roughly 0.5 counts/second/Rayleigh/pixel (Comberiate et al., 2007). One drawback to the technique used for the TIMED mission is that it only produces a longitudinal resolution of 33 km (Comberiate et al., 2007). A tomographic model of 135.6-nm emissions is needed to reconstruct three dimensional ionospheric structures. Many assumptions and approximations go into this model, such as electron density will be constant over a 10° slice of latitude and only vary with altitude and longitude (Comberiate et al., 2007). As TIMED travels on its 79° inclined orbit over 10° of latitude, each scan adds information to this two dimensional model offset by 1° of latitude (Comberiate et al., 2007). The model consists of a vector of constant squared electron densities times a matrix proportional to the length of the line of sight for each constant electron density observation, plus an additive noise term all equal to a vector of the observations made by GUVI (Comberiate et al., 2007). The vector of constant electron densities is reconstructed by using the pseudoinverse of the

projection matrix and additional constraints on the solution based on prior knowledge to enforce realistic conditions (Comberiate et al., 2007). A final image of plasma density constructed using the observation model can be seen in Figure 12, along with an illustration of the imaging geometry used by GUVI.

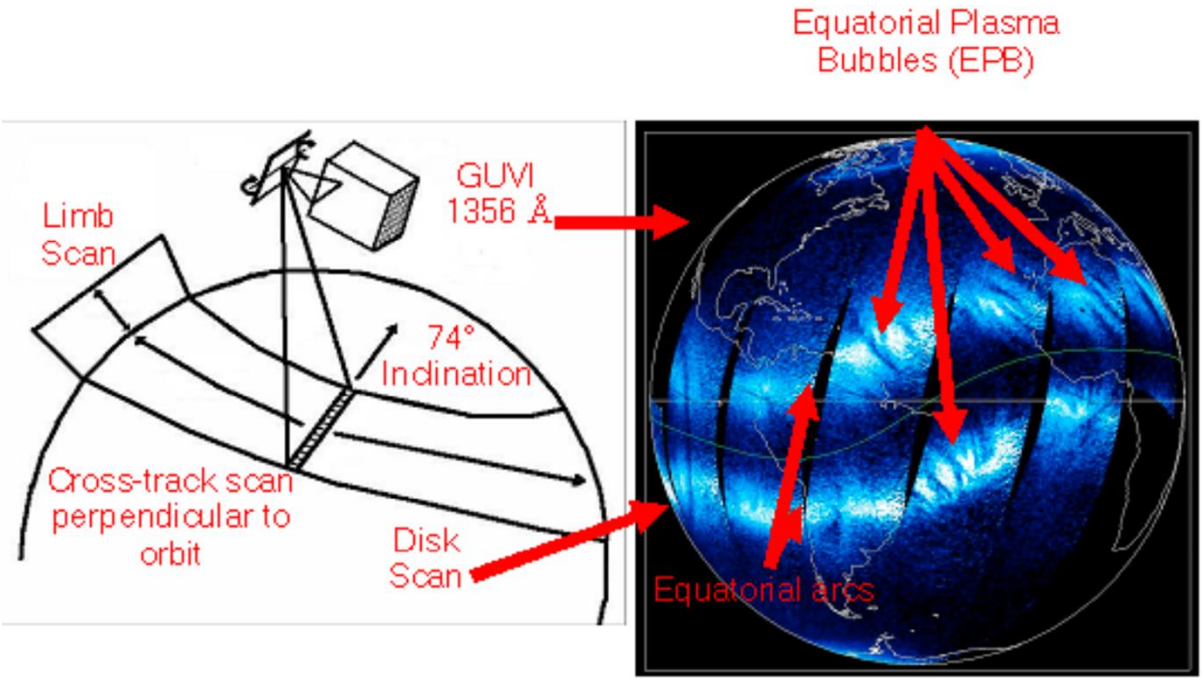

Figure 12: Figure from Comberiate and Paxton (2010) showing a final disk image produced by the GUVI instrument onboard TIMED and the imaging geometry used.

2.1.2 ICON FUV Mission Requirements

The FUV instrument observes both the day side and night side of the ionosphere and consequently, has a dynamic range of over 300 (Mende et al., 2017). To satisfy imaging requirements for both, 100 raw images are digitally co-added together, therefore only a dynamic range of 3 per image is needed. Throughout the 12 second integration time needed to image the nighttime equatorial ionospheric structures, an image is captured every 12 milliseconds. Due to bandwidth restrictions on ICON's downlink budget, each of the 100 raw images is not available for processing on the ground. Therefore, the TDI process must occur on the spacecraft and only a single integrated image is downlinked.

To resolve the structures of plasma bubbles a horizontal sampling resolution of 16 x 16 km was chosen (Mende et al., 2017). Unlike the two previous missions discussed above, ICON's FUV instruments looks out the port side of the spacecraft at only a 20° decline from local horizontal. Therefore, simple linear offset of the images to compensate for the spacecraft's motion, as used on the IMAGE and TIMED mission, will not suffice due to the Low Earth Orbit of ICON and non-nadir pointing orientation of the instrument. The TDI system makes an assumption about the altitude of the spacecraft and bins values onto an 8 x 8 km grid during image integration. To satisfy the 16 x 16 km resolution requirement, the true spacecraft altitude cannot deviate from the assumed

spacecraft altitude by more the ± 12.5 km (Wilkins et al., 2017). Both of these requirements necessitate a novel variable-range motion-compensation TDI process to be used to image spread-F in the nighttime ionosphere from ICON's FUV Spectrographic Imager.

2.2 Onboard Time-Delay Integration Process

The TDI process that happens onboard ICON uses a special coordinate system that is centered at the center of the Earth, called the Spacecraft Orbit-Aligned Position (SOAP) coordinate frame. The x-axis points from the center of the Earth through the position of the spacecraft, the positive y-axis points in the velocity direction, and the z-axis completes the right-handed system (Wilkins et al., 2017). In this coordinate system the TDI process assumes the spacecraft starts each image integration at 0° latitude and longitude and the spacecraft has a circular orbit directly over the equator. It also assumes that the spacecraft is at one of eight pre-determined altitudes spaced 25 kilometers apart and one of thirteen turret view-angles ranging from -30° to 30° in 5° increments. The altitude and turret view-angle of the instrument at the start of image integration dictate which pre-programmed look-up-tables (LUTs) are used for the TDI process. During the TDI process onboard the spacecraft there are also LUTs to correct for a permanent geometric optical distortion and thermal calibration, however these distortions will be assumed to perfectly corrected for in the downlinked images (Wilkins et al., 2017).

The variable-range time-delay integration process works to remove motion blur from images of the nighttime ionosphere by transforming each raw image onto a surface with constant linear motion and then co-adding the raw images together. The first aspect of the TDI process is to transform the raw images observed by the CCD onto a surface with constant linear motion. Due to the close proximity of the target and motion of the spacecraft, the motion of the observed scene varies across the image. To account for the non-uniform motion of the target, an algorithm that performs discrete image transformations on each image is implemented onboard using Look-Up Tables (LUTs) (Wilkins et al., 2017). This process is known as binning because the LUTs take values from the original image and bin them together based on the location of their tangent points to produce the limb and sub-limb images. This surface is considered to have constant linear motion because after the transformation the spacecraft moves with respect to each pixel in the image at a constant angular rate.

This can be more easily shown in Figure 13, in which a 1° latitude by 1° longitude checkerboard pattern was projected onto a surface corresponding to the anticipated region of maximum brightness along the line-of-sight for each pixel. These are the tangent points for the limb and sub-limb observations as described earlier. In the original observed scene detected on the CCD, the checkerboard pattern is distorted due to variable range-to-target across the scene and a turret view-angle of -10° causing the instrument to not look directly down a line of longitude in the SOAP coordinate frame. After the transformation the checkerboard pattern is square because the scene is projected onto a surface that has constant linear motion in latitude and longitude.

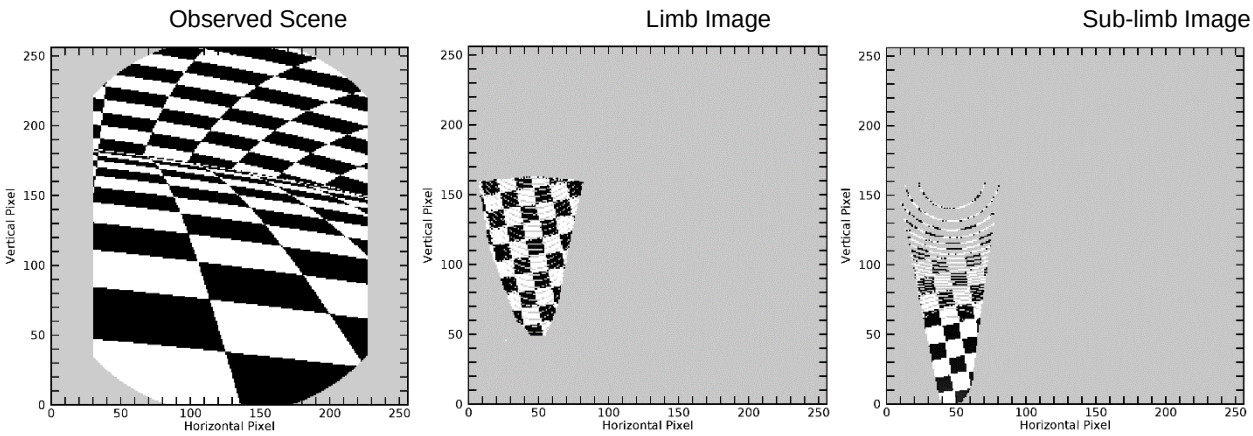

Figure 13: Discrete image transformation of 1° latitude x 1° longitude checkerboard scene to surface with constant linear motion. Turret view-angle of -10° used to demonstrate effects of non-zero turret view-angles. Grey on all three images represents no data.

Due to an odd number of mirrors in the rotating periscope used to capture the FUV photons, the turret view-angle introduces a rotation in the images detected on the CCD when the turret view-angle is not 0°. This rotation is corrected for using a LUT that rotates every pixel around the center of the image. During this transformation, some pixels are rotated to regions outside of the 256 pixel by 256 pixel image size, resulting in the short dash feature near the bottom left of the limb image, known as the dump pixel. This rotation of the image after detection also causes the limb and sub-limb image outlines to have a tilt to them, because the active pixels in the image that is binned are different than those detected on the CCD. The rotated image is then binned using a LUT that assumes the turret view-angle is always 0°. The LUTs do account for differences in turret view-angle when implementing the roll angle, but always assume the turret is at the 0° position. A turret view-angle of +/- 30° is used to implement the roll angle when the true turret view-angle magnitude is greater than 20° (Wilkins et al., 2017). The true bore sight of the observed scene is at an angle (the turret view-angle) relative to perpendicular to ram, and therefore will not look directly down a line of longitude in the SOAP coordinate frame. However, because the LUT assumes a 0° turret view-angle, the bore sight of the image is assumed to point perpendicular to ram and vertical in SOAP coordinate space. This causes the entire SOAP frame to be rotated when binned using a LUT by the value of the turret view-angle. Figure 14 shows the resulting rotation of the SOAP frame that is produced from a non-zero turret view-angle.

Once the incoming raw images have been transformed to a surface with constant linear motion, they can be simply offset and co-added together to form the final TDI image. Each successive raw image is assumed to occur 120 ms after the last; in this time the spacecraft is assumed to be stationary and no further action to account for the spacecraft's motion is taken. This is because each pixel roughly sees FUV photons from a 10 km by 10 km region of space, and the spacecraft would move less than 1 km in that time frame. The turret rotation also influences the co-adding process. In cases where the turret view-angle is non-zero, the image offset has a component in the Y direction in the SOAP coordinate space. This is due to the rotation of the SOAP coordinate

frame relative to the X and Y pixel directions of the image and the fact that the image offset must follow the path of the spacecraft.

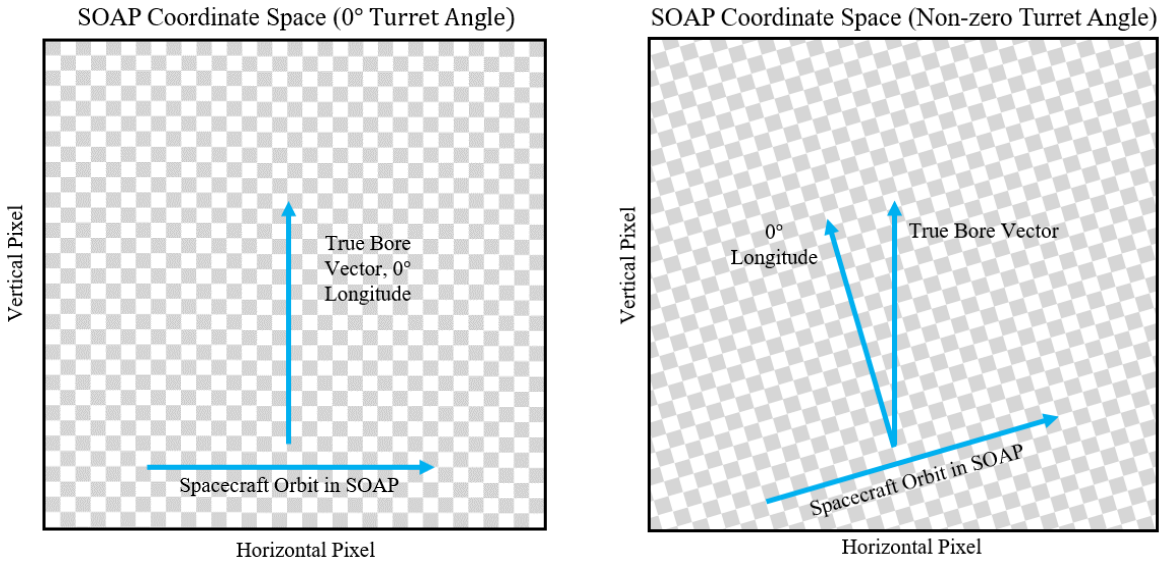

Figure 14: Illustration of the SOAP coordinate frame rotation resulting from a non-zero turret view-angle. Checkerboard represents 1° x 1° in latitude and longitude. The true bore vector of the image always points vertical in the SOAP coordinate space because the LUTs used in the transformation always assumes a turret view-angle of 0°.

During the binning and co-adding processes, some pixels experience artificial gain in brightness due to values from multiple other pixels being added into them (Wilkins et al., 2017). This gain is not experienced equally by every pixel in the image and must be removed via flat-fielding which determines the average brightness value that was added into that particular pixel. Additionally, during the co-adding process, raw image pixel values are binned based on the location of the tangent point of the center of that pixel. The entire raw brightness value is binned into a single pixel in the SOAP coordinate space. This makes the assumption that all the brightness registered at the detector for that pixel is coming from that point in space. However, due to the geometry of the observed scene, pixels, especially those near the horizon, represent a distorted shape in space. Brightness is also accumulated along the entire look vector for that pixel. This leads to some errors in the distribution of brightness in the final TDI images, as well as, areas of missing data in the images because the brightness values are binned instead of truly accounting for the distortion of each pixel. This can be most prominently seen in the sub-limb image in Figure 13, but is also present in the limb image. This pattern of missing data is similar to a Moiré pattern and is the result of adjacent pixels in the raw image having centers that are more than one pixel apart in the SOAP coordinate space. Some information about structure and size of the plasma bubble is lost as result.

2.2.1 Verification with Wilkins et al.

The TDI process discussed in the previous section was originally developed in (Wilkins et al., 2017). As verification that we have recreated the TDI process that is used onboard ICON correctly, we will compare our simulated TDI images to those in (Wilkins et al., 2017). Figure 10 shows the

range-to-target for FUV emissions of a typical observed scene during image integration. This figure matches identically to Figure 1 of (Wilkins et al., 2017) and serves to show that tangent point geometry of our TDI process is correct.

The main simulation used in (Wilkins et al., 2017) to demonstrate the TDI process is for a turret view-angle of -15° and makes use of the projected checkerboard pattern used in Figure 13. The final limb and sub-limb from this simulation can be seen in Figure 15 and will be compared to TDI images from our code. During image formation in (Wilkins et al., 2017) the observed scene for raw images was generated with a turret view-angle of positive 15°. This was discovered because the observed scene in Figure 6 of (Wilkins et al., 2017) is clearly looking behind the spacecraft and a negative turret view-angle corresponds to rotation of the turret toward ram. Additionally, sample TDI images using flight software show features consistent with limb and sub-limb images generated by our code. This will cause the checkboard pattern in the final images of (Wilkins et al., 2017) to have the opposite rotation as that produce by our code. The shape and position of the limb and sub-limb images will be unaffected in the SOAP coordinate space.

The overall shape of the sub-limb and limb images in Figure 16 match well with those in Figure 15. Grey represents areas with no data in Figure 16, similar to the white used in Figure 15. As mentioned earlier, the checkerboard pattern is rotated the opposite direction in Figure 16 and as a result, there is a more missing data on upper-right corner of the sub-limb image, as opposed to more missing data in the upper-left corner of the sub-limb image in Figure 15. This is because with a positive turret view-angle the left hand side of the observed scene will be farther from the spacecraft and will produce more missing data as more pixels are nearer the horizon. The opposite is true for a negative turret view-angle. The small dash feature that is used as a dump pixel during image rotation is slanted the opposite direction in Figure 15, this is also due to the opposite sign turret view-angle used for part of the scenario in (Wilkins et al., 2017).

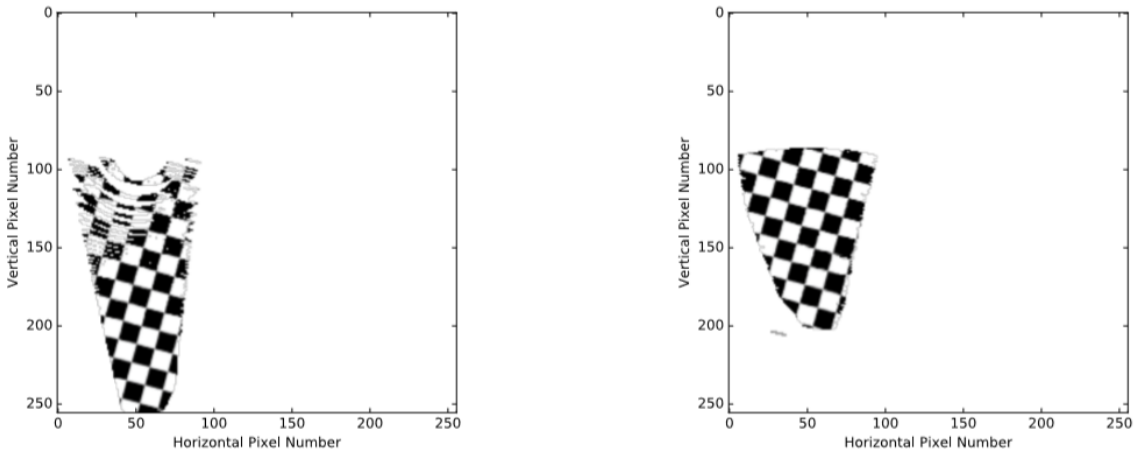

Figure 15: Sub-limb and limb TDI images from (Wilkins et al., 2017) using a -15° turret view-angle. 100 frames were co-added using motion compensation and distortion removal to produce these images. Note the checkerboard pattern is angled 15° clockwise from vertical instead of 15° counter-clockwise from vertical because the original observed scene was created using a turret view-angle of +15°.

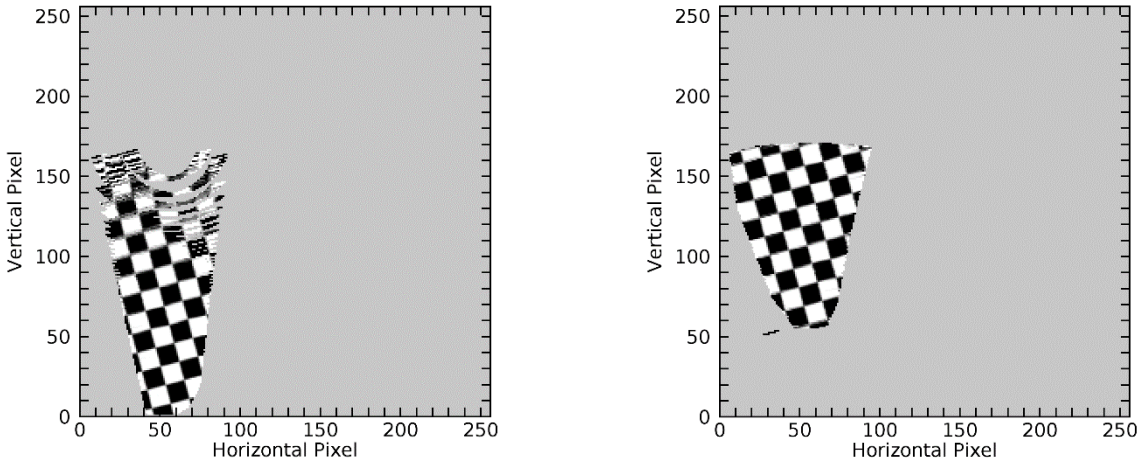

Figure 16: Sub-limb and limb TDI image produced by our code that recreates the TDI process used onboard ICON. The checkerboard pattern is rotated 15° counter-clockwise from vertical due to the -15° turret view-angle used for the simulation.

2.2.2 Geodetic Coordinates of Observed Scene

Once the images are on the ground, the true geodetic coordinates of the observed scene can be determined using information about the spacecraft's position, the instrument's attitude, and the WGS84 geodetic datum. The geodetic coordinates of equatorial spread-F captured by ICON's FUV spectrograph are necessary because they can be used to categorize the phenomena seen and facilitate comparison with additional data sets.

As part of verification of the TDI process and to ensure the correct assumptions for each image are captured, the TDI process using the SOAP coordinate frame was recreated for every combination of altitude and turret view-angle. The minimum latitude and longitude in the SOAP coordinate frame of each resulting co-added image was determined. This is the latitude and longitude of the bottom left corner of the image and is the base latitude and longitude the LUT onboard bins the entire image to. Therefore, the latitude and longitude of each pixel in the image can be extrapolated from this point because each pixel in the image represents an 8 km by 8 km region in the SOAP coordinate frame. Additionally, one of the assumptions made in the LUTs is that each degree of latitude and longitude represents 111 km in the SOAP coordinate frame. To save on computational time, during the recreation of the TDI process for all altitudes and turret view-angles, the pixels that have usable data in them are stored and only these pixels will be processed to find the geodetic coordinates.

Once the latitude and longitude of each 'active' pixel in the image are known, the ECEF coordinates of each pixel is needed to determine look vectors from the spacecraft's location in the SOAP coordinate frame to each of the active pixels in the image. For sub-limb observations the geographic coordinates are extrapolated to a height of 300 km above a spherical model of the Earth, and for limb observations the corresponding tangent height of the geographic coordinates is used to determine the ECEF coordinates. The position of the spacecraft during the middle of image

integration is used for the look vector calculations because as the spacecraft orbits the angle at which photons are observed from a theoretical bin in space that makes up a pixel changes, and the average of this angle occurs at the middle of image integration.

The look vectors for each active pixel in the image in the SOAP coordinate frame are then rotated and translated to the true position and pointing of the instrument. The true position of the spacecraft at the middle of image integration can be recovered from FUV Level 0 ancillary file. The look vectors for the four corners of the six-stripe altitude profile FUV data product can also be recovered from the FUV level 0 ancillary file. From the look vectors of the six-stripe altitude profile, the true bore sight vector and corresponding "up" and "right" unit vectors that make up a right-handed system that describes the attitude of the FUV instrument are determined. A similar coordinate frame can be developed for the SOAP frame using the knowledge that the instrument is half way through image integration that started at 0° latitude and longitude, the turret view-angle is assumed to be 0°, and other information about instrument pointing relative to the spacecraft's orbit. Both of these frames have their axes expressed in ECEF coordinates and therefore a rotation matrix can be determined from the SOAP frame to the ECEF frame, and similarly from the ECEF frame to the true instrument attitude frame. These rotation matrices are calculated through the corresponding dot products between respective axes of the two frames in the transformation. Using the rotation matrices, the look vectors are transformed from the SOAP frame to the ECEF frame and then to have the correct pointing of the FUV instrument during image integration. The base of the look vectors are also translated from the spacecraft position in the SOAP coordinate frame to the true spacecraft position.

The correct pointing vectors are then used to determine the geodetic coordinates of the observed scene using the WGS84 geodetic datum, an oblate spheroid model of the Earth. For the sub-limb observations, the method outlined in Section 2.2.2 of "SSUSI Data Products Algorithms" (2013) is used which employs a scaled z-axis to find the intersection between the look vector and a surface 300 km above the surface of the WGS84 datum. For limb observations a method similar to that described earlier using the tangent point of the look vector is used, however this time with the scaled z-axis as with the sub-limb observations. The geodetic coordinates of each pixel's observation are then calculated using Bowring's iterative method for the latitude and altitude. A comparison between the latitude and longitude profiles of the observed scene and the limb and sub-limb images is shown in Figure 17. Along with the geodetic coordinates of each pixel in the images, the altitude, range from spacecraft, ECEF coordinates of pixel location, and the look unit vector from the spacecraft is stored in a level 2 output file.

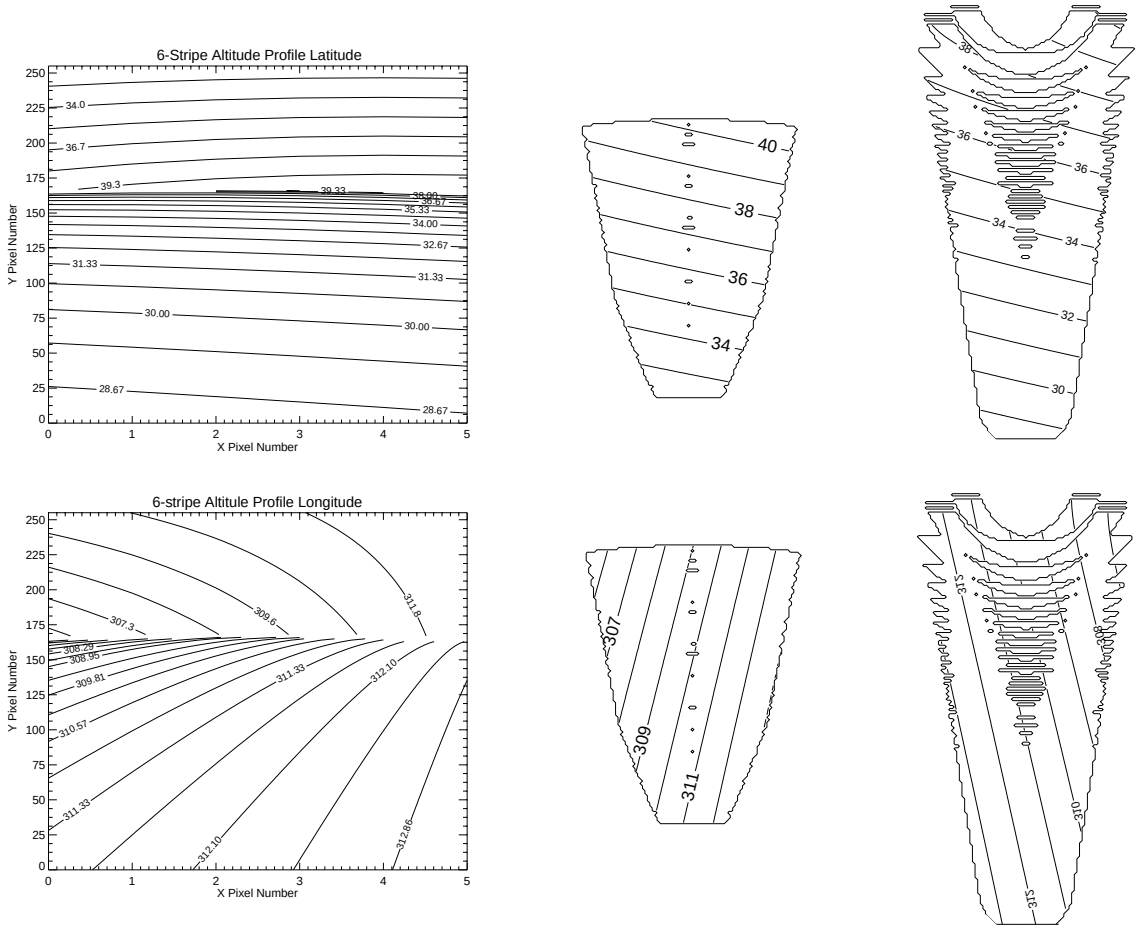

Figure 17: Contour plots of latitude and longitude of a) the observed scene and b) the limb and sub-limb images produced by the TDI process. The latitude and longitude profiles of the observed scene were taken from a previously produced data product. For this simulation the spacecraft is at 24.603° latitude, -46.769° longitude, a turret view-angle of 0°, and an altitude of 570.2 km at the mid-point of image integration.

2.3 Simulation Using SAMI3 Model Output

To verify the intricate structuring and plasma gradients developed in spread-F phenomena can be imaged, a simulation of viewing a plasma bubble from ICON's FUV spectrograph using the TDI process was performed. To accomplish this, the output from the SAMI3 model, provided by Dr. Joe Huba, was used to simulate the electron density in the ionosphere during a spread-F event. An advantage of the using the SAMI3 model output is that it can be easily configured to adjust the parameters of the bubble to test the capabilities of the TDI process. A sensitivity analysis varying the width of the plasma bubble, turret view-angle of the FUV instrument, and solar magnetic activity level will be performed in Chapter 3.

The SAMI3 model is a 3D first-principles physics model of the ionosphere developed by The National Research Laboratory based on the 2D ionosphere model, SAMI2 (Huba et al., 2008). It models the full transport of H^+, He^+, O^+, N^+, N_2^+, NO^+, and O_2^+ and solves the complete ion temperature equations for H^+, He^+, and O^+, along with the electron temperature equation (Huba et

al., 2008). The SAMI3 model has a low resolution global grid, and a high resolution wedge, that covers ~2° in longitude and covers ± 30° in latitude, as well as extending from 85 km up to 2400 km in altitude. The grid of the high resolution wedge has 201 grid points along magnetic field lines, 200 magnetic field lines with different foot points at a particular longitude, and 193 longitude locations across the span.

The SAMI3 model was run with the conditions necessary to produce a plasma bubble centered on the grid of the wedge. A snapshot of the electron density profile during bubble formation was used as the basis for the simulation. The field of view of ICON's FUV spectrographic imager is 24° in the vertical direction and 18° in the horizontal direction. This corresponds to ~6° of longitude and ~12° of latitude coverage when the turret view-angle is 0°. Therefore, the wedge of SAMI3 model output was extended on either side by continuing the ambient electron density values seen on the edges of the wedge.

Figure 19 shows a cross section of electron density from the SAMI3 model output at 0° latitude. The simulation was run assuming the plasma bubble is stationary throughout the image integration and the spacecraft starts at 0° latitude and longitude, in a circular orbit above the equator with an altitude of 575 km, and a turret view-angle of 0°. The bubble was also centered at 0° latitude and longitude and extends along the field lines perpendicular to the spacecraft's orbit. Figure 18 shows the geometry of the grid lines of the SAMI3 model, shown in grey, and the look vectors from ICON's FUV instrument, shown in blue.

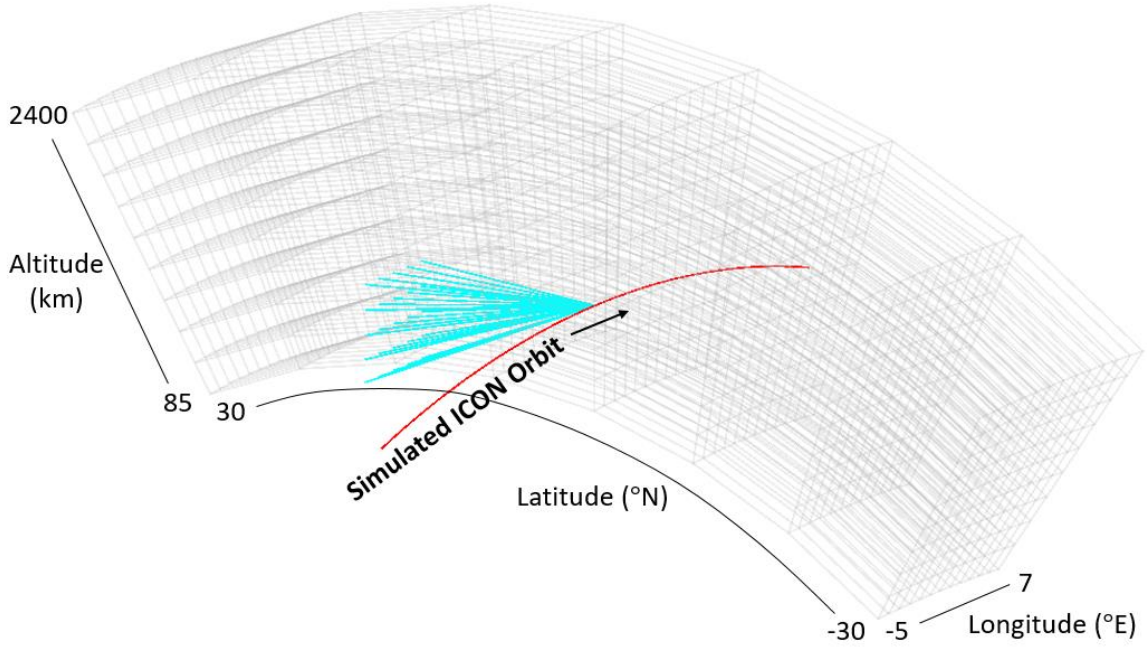

Figure 18: Visualization of SAMI3 sampling geometry from ICON's FUV imager in simulated orbit around the equator. ICON's orbit is in red, the SAMI3 grid is in grey, and the look vectors from ICON's FUV instrument are in blue.

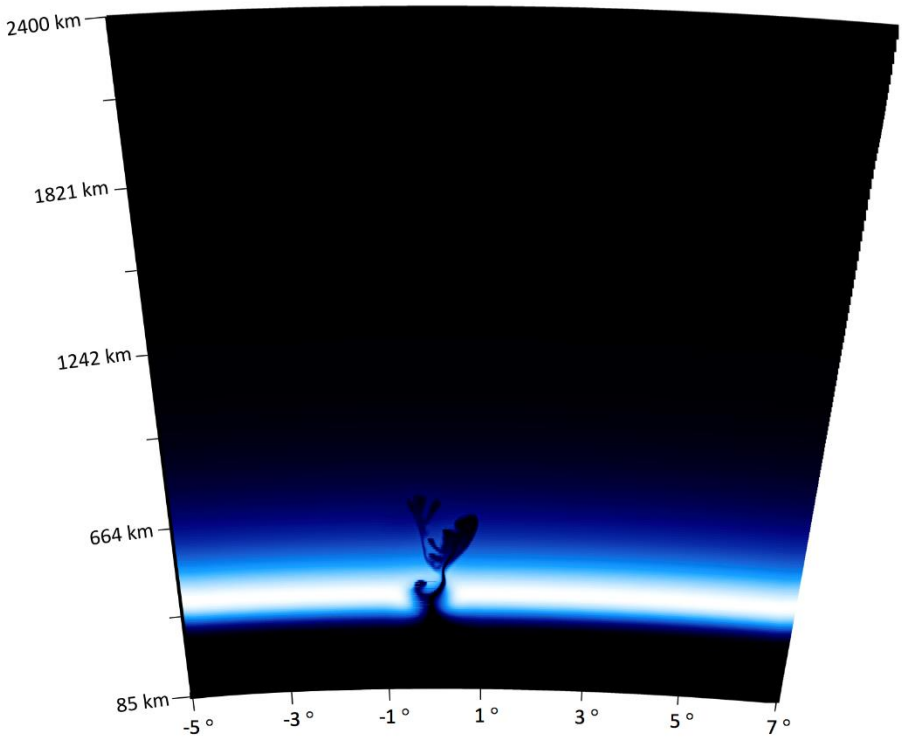

Figure 19: Cross-section at 0° latitude of electron density output from SAMI3. Horizontal direction is longitude and vertical direction is altitude.

The SAMI3 model was sampled using a nearest neighbor approach in which the look vectors were broken up into discrete sections and the electron density at the nearest SAMI3 model grid point was taken as the value at that point. The electron density given by the output from the SAMI3 model is given cm^{-3} and in order to convert to brightness values registered by the FUV instrument, the line-of-sight integral must be performed using Equation 5 (e.g. England et al. 2008).

$$I_{RR} = \frac{1}{10^6} \int \alpha_{1356}\,(T_e) N_e [O^+] ds \tag{5}$$

The O^+ density in Equation 5 is assumed to be equal to the electron density because O^+ is the dominant species in this region and the radiative recombination rate, α_{1356}, is 7.3×10^{-13} at 1160K (England et al., 2008). This equation only takes into account FUV emissions from radiative recombination of O^+ and excludes any contribution of brightness from mutual neutralization of O^+ and O^-. This is done to eliminate the added complexity of sampling an additional model, because the SAMI3 model does not model O^-, and the FUV emissions produced by mutual neutralization only account for a small fraction of the total brightness shortly after sunset, when plasma bubbles are most likely to occur. In Figure 20, a few cross-section profiles of raw electron density at different ranges from the spacecraft show the intricate structuring of the plasma bubble. The final line-of-sight integrated brightness image detected by ICON's FUV instrument for these electron density profiles can be seen in Figure 21a.

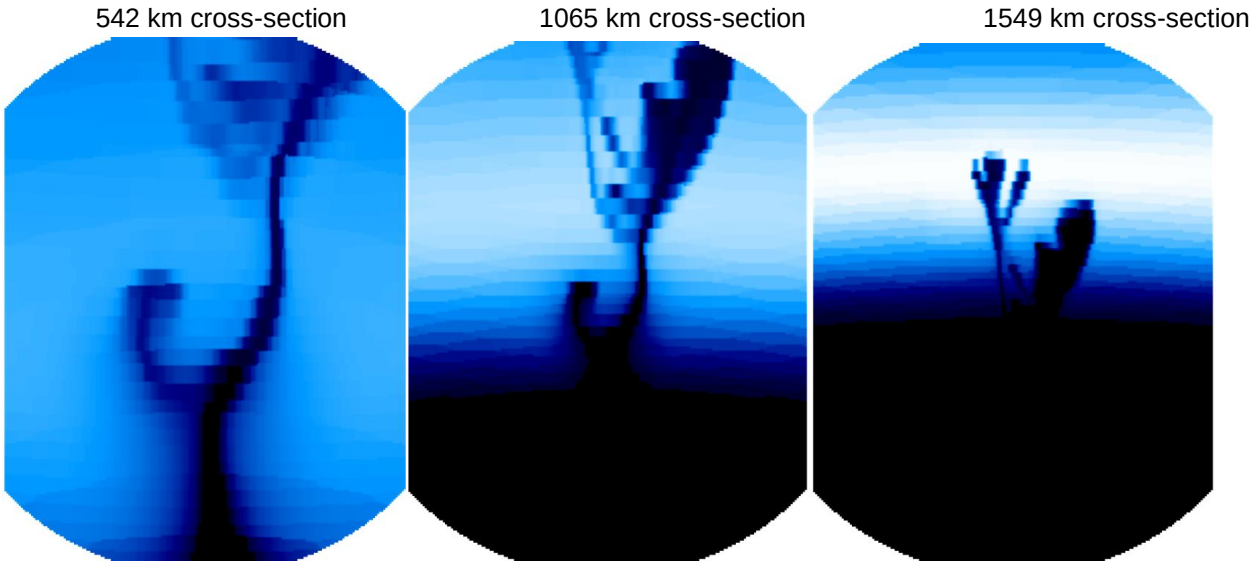

Figure 20: a) Cross-section of electron density at 542 km radially from ICON b) Cross-section of electron density at 1065 km radially from ICON c) Cross-section of electron density at 1549 km radially from ICON. All three images are on the same color scale, where the white represents the highest density plasma at 2.326×10^6 cm^{-3}, and the black represents the lowest density plasma at 0 cm^{-3}.

2.3.1 Simulation Results

The simulation was first run assuming perfect imaging of the incident FUV light throughout the TDI process. The observed FUV scene at the beginning, middle, and end of image integration can be seen in Figure 21. The plasma bubble is distinguished by the dark regions of depleted plasma and shifts left and rotates in the image as the spacecraft orbits around the Earth. Using the TDI process outlined earlier, images similar to these from 100 time steps during image integration are transformed onto a surface with constant linear motion and then co-added together to form the limb and sub-limb images.

Figure 22a shows the resultant limb and sub-limb image after image integration. Also shown in Figure 22, part b, is the same simulation run without compensation for the motion blur encountered during image integration. It is clear the motion compensation in the TDI process preserves the plasma gradients and fine structuring of the bubble. In particular, the two pronged feature in the sub-limb image of Figure 22a has been smoothed out and is only visible as a single pronged channel in Figure 22b. The sharp gradients in the limb image of Figure 22a are also smoothed in Figure 22b. This will be examined in further detail in the next section.

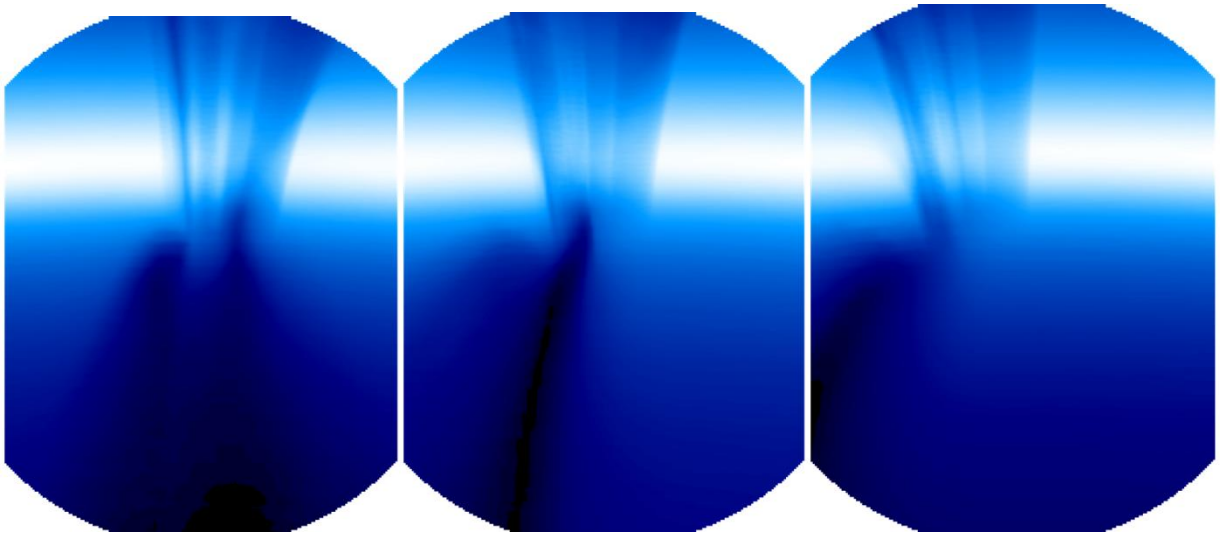

Figure 21: a) Observed FUV scene at beginning of image integration. b) Observed FUV scene at middle of image integration. c) Observed FUV scene at end of image integration. Each image is scaled to fit the entire color range with black representing the lowest brightness, near zero Rayleighs, and white representing the highest brightness at roughly 475 Rayleighs.

The perfect imaging assumed for the simulation is not an accurate representation of the amount of FUV light that is detected on the CCD. Incoming far-ultraviolet photons enter the spectrographic imager through the periscope and goes through a series of mirrors and gratings that filter out any light with a wavelength other than 135.6nm. The light then hits a FUV photocathode where electrons are emitted that are multiplied through a stack of two MCPs. The electrons are then converted back to visible light through a phosphorus screen and the visible light is finally detected on the CCD. The CCD has a resolution of 1024 x 1024 pixels, however these are binned into a 256 x 256 array for image processing. All of these processes introduce a number of sources of noise into the system. First there is a possibility that an unwanted wavelength of light can be scattered onto the detector. There is also the possibility of dark current causing a pixel to read a count even in darkness due to thermal fluctuations. The analog to digital converter also has noise associated with it each time it measures the charge in each pixel, known as read noise. These three sources of noise are minimized by the design of the spectrographic imager and can be neglected. Each FUV photon is effectively multiplied six orders of magnitude and produces a charge of ~900 e^- on the detector. For this reason, any incorrect wavelength light that is scattered onto the detector will be several orders of magnitude less bright than the far-ultraviolet light. Dark current noise can be neglected because the threshold to register a count on the detector is set to ~400 e^- and any dark current produced can be assumed to be less than this. The read noise in a measurement of 900 e^- is negligible when compared to the 400 e^- threshold. Finally, there is shot noise, which is the probability that an incident photon on the CCD will be counted. This type of noise is significant, especially at low levels, and must be modeled in our simulated viewing of a plasma bubble to accurately test the resolution of the images. The shot noise can be modeled as a Poisson distribution on the counts detected on each raw image that make up a TDI image.

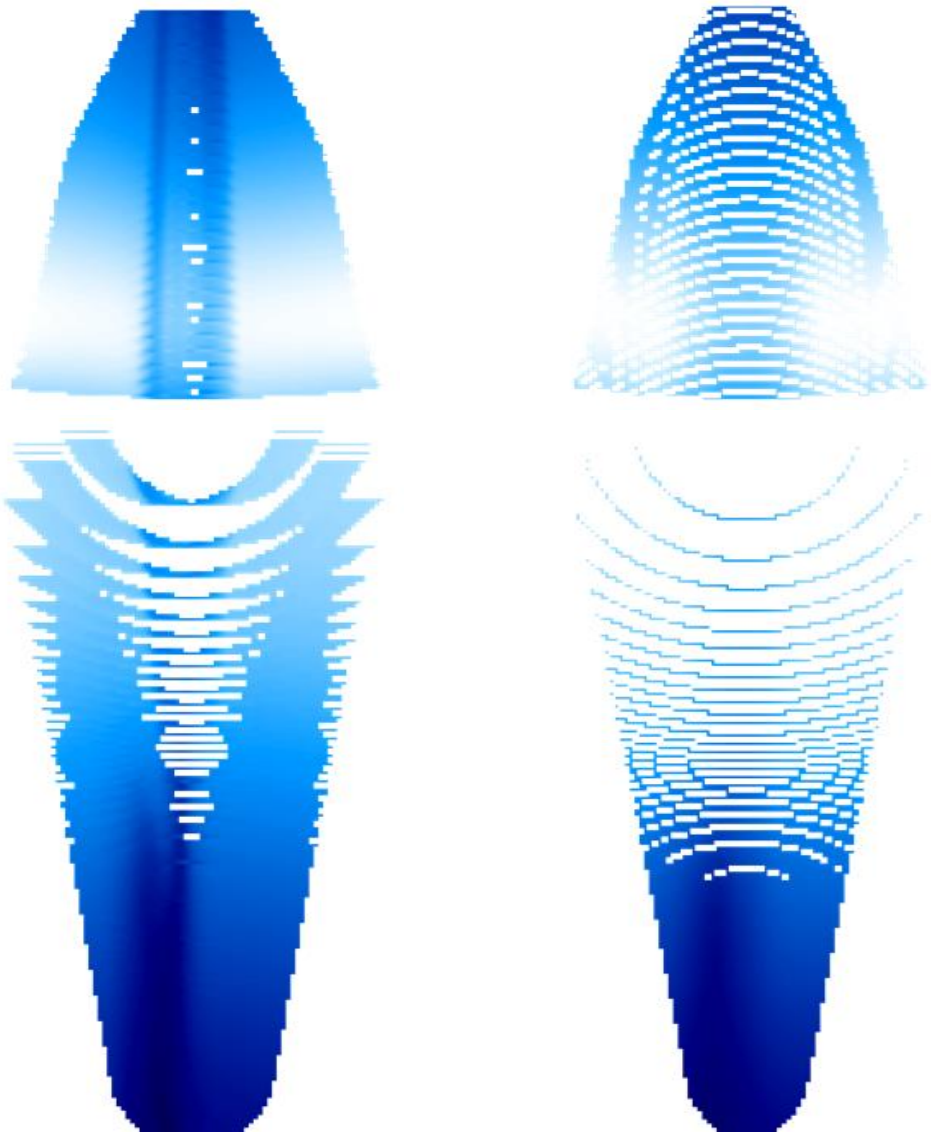

Figure 22: a) Limb and sub-limb of idealized simulation viewing of plasma bubble from SAMI3 model output (left). b) Limb and sub-limb of simulation viewing of plasma bubble without motion compensation (right). Both sets of limb and sub-limb images share a color scale between them, with white representing the brightest emissions and black representing the dimmest emissions.

To incorporate noise into the simulation, brightness values from the idealized model were converted to counts using the relation detailed in Mende et al. (2017) and shown in Equation 6.

$$Counts = [Brightness\ (kR)] * [Time\ (s)] * [4.5\ counts/s/kR] \quad (6)$$

The measured counting rate for the short wave channel is 49 counts/science pixel/s/kR (Mende et al., 2017). Science pixels as defined in the paper are 32 times larger than the pixels we are concerned with during the TDI process. Therefore, each pixel in output memory for the TDI process has a count rate of 4.5 counts/pixel/s/kR. (Mende et al., 2017). Then the RANDOMN

function in IDL with a Poisson distribution was used to simulate the effects of shot noise. During solar max, FUV brightness values are anticipated to have a maximum around 400-500 Rayleigh's, this corresponds to roughly 27 counts over the entire 12 second integration period or 0.27 counts for a single raw image. The detector can only output counts in whole integer values, however, when multiple raw images are co-added together non-integer values can result. This leads to the noise on the individual frames of the TDI being significant. Figure 23 shows the first raw image in the TDI process, both the idealized version and what is actually detected by the CCD. In the version with noise is it very difficult to make out the plasma bubble, this is why the TDI process is crucial to viewing plasma bubbles from ICON's FUV imager.

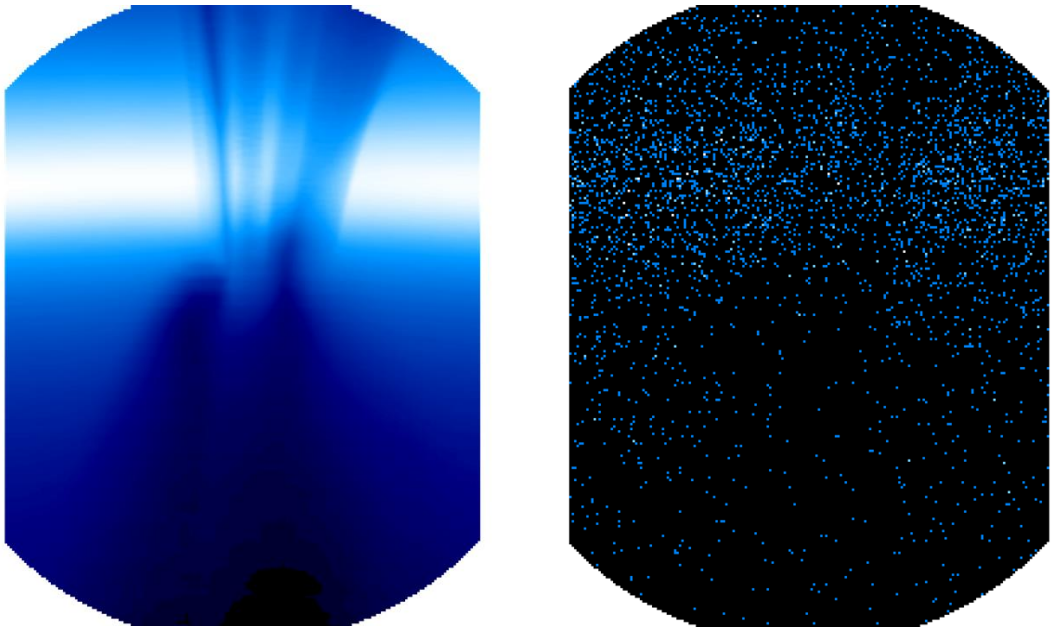

Figure 23: a) Idealized observed scene of simulated plasma bubble. b) Simulated observed scene with shot noise. The color scale for the idealized version is the same as above and for the noise version black symbolizes a reading of zero, dark blue a reading of one, all the way up to white a reading of four counts.

The simulation was repeated accounting for shot noise and Figure 24 shows the resultant limb and sub-limb images. The sharp plasma gradients and fine structuring of the bubble are degraded slightly, however the main features of the plasma bubble are still visible. The two pronged feature in the sub-limb is still visible and the depletions in the limb image have not been significantly smoothed out.

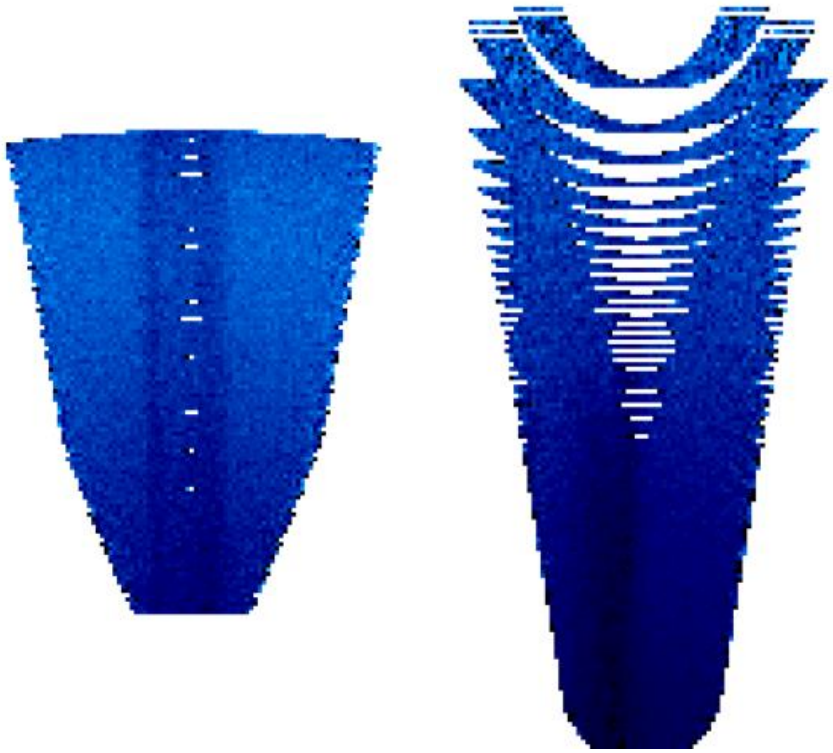

Figure 24: Limb and sub-limb images of simulated viewing of a plasma bubble with shot noise. Both images are on the same color scale with black representing the lowest brightness and white representing the highest brightness.

2.4 Quantitative Comparison of Imaging Techniques

To qualitatively assess the performance of the TDI process, metrics have been developed to compare the characteristics of the plasma bubble in each of the three limb and sub-limb image pairs presented in the previous section. These will be compared against the "true" characteristics of the plasma bubble, taken from a stationary spacecraft's point of view at the beginning of image integration. We will use three different metrics to characterize the plasma bubble. In the limb image we will look at the brightness gradient at the left and right walls of the plasma bubble. In most cases it has been observed that the western wall has a steeper gradient than the eastern wall in a plasma bubble (Mendillo and Baumgardner, 1982). In our simulation the right wall of the observed bubble represents the western wall because during model formation, the orientation of the bubble in the SAMI3 output received from Dr. Joe Huba was flipped. However, we do not expect to see this characteristic of plasma bubbles in our simulation because of a couple of factors. First, we are viewing the plasma bubble from a different vantage point where our line-of-sight has varying latitude and altitude convolved together. As opposed to ground based observations where only altitude is varied along a line-of-sight. Secondly, the SAMI3 output snapshot used to make the model is from early in the post-sunset period and the degradation of the eastern wall has not begun to happen yet. This is particularly evident in Figure 20, where you can see that the plasma bubble is taller on the left side and as the line-of-sight gets farther from the spacecraft the part of

the image where the deep depletion of plasma on the right side was, is replaced with ambient F-peak plasma. Through integration along the line-of-sight, the intensity of the depletion seen at the western wall of the plasma bubble is reduced. In the sub-limb image because the brightness is much dimer, we will look at the overall width and relative brightness drop across the plasma bubble for our quantitative metrics.

All cross-section profiles are the average of three rows of pixels in their respective images. This is done to eliminate missing data for some of the TDI images and keep a consistent analysis across all images. Some TDI images shown in previous sections have units of Rayleighs, however for comparison with the TDI images that account for shot noise, all TDI images were convert to counts detected by the CCD using Equation 6. The calculations for the case of TDI with noise were calculated as the mean of 15 simulations while applying a random Poisson distribution of noise. The uncertainty in these calculations is the standard deviation in the data set of 15 simulations.

Shown in Figure 25 are selected cross-sections of brightness profiles of the limb and sub-limb images, where the idealized TDI is shown in blue, TDI without motion compensation is shown in red, TDI with shot noise is shown in black, and the true airglow brightness detected is shown in green. Shot noise becomes more significant near the ends of the cross-sections because there is less averaging at these locations during the TDI process.

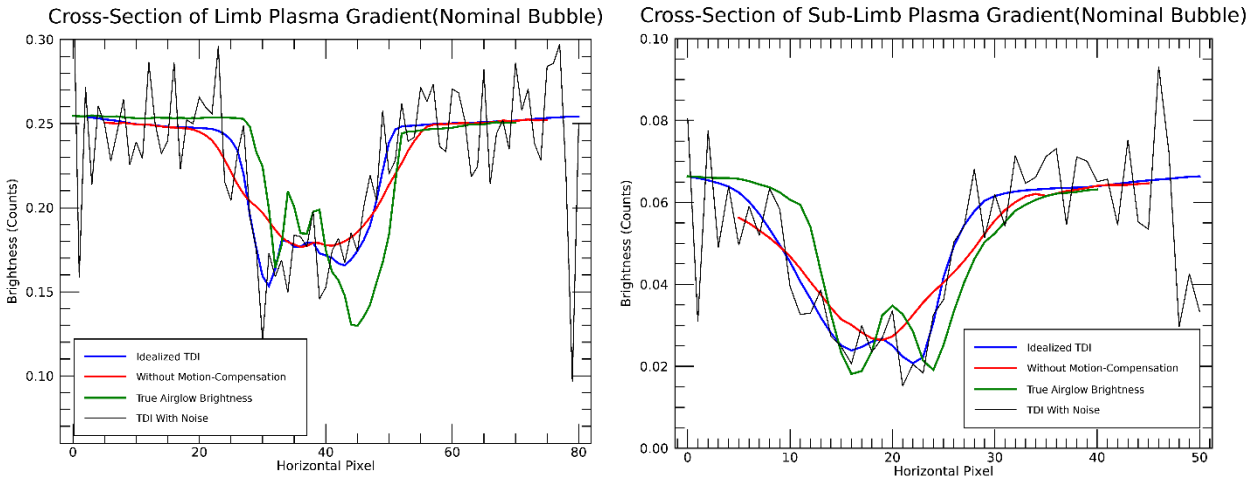

Figure 25: Cross section plots of the limb and sub-limb counts detected for idealized TDI, TDI with noise, TDI without motion compensation, and the 'true' airglow brightness of the observed plasma bubble.

	TDI without Motion Compensation	Idealized TDI	TDI with Shot Noise	True Airglow Brightness
Brightness Gradient in Left Wall of Limb Image (counts/pixel)	0.0072	0.0219	0.0242 ± 0.0057	0.0301
Brightness Gradient in Left Wall of Limb Image (Rayleigh/km)	1.6678	5.0680	5.6047 ± 1.3152	6.9623
Brightness Gradient in Right Wall of Limb Image (counts/pixel)	0.0071	0.0173	0.0230 ± 0.0041	0.0300
Brightness Gradient in Right Wall of Limb Image (Rayleigh/km)	1.6337	4.0159	5.3254 ± 0.9377	6.9454
Width of Plasa Bubble in Sub-limb Image (pixel)	15	15	14.40 ± 0.91	15
Width of Plasa Bubble in Sub-limb Image (km)	121.8	119.0	115.4 ± 4.87	116.95
Relative Brightness Drop across Plasma Bubble in Sub-limb Image (%)	52.66	62.11	61.72 ± 2.65	58.40

Table 2: Calculated metrics of the observed simulated nominal plasma bubble located at 0° longitude with a turret view-angle of 0°, along with the true characteristics of the plasma bubble (right column).

The metric used for the limb image, was the brightness gradient seen at the left and right walls of the plasma bubble. This was calculated using the DERIV function in IDL, which uses a quadratic Lagrangian interpolation to compute the derivatives. A low-pass filter with a cutoff frequency of half the Nyquist frequency was applied to the limb brightness cross-section with noise. The gradients are expressed in counts per pixel, as well as, Rayleighs per kilometer in Table 2. The brightness gradients at the walls of the plasma bubble in the limb image for the TDI with noise are similar to those from the idealized TDI. However, they were calculated to be slightly greater in magnitude, which is closer to the true brightness gradients at the walls of the plasma bubble. The brightness gradients calculated for TDI without motion compensation are significantly lower than either the idealized TDI or TDI with noise. The true gradient in the left wall of the plasma bubble is slightly greater than that in the right wall. This remains true for the gradients measured in all cases, although the uncertainty in the measurement with noise at the left wall is greater.

For the metrics used on the sub-limb image, the width of the plasma bubble was calculated as the number of pixels that were below a threshold of 30 percent drop in brightness relative to ambient plasma brightness. A threshold of 30 percent was used because in a survey of the last 30 years of imaging observations of plasma depletions, they were normally depleted by 30-50 percent (Makela, 2006). The ambient plasma brightness was taken as the average brightness of the true airglow to the right of the plasma bubble. The bubble width in kilometers was calculated by linearly interpolating between pixels and assuming each pixel is 8 km wide. The relative brightness

drop for each sub-limb image was calculated as the mean brightness in the middle of the plasma bubble over the mean ambient plasma brightness to the right of the bubble for each cross-section. Shown in Table 2 are the metrics for the limb and sub-limb images for all four cases. The width of the plasma bubble in kilometers agrees fairly well between all four case, with the TDI without motion compensation having the largest bubble width and the TDI with noise being the closest to the true bubble width. Bubble width measured in pixels is the same for every case except the TDI with noise, and the true value is still with the uncertainty of that measurement. For relative brightness drop across the bubble, the idealized TDI and TDI with noise are similar and slightly higher than the true brightness drop, while the brightness drop for the case of TDI without motion compensation is lower than the true brightness drop.

2.5 IDL Code and NetCDF Output Files

Onboard the spacecraft the TDI process is implemented by FGPAs and during the nightside of the orbit, a limb and sub-limb image are created every 12 seconds. These images are received on the ground in two files, a L1 limb file and a L1 sub-limb file, both in NetCDF format. The level 1 files contain all the respective images for a given day, as well as, information about the LUT table used to create that image and the turret view-angle at the time of image creation. The L0 FUV ancillary file is also needed to process the images and determine the geodetic coordinates of the scene. The ancillary file contains information about the position of the spacecraft and true orientation of the instrument during image formation.

A code was developed in IDL to process the received FUV TDI images and produce a L2 data product containing information about the geometry of the observed scene, including the geodetic coordinates of every active pixel. This data product is written in the NetCDF format and a list and description of all the variables in the L2 file can be seen in Table 3.

Variable Name	Description	Units
EPOCH	Time corresponding to the center of the exposure in milliseconds, since Jan 1 1970.	milliseconds
ICON_L2_FUVA_LIMB_TDI_ALTITUDE	Altitude of tangent point seen at corresponding pixel in TDI image.	Kilometers
ICON_L2_FUVA_LIMB_TDI_LATITUDE	Geodetic latitude of tangent point seen at corresponding pixel in TDI image.	Degrees
ICON_L2_FUVA_LIMB_TDI_LONGITUDE	Geodetic longitude of tangent point seen at corresponding pixel in TDI image.	Degrees
ICON_L2_FUVA_LIMB_TDI_LOOK_UNITVECTORS_ECEF	Unit vectors pointing from spacecraft positon at center time of TDI image to tangent point of corresponding pixel.	Unit-less
ICON_L2_FUVA_LIMB_TDI_TANGENT_POINT_RANGE	Distance from spacecraft to tangent point of corresponding pixel in TDI image.	Kilometers
ICON_L2_FUVA_LIMB_TDI_TANGENT_POINTS_ECEF	ECEF position of tangent point of corresponding pixel in TDI image.	Kilometers
ICON_L2_FUVA_LIMB_TDI_SC_ALTITUDE	Altitude of spacecraft at the center time of the TDI image.	Kilometers
ICON_L2_FUVA_LIMB_TDI_SC_LATITUDE	Geodetic latitude of spacecraft at the center time of the TDI image.	Degrees
ICON_L2_FUVA_LIMB_TDI_SC_LONGITUDE	Geodetic longitude of spacecraft at the center time of the TDI image.	Degrees
ICON_L2_FUVA_LIMB_TDI_SC_POSITION_ECEF	ECEF position of the spacecraft at the center time of the TDI image.	Kilometers
ICON_L2_FUVA_LIMB_TDI_TIME_UTC	UTC string of corresponding center time of the exposure.	String

Table 3: List of variables in L2 data product produced by IDL code. Variable names are those for the limb file, the sub-limb file has similar variable names with “SUBLIMB” instead of “LIMB” in them.

There are two versions of the code, one for UC Berkeley’s data pipeline that processes an entire day’s worth of images and one for ad hoc data analysis of a specific sub-set of TDI images. Both versions read a plain text file, nominally named ‘Information.txt’, for instructions on the input files to use and specific time period for that day which the L2 data product is needed for the case of ad hoc analysis. The UC Berkeley code is called automatically and produces two system check files per day of images processed, to quickly identify if the program is running correctly. Examples of the typical expected postscript files produced can be seen in Figure 26 and Figure 27. In Figure 26, the time histories of the spacecraft latitude and longitude can be seen alongside the latitude and longitude of a selected pixel in the TDI limb and sub-limb images. These time histories should follow each other closely and gaps in the data represent times on the dayside when TDI is not used. For a northward pointing FUV instrument, the selected pixel latitude should be greater than the spacecraft latitude. The longitude of the selected pixel relative to the spacecraft’s longitude is dependent on the turret view-angle during image creation. In Figure 27, sample contour plots of the latitude and longitude of the limb and sub-limb images is shown for an interior time step. The limb longitude contour plot should have similar orientation and values as the sub-limb longitude contour plot, and equivalently for the latitude profiles.

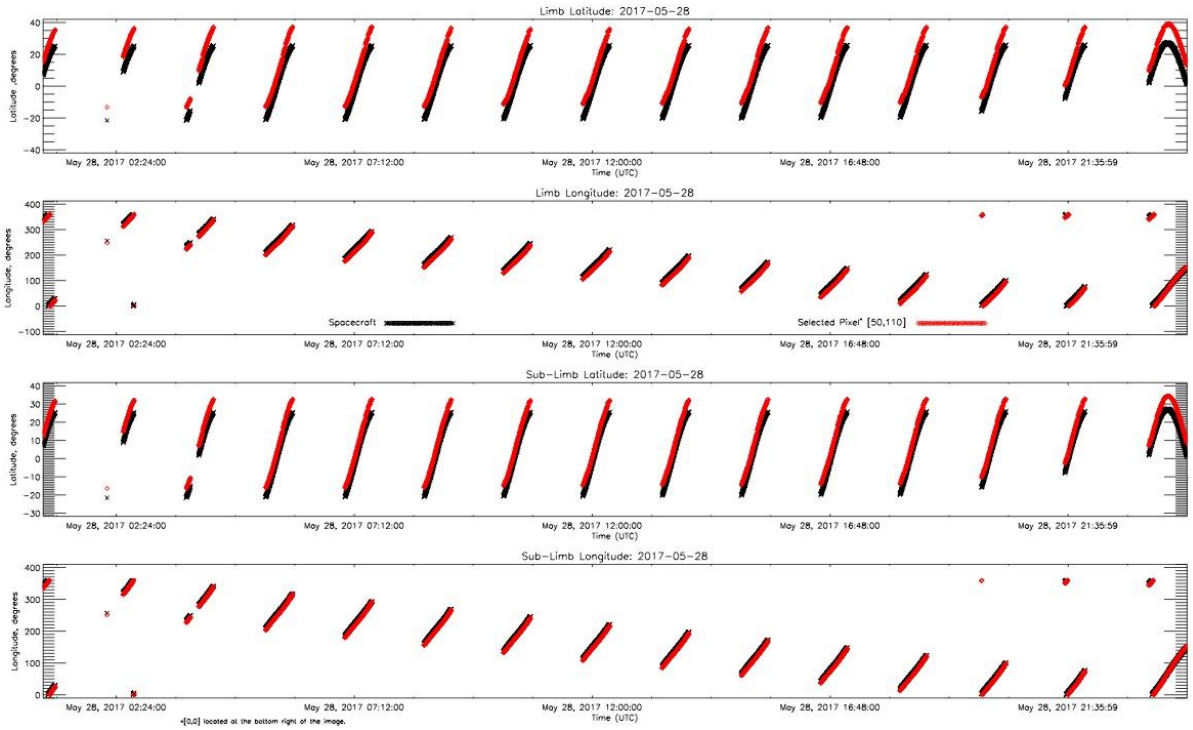

Figure 26: Sample output postscript file containing time histories of the spacecraft latitude and longitude (black) and latitude and longitude of a selected pixel in the limb and sub-limb images (red). Data is for a simulated full day, where the gaps represent daytime use of the FUV instrument.

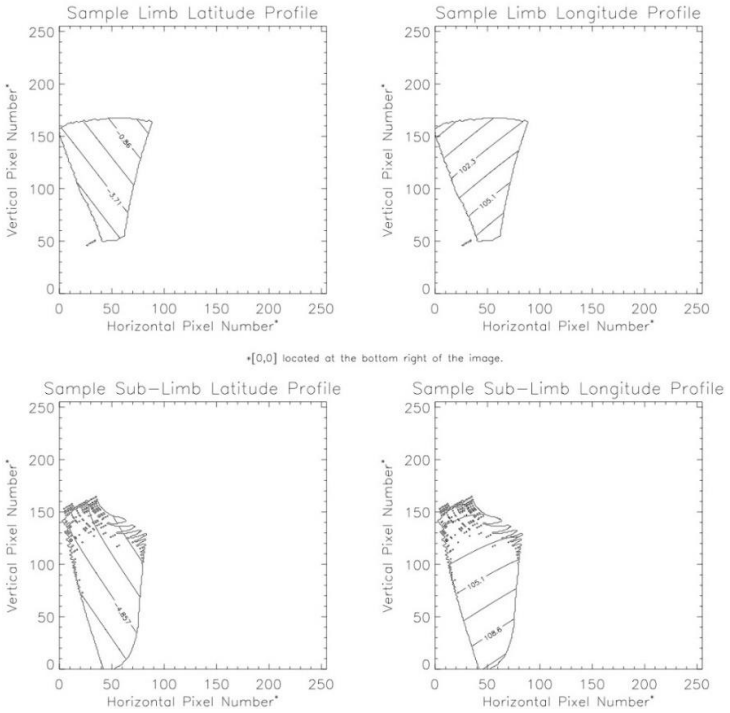

Figure 27: Sample output postscript file containing contour plots of latitude and longitude profiles for a representative TDI image processed by the code. Longitude and latitude profiles from the limb and sub-limb should match rough orientation and values.

The variable-range TDI method outlined in this chapter will be used on additional simulated data in Chapter 3. We will repeat the simulation performed in Section 2.3 three times to gain knowledge about the capabilities and limitations of the TDI process to measure bubble widths, relative brightness drops across the bubble, and gradients at the walls of the bubble. This is done because due to delays in ICON's launch no in-flight data has become available. To examine in-flight data of this spread-F phenomena, we will look at data from the Global-scale Observations of the Limb and Disk (GOLD) mission and gather information about typical bubble widths and relative brightness drops across bubbles, currently observed. In Chapter 4, the variable-range TDI process will not be used to produce this data and a different method will be used to present the GOLD data.

3 SAMI3 Model Output Simulation Sensitivity Study

In this chapter the simulation performed in section 2.3 will be repeated for three different scenarios of viewing a plasma bubble, with varying conditions during image integration. These three simulations allow us to demonstrate the effectiveness of the TDI process, since no in-flight data has become available from ICON. An analysis will be performed on the results to determine the capabilities and limitations of the TDI process to detect a plasma bubble. The TDI process described in section 2.2 will be used to produce the limb and sub-limb images and the same metrics used in section 2.4 will be used to compare each scenario. Due to significant computational time needed to reproduce the simulated images, only one parameter of the simulation will be altered at a time and the effects of combinations of varying parameters will only be inferred from these results. The three scenarios consist of one with a plasma bubble that has half the width of the original simulated plasma bubble, one observing the plasma bubble at a turret view-angle of positive 9°, and one observing a plasma bubble during typical solar minimum conditions.

3.1 Half-width Plasma Bubble Simulation

The scenario in which a plasma bubble with half the width as the original simulation is observed, tests the ability of the TDI process to recover small spatial features and sharp gradients. The original SAMI3 output was compressed longitudinally to create the model used for this simulation. A cross-section of the model at 0° latitude can be seen in Figure 28.

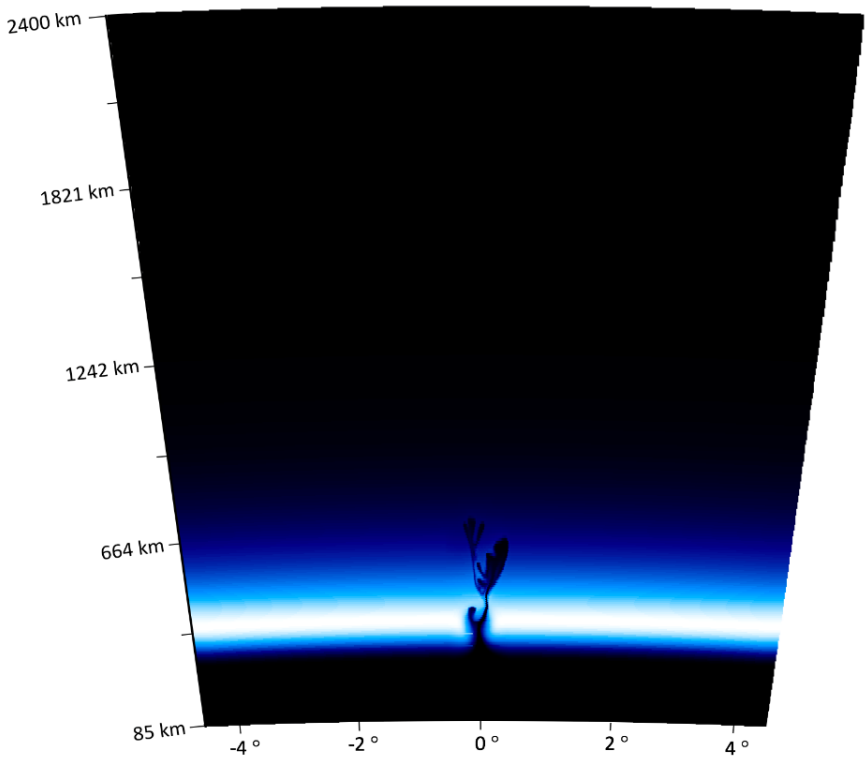

Figure 28: Cross-section of the SAMI3 output model used in the half-width plasma bubble simulation. The cross-section is at 0° latitude and the horizontal axis represents longitude. Brighter regions represent higher density plasma.

The plasma bubble only spans longitudinally from -0.5° to 0.5° longitude, as opposed to -1° to 1° longitude in the original simulation, however the height and shape of the plasma bubble remain the same. This was done to reduce the east-west bubble dimension from roughly 120 km to 60 km across. This is in line with observations referenced in (Makela, 2006) of the low-end of bubble widths observed during the typical spread-F season and outside of it, respectively. The orbit of the spacecraft and integration period remain the same, with the spacecraft having a circular orbit 575 km above the equator and the image integration beginning at 0° longitude and lasting 12 seconds. The resulting limb and sub-limb images of the simulated image integration for the idealized TDI and TDI with noise can be seen in Figure 29. The plasma bubble visible in both sets of images is much narrower than that seen in the original simulation. The overall presence of the bubble is still visible, however some of the structuring, especially the two-pronged feature in the sub-limb image with noise is lost.

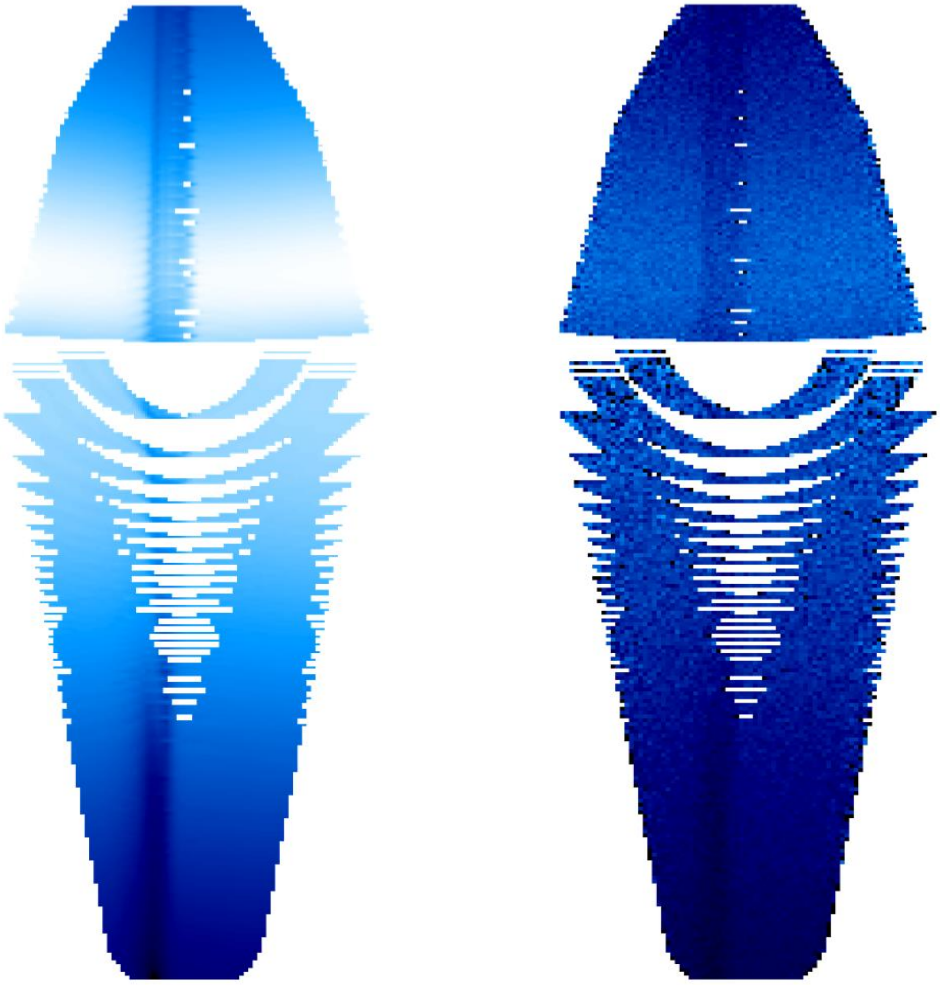

Figure 29: a) Limb and sub-limb images for idealized TDI of the half-width plasma bubble simulation. b) Limb and sub-limb images using TDI with noise of the half-width plasma bubble simulation. Both sets of limb and sub-limb images share a color scale between them, with white representing the brightest emissions and dark blue representing the dimmest emissions.

The width of the plasma bubble is expected to be half of the original simulation, yet the relative brightness drop across the bubble is not expected to change. Therefore, the gradients at either wall of the plasma bubble are expected to be twice that compared to the original simulation. A cross-section of the brightness profiles for the limb and sub-limb images can be seen in Figure 30. The four lines represent the idealized TDI, TDI without motion compensation, TDI with noise, and the true airglow brightness. The same region was selected for the cross-sections as in the original simulation for the best comparison between the two simulations. The calculated metrics for the limb and sub-limb images for all four cases of the half-width plasma bubble simulation are shown in Table 4. The results from the original simulation are also shown in blue parentheses in Table 4 for easy comparison.

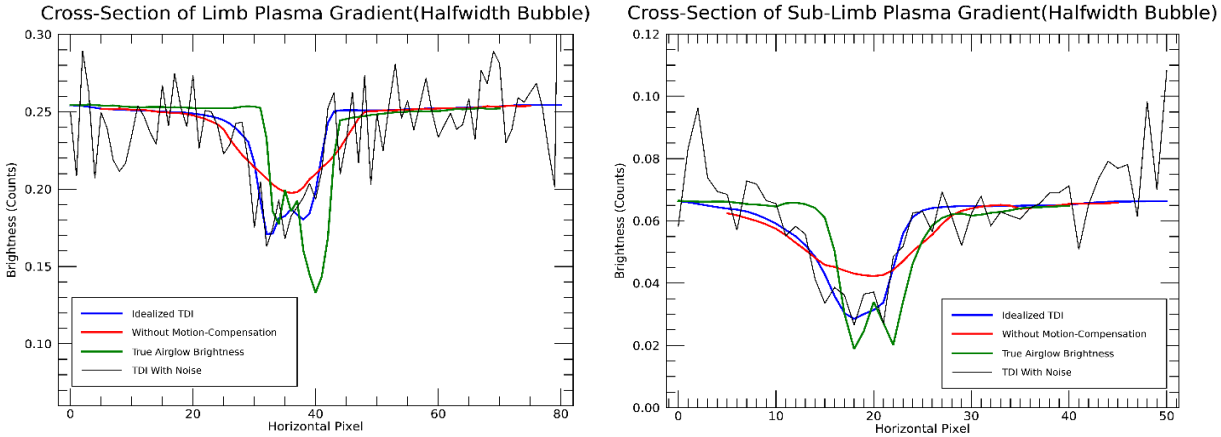

Figure 30: Cross-section plots of the limb and sub-limb counts detected for idealized TDI, TDI with noise, TDI without motion compensation, and the 'true' airglow brightness of the observed plasma bubble in the half-width simulation.

	TDI without Motion Compensation	Idealized TDI	TDI with Shot Noise	True Airglow Brightness
Brightness Gradient in Left Wall of Limb Image (counts/pixel)	0.0058 (0.0072)	0.0230 (0.0219)	0.0260 ± 0.0075 (0.0242 ± 0.0057)	0.0334 (0.0301)
Brightness Gradient in Left Wall of Limb Image (Rayleigh/km)	1.3357 (1.6678)	5.3183 (5.0680)	6.0197 ± 1.7262 (5.6047 ± 1.3152)	7.7324 (6.9623)
Brightness Gradient in Right Wall of Limb Image (counts/pixel)	0.0063 (0.0071)	0.0222 (0.0173)	0.0227 ± 0.0048 (0.0230 ± 0.0041)	0.0389 (0.0300)
Brightness Gradient in Right Wall of Limb Image (Rayleigh/km)	1.4548 (1.6337)	5.1430 (4.0159)	5.2560 ± 1.1090 (5.3254 ± 0.9377)	9.0149 (6.9454)
Width of Plasa Bubble in Sub-limb Image (pixel)	6 (15)	8 (15)	7.33 ± 1.11 (14.40 ± 0.91)	7 (15)
Width of Plasa Bubble in Sub-limb Image (km)	49.99 (121.8)	59.44 (119.0)	58.65 ± 7.58 (115.4 ± 4.87)	61.20 (116.95)
Relative Brightness Drop across Plasma Bubble in Sub-limb Image (%)	33.56 (52.66)	52.57 (62.11)	51.72 ± 2.32 (61.72 ± 2.65)	58.13 (58.40)

Table 4: Calculated metrics of the observed simulated plasma bubble with half width located at 0° longitude with a turret view-angle of 0°, along with the true characteristics of the half-width plasma bubble (right column). Results from original simulation shown in blue parentheses.

Comparing Table 4 to Table 2 in Chapter 2, the measured width of the plasma bubble did decrease to about half of the original width as expected, with an uncertainty of 1.11 pixels. The measured relative brightness drop across the bubble was reduced by 16 percent from the original simulation. This demonstrates that the TDI process cannot recover the full depth of the depletion as the bubble's features become smaller. The measured relative brightness drop of 51.72 ± 2.32 percent is still well above the threshold needed to register a plasma bubble. The gradients measured at the bubble walls in the limb image only increased by 7.4 percent in the left wall and slightly decreased in the right wall. The sharper gradients of the narrower plasma bubble were smoothed out by the TDI process and not detectable. Overall, the TDI with noise performed much better than imaging without any motion compensation techniques in this simulation.

3.2 Positive Turret View-Angle Simulation

The scenario in which the plasma bubble from the original simulation is observed at a turret view-angle of positive 9° was performed to demonstrate the effects of misalignment between the instrument's field-of-view and the local magnetic field.

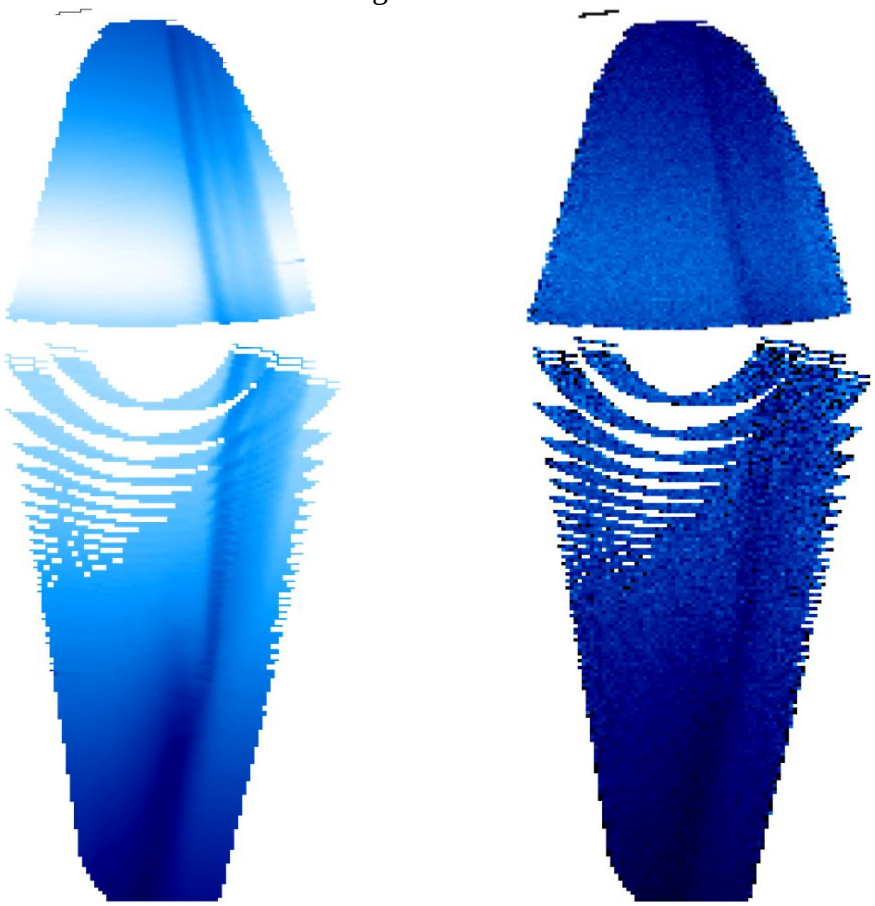

Figure 31: a) Limb and sub-limb images for idealized TDI of the positive turret view-angle simulation. b) limb and sub-limb images using TDI with noise of the positive turret view-angle simulation. Both sets of limb and sub-limb images share a color scale between them, with white representing the brightest emissions and dark blue representing the dimmest emissions.

A turret view-angle of +9° was chosen because the FUV instrument's field-of-view is 18° in the horizontal direction, consequently the FOV can be up to 9° misaligned with the local magnetic field. A turret view-angle of +9° reproduces the conditions in this worst case scenario. Other than a turret view-angle of +9°, the simulation is a duplicate of the original simulation. Additionally, since the instrument is looking slightly behind perpendicular to ram, image integration was started at 0.376753° longitude and continued for 12 seconds to ensure the bubble could be seen in the final limb and sub-limb images.

A cross-section of the SAMI3 output model used in the original simulation and this simulation is shown in Figure 19. The resulting limb and sub-limb images for this simulation, both idealized TDI and TDI with noise can be seen in Figure 31. The plasma bubble can be seen in both sets of images at a slight angle. The two-pronged feature in the sub-limb image is somewhat distinguishable in the idealized TDI version, but is not as discernable in the version with noise. The plasma bubble seen in the limb image is very similar to that from the original simulation.

The quantitative metrics calculated for this simulation will be compared to the 'true' characteristics of the plasma bubble from the original simulation. The calculated metrics should remain the same in this simulation as the original simulation since the same SAMI3 output model was used. Cross-sections of the brightness profiles for the limb and sub-limb images for idealized TDI, TDI without motion compensation, TDI with noise, and the true airglow brightness can be seen in Figure 32. The vertical pixel rows included in the cross-sections were adjusted to account for changes in the position of the plasma bubble in the limb and sub-limb images. This allows us to analyze the same region of the observed plasma bubble as in the other simulations. The metrics for the limb and sub-limb images for all four cases of the positive turret view-angle simulation are shown in Table 5. The results from the original simulation are also shown in blue parentheses in Table 5 for easy comparison.

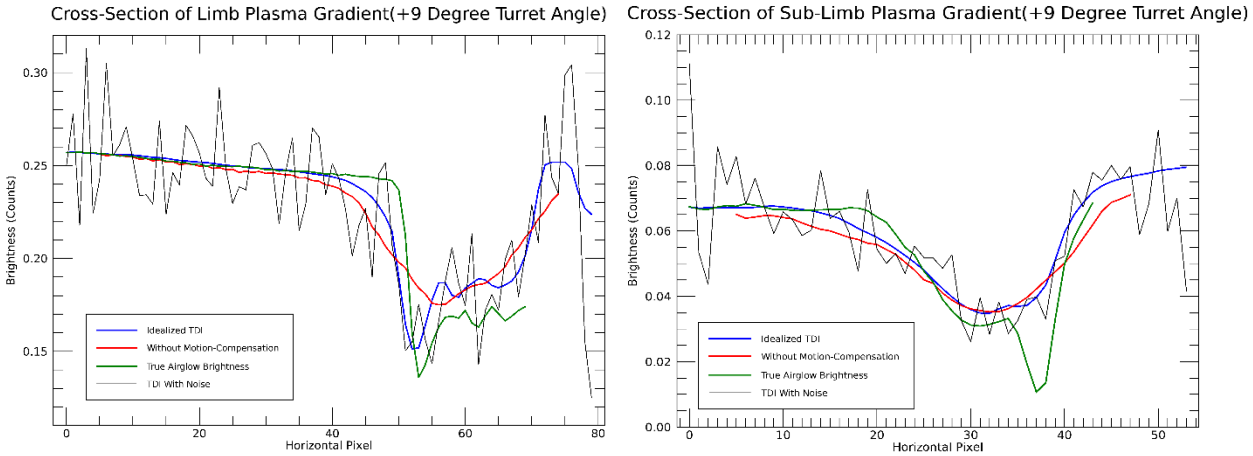

Figure 32: Cross-section plots of the limb and sub-limb counts detected for idealized TDI, TDI with noise, TDI without motion compensation, and the 'true' airglow brightness of the observed plasma bubble in the positive turret view-angle simulation.

	TDI without Motion Compensation	Idealized TDI	TDI with Shot Noise	True Airglow Brightness
Brightness Gradient in Left Wall of Limb Image (counts/pixel)	0.0065 (0.0072)	0.0249 (0.0219)	0.0258 ± 0.0064 (0.0242 ± 0.0057)	0.0301 (0.0301)
Brightness Gradient in Left Wall of Limb Image (Rayleigh/km)	1.5129 (1.6678)	5.7616 (5.0680)	5.9816 ± 1.4707 (5.6047 ± 1.3152)	6.9623 (6.9623)
Brightness Gradient in Right Wall of Limb Image (counts/pixel)	0.0051 (0.0071)	0.0179 (0.0173)	0.0225 ± 0.0064 (0.0230 ± 0.0041)	0.0300 (0.0300)
Brightness Gradient in Right Wall of Limb Image (Rayleigh/km)	1.1794 (1.6337)	4.1451 (4.0159)	5.2093 ± 1.4763 (5.3254 ± 0.9377)	6.9454 (6.9454)
Width of Plasa Bubble in Sub-limb Image (pixel)	14 (15)	13 (15)	13.20 ± 2.21 (14.40 ± 0.91)	15 (15)
Width of Plasa Bubble in Sub-limb Image (km)	116.60 (121.8)	105.65 (119.0)	104.96 ± 15.94 (115.4 ± 4.87)	116.95 (116.95)
Relative Brightness Drop across Plasma Bubble in Sub-limb Image (%)	42.17 (52.66)	45.47 (62.11)	47.67 ± 3.71 (61.72 ± 2.65)	58.40 (58.40)

Table 5: Calculated metrics of the observed simulated nominal plasma bubble located at 0° longitude with a turret view-angle of +9°, along with the true characteristics of the plasma bubble (right column). Results from original simulation shown in blue parentheses.

When compared to Table 2 in Chapter 2, Table 5 shows that the measured width of the plasma bubble in the sub-limb image decreased by 8.33 percent and the uncertainty on the measurement increased by over 100 percent as a result of a turret view-angle of +9°. The measured relative brightness drop across the bubble also decreased by 22.76 percent because of the 9° misalignment between the field-of-view and the local magnetic field. The brightness gradient measured at the left wall of the bubble increased by 6.72 percent and the brightness gradient at the right wall of the bubble decreased by 2.18 percent. Both of these measurements are well within the uncertainty of the measurements from the original simulation. Therefore, the misalignment between the field-of-view and the local magnetic field had little effect on the measured brightness gradients and they are still measured at roughly 80 percent of the true brightness gradient.

3.3 Solar Minimum Conditions Simulation

The solar minimum simulation was performed to test the effectiveness of the TDI process during low emission conditions experienced during solar minimum. Typical F10.7 values for solar maximum and solar minimum were compared and every electron density in the SAMI3 output model was reduced by this factor. A cross-section at 0° latitude of the SAMI3 output model used for this simulation is shown in Figure 33 on the same color scale as Figure 19, the cross-section of the original SAMI3 output model during solar maximum conditions. The orbit of the spacecraft and image integration period used were the same as the original simulation.

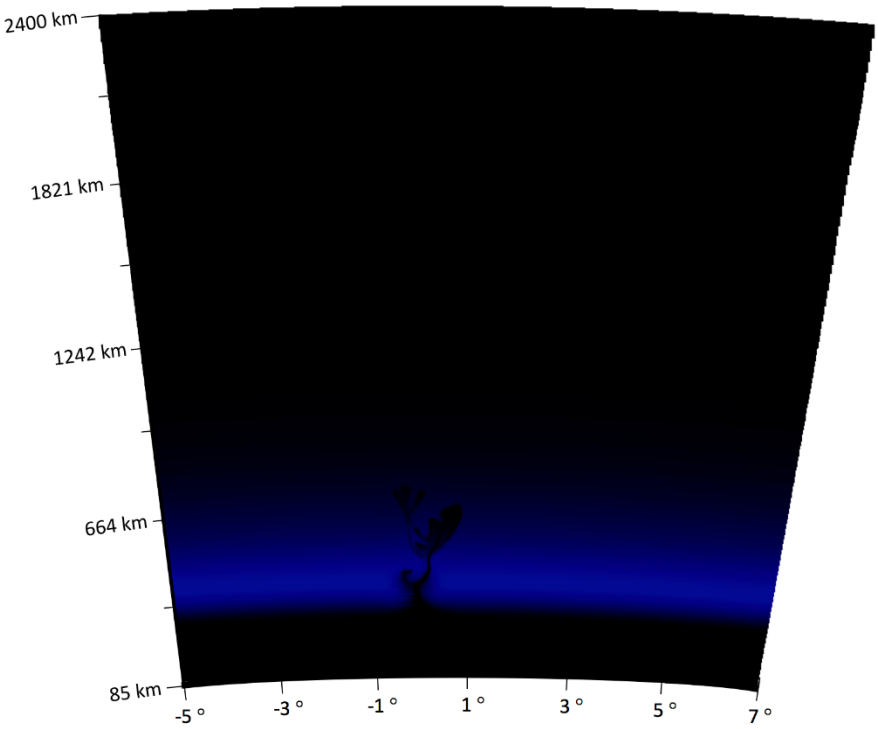

Figure 33: Cross-section of the SAMI3 output data used in the solar minimum simulation. The cross-section is at 0° latitude and the horizontal axis represents longitude. The color scale used is the same as in Figure 19.

The limb and sub-limb images for the solar minimum simulation are shown in Figure 34, for both the idealized TDI and TDI with noise. The color scale for each set of limb and sub-limb images is the same as used in the original simulation (Figure 22 and Figure 24) to highlight the decreased brightness. In the idealized TDI version, the plasma bubble is still visible in the limb and sub-limb images with less contrast than in the original simulation. Conversely, in the version with noise, only a slightly darker region with no discernable shape is detectable in the sub-limb image. There is almost no visible bubble in the limb image, however, from Figure 35, we can tell that the brightness values do drop across the plasma bubble region in the middle of the image.

As with the original and half-width simulations, the same region of the limb and sub-limb images was analyzed when calculating the quantitative metrics used for comparison. For the solar minimum simulation, the plasma bubble width and relative brightness drop across the bubble are expected to remain the same. However, the gradient at either wall of the plasma bubble in the limb image is expected to decrease. Cross-sections of the brightness profiles for the limb and sub-limb images for idealized TDI, TDI without motion compensation, TDI with noise, and the true airglow brightness for the solar minimum simulation can be seen in Figure 35. The calculated metrics for the solar minimum conditions simulation are shown in Table 6. The results from the original simulation are also shown in blue parentheses in Table 6 for easy comparison.

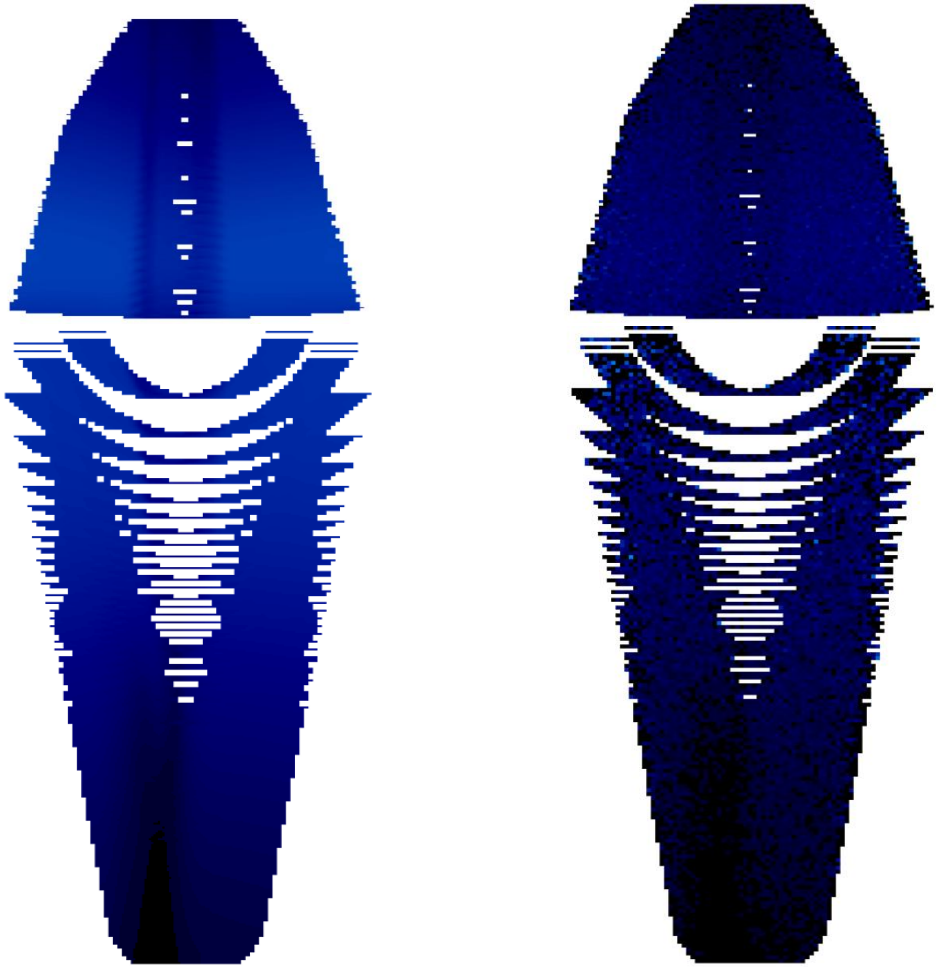

Figure 34: a) Limb and sub-limb images for idealized TDI of the solar minimum simulation. b) limb and sub-limb images using TDI with noise of the solar minimum simulation. Both sets of limb and sub-limb images are on the same color scale as the limb and sub-limb image pairs in Figure 22 and Figure 24, respectively, with white representing the brightest emissions and dark blue representing the dimmest emissions.

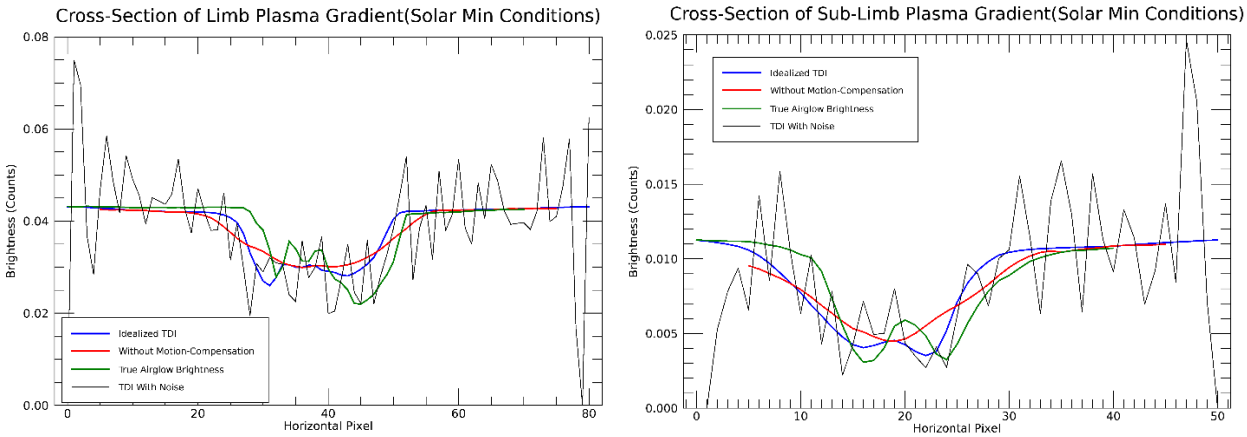

Figure 35: Cross-section plots of the limb and sub-limb counts detected for idealized TDI, TDI with noise, TDI without motion compensation, and the 'true' airglow brightness of the observed plasma bubble in the solar minimum simulation.

	TDI without Motion Compensation	Idealized TDI	TDI with Shot Noise	True Airglow Brightness
Brightness Gradient in Left Wall of Limb Image (counts/pixel)	0.0012 (0.0072)	0.0037 (0.0219)	0.0068 ± 0.0020 (0.0242 ± 0.0057)	0.0051 (0.0301)
Brightness Gradient in Left Wall of Limb Image (Rayleigh/km)	0.2828 (1.6678)	0.8593 (5.0680)	1.5677 ± 0.4618 (5.6047 ± 1.3152)	1.1805 (6.9623)
Brightness Gradient in Right Wall of Limb Image (counts/pixel)	0.0012 (0.0071)	0.0029 (0.0173)	0.0065 ± 0.0017 (0.0230 ± 0.0041)	0.0051 (0.0300)
Brightness Gradient in Right Wall of Limb Image (Rayleigh/km)	0.2770 (1.6337)	0.6809 (4.0159)	1.5147 ± 0.3988 (5.3254 ± 0.9377)	1.1776 (6.9454)
Width of Plasa Bubble in Sub-limb Image (pixel)	15 (15)	15 (15)	14.29 ± 1.59 (14.40 ± 0.91)	15 (15)
Width of Plasa Bubble in Sub-limb Image (km)	121.85 (121.8)	119.02 (119.0)	115.83 ± 11.63 (115.4 ± 4.87)	116.95 (116.95)
Relative Brightness Drop across Plasma Bubble in Sub-limb Image (%)	51.31 (52.66)	61.07 (62.11)	61.80 ± 6.03 (61.72 ± 2.65)	59.50 (58.40)

Table 6: Calculated metrics of the observed simulated plasma bubble during solar minimum conditions, located at 0° longitude with a turret view-angle of 0°, along with the true characteristics of the plasma bubble during solar minimum conditions (right column). Results from original simulation shown in blue parentheses.

Again comparing Table 6 to the original simulation results in Table 2 in Chapter 2, the measured width of the plasma bubble in the sub-limb image decreased by less than one percent, but the uncertainty in the measurement increased by 75 percent. The measured relative brightness drop across the bubble did not significantly change, however the uncertainty in the measurement increased by over 100 percent. Therefore, the observed plasma bubble in solar minimum conditions can still be seen and measured, though there is greater uncertainty in the measurements. The true brightness gradients at both walls of the plasma bubble were reduced by 83 percent during solar minimum conditions. The measured brightness gradient at the left wall of the plasma bubble decreased by 71.9 percent and the measured brightness gradient at the right wall of the bubble decreased by 71.74 percent. The average uncertainty in these measurements did increase by 34.27 percent when compared to their mean value. Because of the noise associated with the TDI process, both measured brightness gradients were higher than the true brightness gradients at the bubbles walls during solar minimum conditions, but both true values are still within the uncertainty ranges of the measured gradients. This demonstrates that the TDI process has limitations on how small of brightness gradients it can detect before the noise associated with the process masks any detectable gradients at bubble walls.

3.4 Sensitivity Study Conclusions

The three simulations give insights into which conditions a plasma bubble would be detectable using the TDI process and FUV instrument onboard ICON. From the half-width plasma bubble simulation, we know that small sized spatial features can be detected, but the full depth of the

depletion can be diminished if the feature becomes too narrow. Additionally, the brightness gradients seen at the walls of the plasma bubble in the half-width bubble simulation were too sharp for the TDI process to measure accurately. The positive turret view-angle simulation informed us that a 9° misalignment between the instrument's FOV and the local magnetic field will cause the measured size and depth of the plasma depletion to be reduced in magnitude and increase the measurement uncertainty. This misalignment however did not affect the TDI process's ability to measure the brightness gradients at both walls of the bubble. The final simulation during solar minimum conditions expressed to us that during decreased emission periods it is still possible to detect the size and depth of the plasma bubble but the uncertainty in the measurements is much greater. Furthermore, the gradients at the walls of the plasma bubble during these periods can become too small that the noise associated with the instrument conceals any discernable bubble wall.

One can infer certain limitations of the TDI process from these findings. For example, the measured depth of the depletion was reduced during the half-width bubble simulation and the uncertainty in the measurement is much more significant during solar minimum conditions. Therefore, it is possible that during solar minimum conditions, the narrow bubble used in the half-width simulation might not be detectable. Additionally, sharp brightness gradients seen in the half-width simulation would likely be unmeasurable because of the magnitude of the noise during solar minimum conditions. In Chapter 4, the models used during these three simulations will be validated through examination of plasma bubbles currently observed by the GOLD mission. The choice of bubble size and solar conditions in the models used to test the capabilities of the TDI process to detect plasma bubbles will be proved to be accurate representations of the variations in ionospheric conditions we expect to encounter.

4 GOLD Observations

In order to contextualize our SAMI3 simulations in the setting of current ionospheric conditions, we will look at data from the Global-scale Observations of the Limb and Disk (GOLD) mission. We will determine if our simulations depict an accurate representation of the variety of characteristics of plasma bubbles currently being observed in the ionosphere. A suitable data set that utilizes variable-range time-delay integration to view plasma bubbles is not available because this is the first time this technique is being employed for this kind of observation. Data from the GOLD mission was selected because, similar to ICON, the instrument on board detects 135.6 nm wavelength light in the far-ultraviolet range to observe plasma bubbles in the nighttime ionosphere and GOLD is currently in orbit. Additionally, the GOLD and ICON missions were intended to fly at the same time to explore the upper atmosphere and ionosphere from two different perspectives. For these reasons, data from the GOLD mission is a natural choice for simulation model validation. In this chapter, data from October 17th, 2018, across 2040 – 2355 UTC, will be examined to determine pertinent characteristics of plasma bubbles currently observed by GOLD. The UTC range selected corresponds to nighttime at the observed scene, given the longitudes GOLD is able to observe. At the time of writing, only a select few nights of GOLD data are publicly available, and October 17th 2018 is one such evening that contains numerous observations of plasma bubbles.

4.1 GOLD Observed Plasma Bubbles

The GOLD mission is a NASA explorer mission aimed at understanding the coupling of Earth's atmosphere and space on a global scale (Eastes et al., 2017). The GOLD image is a hosted payload on the SES-14 satellite in a geostationary orbit over 47.5° W longitude and started collecting data in October of 2018 (Eastes et al., 2017). The images in Figure 36 were created from L1C GOLD data files that contain measured brightness values for each binned pixel. These were projected onto a satellite projection of the Earth and measures were taken to artificially smooth features along magnetic field meridians. This was done because the features we are looking for are known to be approximately aligned with magnetic field meridians and such a smoothing aids with removing pixel-to-pixel variation that may be related to noise associated with energetic particles in the geostationary environment. The images are an integration over a range of wavelengths observed by GOLD to capture the entire emission feature at 135.6 nm. The range of wavelengths used is highlighted in Figure 37, which shows an example emission profile across all wavelengths sampled by GOLD.

A total of ten images were taken by GOLD in nighttime mode on October 17th, 2018, ranging from 1700 local time to 2045 local time at the sub-satellite point. Of these images, nine have discernable plasma bubbles in them which we can examine to determine the characteristic qualities of the observed plasma bubbles. We will look at a total of eleven bubbles that can be seen as clear depletions in brightness compared to the surrounding plasma in three consecutive images and are labeled A through G in Figure 36. Table 7 shows the geodetic longitude and magnetic longitude of each bubble. Plasma bubbles A and A' look as if they are geomagnetic conjugates occurring in

the Equatorial Ionization anomaly region of high density plasma on either side of the magnetic equator. Plasma bubbles B/B', C/C', and D/D' also appear to be geomagnetic conjugate pairs resulting from the electric potential nearly being constant along magnetic field lines and therefore the depletion exists in both hemispheres along the entire flux tube. Equatorial ionospheric plasma bubbles in this region tend to have an average drift velocity of 1° - 5° magnetic longitude per hour (Immel et al., 2004, Park et al., 2007) and during the up to 15 minutes northern and southern images can be apart, we can expect the bubble to move up to 1.25° magnetic longitude. All conjugate pairs we see in the GOLD data are less than 0.5° magnetic longitude apart. Bubbles E, F, and G do not have geomagnetic conjugates that we will examine in this data. From image to image in Figure 36, it is possible to track individual bubbles as they progress eastward with time.

To compare the observed bubbles from GOLD data to those from the SAMI3 model output simulations, we must account for the difference in vantage points between the two observations. GOLD is in a geosynchronous orbit, roughly at 47.5° W longitude. This creates an entirely different perspective where line-of-sight is nearly devoid of any variation in latitude as altitude changes. Whereas, from ICON's perspective in Low-Earth Orbit, variations in latitude and altitude along a line-of-sight are convolved together. This will be addressed in Section 4.2, where the SAMI3 model output used in the original simulation in Section 2.3 will be re-observed using the geometry and vantage point of GOLD.

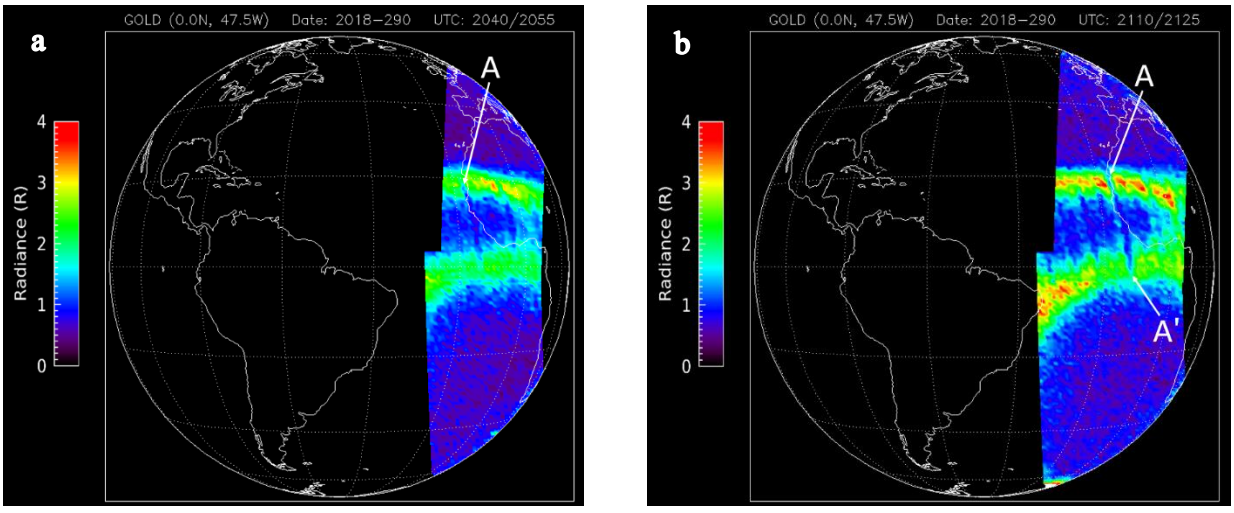

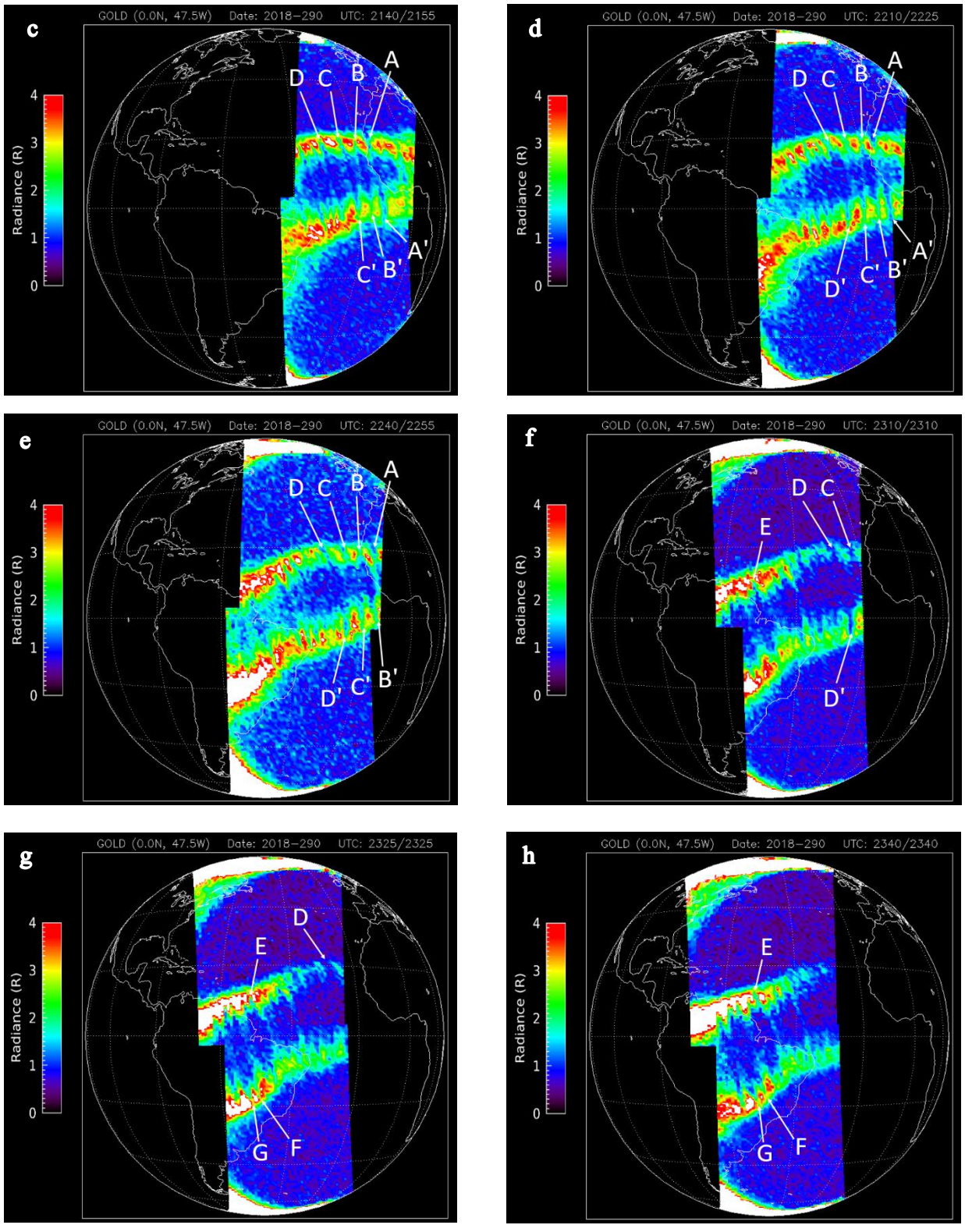
c
GOLD (0.0N, 47.5W) Date: 2018–290 UTC: 2140/2155
Radiance (R)
A
B
C
D
A'
B'
C'
d
GOLD (0.0N, 47.5W) Date: 2018–290 UTC: 2210/2225
Radiance (R)
A
B
C
D
A'
B'
C'
D'
e
GOLD (0.0N, 47.5W) Date: 2018–290 UTC: 2240/2255
Radiance (R)
A
B
C
D
B'
C'
D'
f
GOLD (0.0N, 47.5W) Date: 2018–290 UTC: 2310/2310
Radiance (R)
C
D
E
D'
g
GOLD (0.0N, 47.5W) Date: 2018–290 UTC: 2325/2325
Radiance (R)
D
E
F
G
h
GOLD (0.0N, 47.5W) Date: 2018–290 UTC: 2340/2340
Radiance (R)
E
F
G

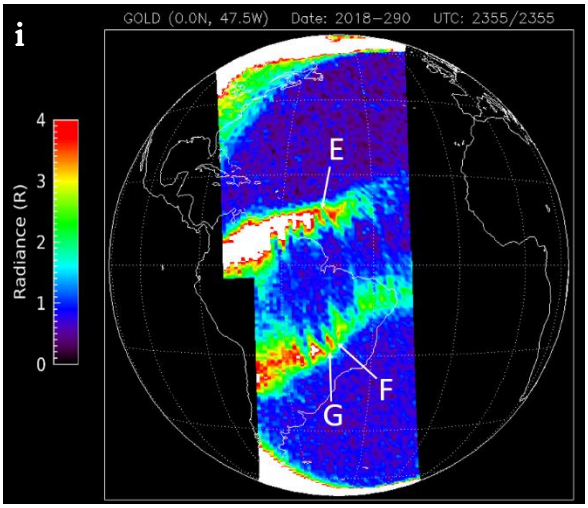

Figure 36: GOLD images showing plasma bubbles labeled A-G, for comparison to those simulated by the SAMI3 model. White represents regions of greater than 4 Rayleigh brightness. Features were artificially smoothed along magnetic field meridians. Our focus will be on plasma bubbles seen in high plasma density region of the Equatorial Ionization Anomaly. The other bright spots in the polar regions are due to the aurora or parts of the image still on the dayside of the terminator.

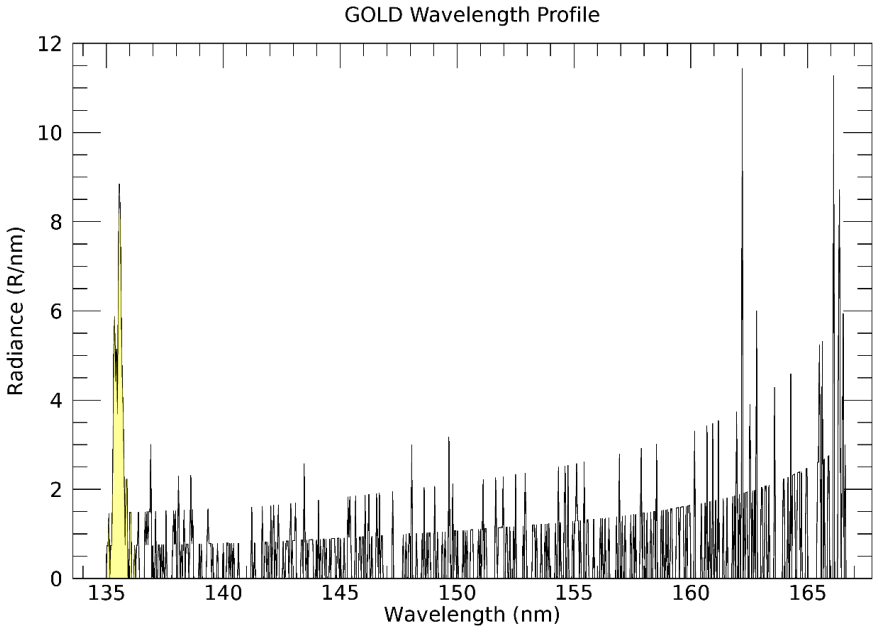

Figure 37: Example GOLD wavelength profile, showing the wavelengths used in image integration highlighted in yellow. The units of the data were Rayleighs per width of each wavelength bin in nanometers (nm). The average wavelength bin is 0.04 nm wide.

4.2 SAMI3 Comparison Geometry

To accurately compare the measured metrics from the SAMI3 model output simulations to GOLD data, we will sample the simulated bubble from GOLD's perspective. For this simulation we will

use the SAMI3 model output during solar maximum and solar minimum conditions. A cross-section at 0° latitude of the model used for solar maximum conditions can be seen in Figure 19 and that for solar minimum conditions can be seen in Figure 33. The vantage point is the same as GOLD's for this simulation, except it is geo-synchronous orbit at 0° longitude, because the plasma bubble in our model is centered at 0° longitude and 0° latitude. The resulting images from the SAMI3 model output during solar maximum and solar minimum conditions from GOLD's vantage point are shown in Figure 38. A cross-section of the northern and southern ends of the bubble in brightness, along with the measured metrics from this perspective can be seen in Figure 39.

We will define the quantitative metrics used to compare bubbles the same as in Section 2.4. Cross-section profiles of the bubbles in latitude-longitude space are taken as the average of three rows of pixels, roughly equal to the latitude averaged across during the original simulation and in Chapter 3. Plasma bubble width is considered the region of the bubble below a 30% drop in brightness relative to ambient plasma brightness. The relative brightness drop across the bubble will also be calculated similarly, as the mean brightness in the middle of the plasma bubble over the mean ambient plasma brightness. GOLD employs a variable pixel size when imaging which does not greatly affect the measured size and depletion of the bubble, but can have an impact and complicate the measured gradient at the bubble walls (Eastes et al., 2017). Therefore, the gradients at the bubble walls will not be compared and we will only look at the overall size and intensity of the bubble to authenticate our simulations. The starkly different vantage points and image capture methods are not conducive to accurately compare gradients observed at the bubble walls.

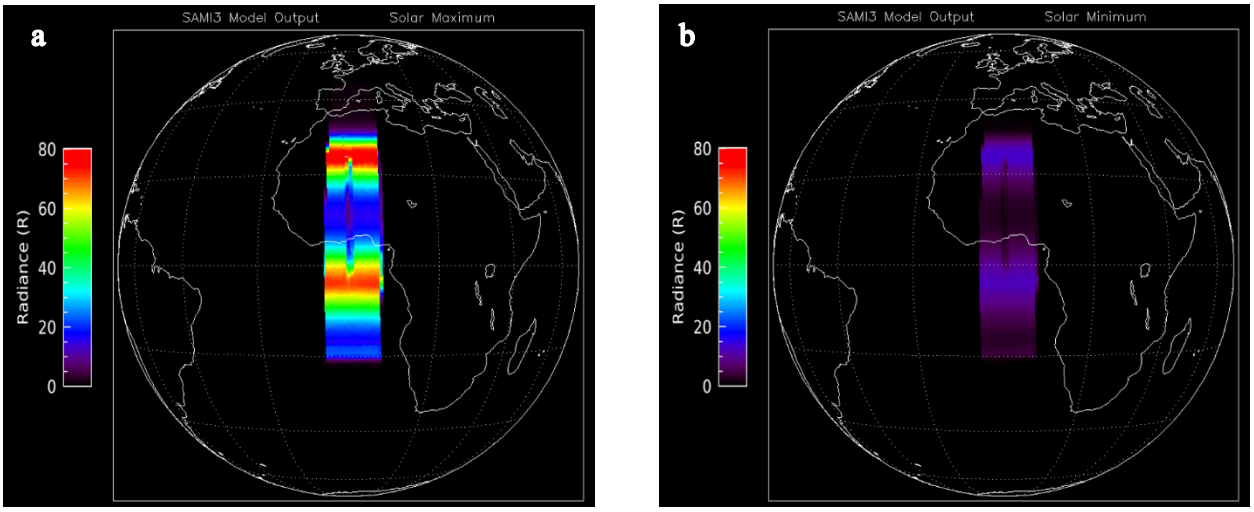

Figure 38: Plasma bubble from SAMI3 model output seen from GOLD perspective over 0° latitude and 0° longitude. a) Solar maximum conditions and b) Solar minimum conditions. Note the color scale is different from actual GOLD data, however both images in this figure on the same color scale.

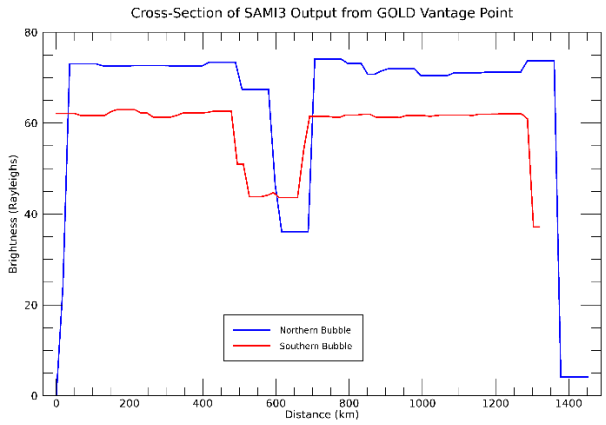

	Width (km)	Rel. Brightness Drop (%)
Northern Bubble	90.38	50.29
Southern Bubble	131.62	29.35
Original Simulation	119.0	62.11

Figure 39: Cross-section of SAMI3 model output seen from GOLD's prospective. The northern and southern cross-sections of the plasma bubble are from the solar maximum case. The original simulation case is idealized TDI values from the Section 2.4

In the original simulation of observing the SAMI3 model output from ICON's perspective, the spacecraft is on the equator observing the northern end of the plasma bubble. The measured width of the northern end of the bubble from GOLD's perspective is smaller, at 90.38 km, than that measured in the original simulation. However, the measured width of the southern end of the bubble is larger, at 131.62 km, than the original simulation. This suggests that the bubble is wider on the southern end than the northern end and from ICON's perspective the change in width might become obscured to produce a larger appearing bubble while looking north from the equator. The measured relative brightness drop across the bubble in the original simulation is slightly larger than when the northern end of the bubble is observed from GOLD's perspective. This could also be due to the difference in perspective, since ICON's view might measure a higher ambient plasma brightness since it has a larger viewing zenith angle.

4.3 Comparison of Results

The width of the plasma bubble and relative brightness drop across the bubble from the SAMI3 simulation will be compared to plasma bubbles seen in GOLD data to evaluate our models used in previous simulations in Chapter 2 and 3. Metrics for each bubble in the GOLD data set will be the average of the measured metrics for each image that the bubble appears in. The measured width and relative brightness drop across the bubble for plasma bubbles in the GOLD data set are shown in Table 7. The widths of the plasma bubbles range from 80 km to 259 km, with an average of 151 km and a standard deviation of 64 km. The relative brightness drop across the bubbles ranges from 45% to 57%, with an average of 50% and a standard deviation of 3.6%. This shows that plasma bubbles currently seen in the ionosphere can have a wide variety of sizes, but a fairly consistent depletion inside the bubble, around 50%.

	Width (km)	Relative Brightness Drop (%)	Geodetic Longitude (°E)	Magnetic Longitude (°E)
Bubble A	177.28	53.65	343.64	59.53
Bubble A'	189.38	48.76	346.58	59.46
Bubble B	215.43	48.73	339.80	55.98
Bubble B'	92.27	48.43	343.39	55.99
Bubble C	227.16	46.13	334.65	51.02
Bubble C'	125.90	46.92	338.99	51.16
Bubble D	259.07	57.17	329.44	46.49
Bubble D'	118.24	49.94	334.91	46.49
Bubble E	98.42	53.00	308.81	25.67
Bubble F	80.41	45.41	311.11	20.36
Bubble G	85.44	51.98	308.90	18.08
Average	151.73	50.01	---	---
Standard Dev.	64.02	3.59	---	---

Table 7: Measured characteristics of plasma bubbles observed from GOLD on the night of October 17th, 2018. Geodetic and magnetic longitudes represent approximate average longitude of each bubble in the first image they appear in with their geomagnetic conjugate if they have one.

These observed bubbles are similar to the SAMI3 model output used in the original simulation. The true plasma bubble width in the original simulation, at 116.95 km, is smaller than the average observed plasma bubble width but still in the range of observed widths. The relative brightness drop across the bubble in the original simulation, at 58.4 percent, is slightly above the range of observed brightness drops on this night of the GOLD data set, but still within the range of previously observed percentage depletions in plasma bubbles (Tsunoda, 1980). Therefore, the original simulation used an accurate representation of the size and intensity of a plasma bubble currently seen in the ionosphere. The maximum brightness observed in Figure 38b under solar minimum conditions in our SAMI3 model output was 13.63 Rayleighs and the maximum brightness observed in the equatorial region in the GOLD data set was 7.91 Rayleighs. Current conditions are near solar minimum and this is a reduction in brightness of 41.9% from our model, however, our solar minimum simulation still represents a good approximation of the conditions in the ionosphere during low solar activity. In our half-width bubble simulation, the true plasma bubble width was 61.20 km and the relative brightness drop across the bubble was 58.13 percent. The width of the bubble is slightly lower than what we observe in the GOLD data set and the relative brightness drop across the bubble is slightly above the range of observed depletions in the GOLD data set. This makes our half-width simulation on the narrow end of plasma bubbles, but still a reasonable bubble width to test the capabilities of the TDI technique with.

5 Conclusions

The use of airglow emissions to study plasma depletions has been implemented on many spacecraft missions before. These missions have imaged a variety of different wavelengths of airglow and across all imaging techniques it could be assumed that the observed scene is either not moving throughout image integration or each pixel in the image is moving at a constant angular rate with respect to the spacecraft. However, due to several factors of ICON's orbital geometry, the spacecraft moves nearly 96 km and the observed scene incurs a non-uniform motion blur throughout image integration. The non-uniformity of the motion blur is due to the assumption that each pixel in the image is moving at a constant angular rate does not hold. This is because the distance from the spacecraft to the assumed region of emission for each pixel in every image varies by over a factor of three across the image. For these reasons a novel variable-range time-delay integration technique was developed that was originally described in Wilkins et al., 2017.

The variable-range time-delay integration technique works by transforming each raw image onto a surface where the spacecraft moves at a constant angular rate with respect to every pixel in the image. Then a traditional time-delay integration technique can be applied to offset raw image frames throughout image integration. This thesis investigated the capabilities of the variable-range time-delay integration technique to spatially resolve plasma depletions through a series of simulations of viewing plasma depletions from ICON's FUV imager. Additionally, a code was developed to post-process images created using this algorithm and correct for assumptions, used during image integration, about Earth's shape and the position and orientation of ICON's FUV instrument. The following conclusions were drawn:

- The variable-range time-delay integration process used onboard ICON was recreated successfully and verified using simulated checker-board pattern images following the process described by Wilkins et al., (2017) where the TDI process was originally developed.
- The simulation of viewing a plasma bubble from SAMI3 model output showed the TDI technique can spatially resolve the structuring, location, and some quantitative metrics of the observed bubble.
- Shot noise was added to the simulation and some of the fine structuring was lost, however, the overall characteristics of the bubble were still recoverable and the true values were within the range of the uncertainty in the measurements.
- The half-width plasma bubble simulation revealed the TDI technique can detect and measure plasma bubbles that are on the narrow end of the range typically seen, however the measured full depth of the depletion in brightness is slightly diminished and the sharp gradients seen at either wall of the bubble were not recoverable for very narrow bubbles.

- The positive turret view-angle simulation showed that when the turret of ICON's FUV imager is misaligned with the magnetic field meridian, the measured width and relative brightness drop across the bubbles will decrease slightly in magnitude and the uncertainty in the measurements will increase. The measured gradients at the bubble walls were unaffected by this misalignment.
- The solar minimum conditions simulation confirmed that during low solar activity, the width and depth of depletion of plasma bubbles are still measurable, but the uncertainty in the measurements is increased. The noise associated with the observations at low solar activity levels can mask brightness gradients at the bubble walls.
- Images from the GOLD mission support that the parameters used in the four simulations are reasonable approximations of the range of plasma bubbles and ionospheric conditions currently seen in the upper atmosphere.
- A code was written to process L1 data files from ICON and produce an L2 data file containing all pertinent information about the geometry and geodetic coordinates of plasma bubbles seen by the FUV instrument onboard ICON.

The ability of the variable-range time-delay integration technique to spatially resolve structures of the nighttime ionosphere and the location of plasma depletions, when the assumption of uniform motion blur throughout image integration does not hold, allows for this technique to be used on future missions with similar imaging constraints. Future work would also include application of the post-processing code to data from ICON when it becomes available and investigation into the plasma depletions observed.

Bibliography

Adeniyi, J. O., Bilitza, D., Radicella, S. M., & Willoughby, A. A. (2003). Equatorial F2-peak parameters in the IRI model. *Advances in Space Research*, *31*(3), 507–512. https://doi.org/10.1016/S0273-1177(03)00039-5

Barth, C. A., & Schaffner, S. (1970). Ogo 4 spectrometer measurements of the tropical ultraviolet airglow. *Journal of Geophysical Research*, *75*(22), 4299–4306. https://doi.org/10.1029/JA075i022p04299

Berkner, L. V., & Wells, H. W. (1934). F-region ionosphere-investigations at low latitudes. *Terrestrial Magnetism and Atmospheric Electricity*, *39*(3), 215–230. https://doi.org/10.1029/TE039i003p00215

Chapman, S. (1931). The absorption and dissociative or ionizing effect of monochromatic radiation in an atmosphere on a rotating earth. *Proceedings of the Physical Society*, *43*(1), 26–45. https://doi.org/10.1088/0959-5309/43/1/305

Comberiate, J. M., Kamalabadi, F., & Paxton, L. J. (2007). A tomographic model for ionospheric imaging with the Global Ultraviolet Imager. *Radio Science*, *42*(2). https://doi.org/10.1029/2005RS003348

Comberiate, J., & Paxton, L. J. (2010). Coordinated UV imaging of equatorial plasma bubbles using TIMED/GUVI and DMSP/SSUSI. *Space Weather*, *8*(10), 1–9. https://doi.org/10.1029/2009SW000546

DeMajistre, R., Paxton, L. J., Morrison, D., Yee, J. H., Goncharenko, L. P., & Christensen, A. B. (2004). Retrievals of nighttime electron density from Thermosphere Ionosphere Mesosphere Energetics and Dynamics (TIMED) mission Global Ultraviolet Imager (GUVI) measurements. *Journal of Geophysical Research*, *109*(A5). https://doi.org/10.1029/2003JA010296

Dungey, J. W. (1956). Convective diffusion in the equatorial F region. *Journal of Atmospheric and Terrestrial Physics*, *9*(5), 304–310. https://doi.org/10.1016/0021-9169(56)90148-9

Eastes, R. W., McClintock, W. E., Burns, A. G., Anderson, D. N., Andersson, L., Codrescu, M., … Oberheide, J. (2017). The Global-Scale Observations of the Limb and Disk (GOLD) Mission. *Space Science Reviews*, *212*(1), 383–408. https://doi.org/10.1007/s11214-017-0392-2

England, S. L., Immel, T. J., & Huba, J. D. (2008). Modeling the longitudinal variation in the post-sunset far-ultraviolet OI airglow using the SAMI2 model. *Journal of Geophysical Research: Space Physics*, *113*(A1). https://doi.org/10.1029/2007JA012536

Farley, D. T., Bonelli, E., Fejer, B. G., & Larsen, M. F. (1986). The prereversal enhancement of the zonal electric field in the equatorial ionosphere. *Journal of Geophysical Research: Space Physics*, *91*(A12), 13723–13728. https://doi.org/10.1029/JA091iA12p13723

Fejer, B. G., & Kelley, M. C. (1980). Ionospheric irregularities. *Reviews of Geophysics*, *18*(2), 401. https://doi.org/10.1029/RG018i002p00401

Fejer, B. G., de Paula, E. R., González, S. A., & Woodman, R. F. (1991). Average vertical and zonal F region plasma drifts over Jicamarca. *Journal of Geophysical Research: Space Physics*, *96*(A8), 13901–13906. https://doi.org/10.1029/91JA01171

Frey, H. U., Mende, S. B., Immel, T. J., Gérard, J.-C., Hubert, B., Habraken, S., … Shematovich, V. I. (2003). Summary of Quantitative Interpretation of IMAGE Far Ultraviolet Auroral Data. In J. L. Burch (Ed.), *Magnetospheric Imaging — The Image Prime Mission* (pp. 255–283). Dordrecht: Springer Netherlands. https://doi.org/10.1007/978-94-010-0027-7_11

Hargreaves, J. K. (1992). *The solar-terrestrial environment : an introduction to geospace–the science of the terrestrial upper atmosphere, ionosphere, and magnetosphere*. Cambridge [England] ;

New York, NY, USA : Cambridge University Press. Retrieved from https://trove.nla.gov.au/version/24813388
Heelis, R. A., Kendall, P. C., Moffett, R. J., Windle, D. W., & Rishbeth, H. (1974). Electrical coupling of the E- and F-regions and its effect on F-region drifts and winds. *Planetary and Space Science*, *22*(5), 743–756. https://doi.org/10.1016/0032-0633(74)90144-5
Hei, M. A., Heelis, R. A., & McClure, J. P. (2005). Seasonal and longitudinal variation of large-scale topside equatorial plasma depletions. *Journal of Geophysical Research: Space Physics*, *110*(A12). https://doi.org/10.1029/2005JA011153
Hey, J. S., Parsons, S. J., & Phillips, J. W. (1946). Fluctuations in Cosmic Radiation at Radio-Frequencies. *Nature*, *158*(4007), 234. https://doi.org/10.1038/158234a0
Huba, J. D., Joyce, G., & Krall, J. (2008). Three-dimensional equatorial spread F modeling. *Geophysical Research Letters*, *35*(10). https://doi.org/10.1029/2008GL033509
Hysell, D. L. (1999). Imaging coherent backscatter radar studies of equatorial spread F. *Journal of Atmospheric and Solar-Terrestrial Physics*, *61*(9), 701–716. https://doi.org/10.1016/S1364-6826(99)00020-6
Hysell, D. L. (2000). An overview and synthesis of plasma irregularities in equatorial spread F. *Journal of Atmospheric and Solar-Terrestrial Physics*, *62*(12), 1037–1056. https://doi.org/10.1016/S1364-6826(00)00095-X
Immel, T. J., England, S. L., Mende, S. B., Heelis, R. A., Englert, C. R., Edelstein, J., … Sirk, M. M. (2017). The Ionospheric Connection Explorer Mission: Mission Goals and Design. *Space Science Reviews*, *214*(1), 13. https://doi.org/10.1007/s11214-017-0449-2
Immel, T. J., Frey, H. U., Mende, S. B., & Sagawa, E. (2004). Global observations of the zonal drift speed of equatorial ionospheric plasma bubbles. *Annales Geophysicae*, *22*(9), 3099–3107.
Immel, T. J., Mende, S. B., Frey, H. U., Peticolas, L. M., & Sagawa, E. (2003). Determination of low latitude plasma drift speeds from FUV images. *Geophysical Research Letters*, *30*(18). https://doi.org/10.1029/2003GL017573
Kelley, M. C. (2009) *The Earth's Ionosphere: Plasma Physics and Electrodynamics.* Burlington, MA: Elsevier Inc.
Kelley, M. C., Larsen, M. F., LaHoz, C., & McClure, J. P. (1981). Gravity wave initiation of equatorial spread F: A case study. *Journal of Geophysical Research*, *86*(A11), 9087. https://doi.org/10.1029/JA086iA11p09087
Kelley, M. C., Makela, J. J., Paxton, L. J., Kamalabadi, F., Comberiate, J. M., & Kil, H. (2003). The first coordinated ground- and space-based optical observations of equatorial plasma bubbles. *Geophysical Research Letters*, *30*(14). https://doi.org/10.1029/2003GL017301
Kil, H., Su, S.-Y., Paxton, L. J., Wolven, B. C., Zhang, Y., Morrison, D., & Yeh, H. C. (2004). Coincident equatorial bubble detection by TIMED/GUVI and ROCSAT-1. *Geophysical Research Letters*, *31*(3). https://doi.org/10.1029/2003GL018696
King, J. W., & Kohl, H. (1965). Upper Atmospheric Winds and Ionospheric Drifts Caused by Neutral Air Pressure Gradients. *Nature*, *206*(4985), 699–701. https://doi.org/10.1038/206699a0
Makela, J. J. (2006). A review of imaging low-latitude ionospheric irregularity processes. *Journal of Atmospheric and Solar-Terrestrial Physics*, *68*(13), 1441–1458. https://doi.org/10.1016/j.jastp.2005.04.014
Meier, R. R. (1991). Ultraviolet spectroscopy and remote sensing of the upper atmosphere. *Space Science Reviews*, *58*(1), 1–185. https://doi.org/10.1007/BF01206000

Meier, R. R., Picone, J. M., Drob, D., Bishop, J., Emmert, J. T., Lean, J. L., … Gibson, S. T. (2015). Remote Sensing of Earth's Limb by TIMED/GUVI: Retrieval of thermospheric composition and temperature. *Earth and Space Science*, *2*(1), 1–37. https://doi.org/10.1002/2014EA000035

Mende, S. B., Frey, H. U., Rider, K., Chou, C., Harris, S. E., Siegmund, O. H. W., … Ellis, S. (2017). The Far Ultra-Violet Imager on the Icon Mission. *Space Science Reviews*, *212*(1–2), 655–696. https://doi.org/10.1007/s11214-017-0386-0

Mendillo, M., & Baumgardner, J. (1982). Airglow characteristics of equatorial plasma depletions. *Journal of Geophysical Research: Space Physics*, *87*(A9), 7641–7652. https://doi.org/10.1029/JA087iA09p07641

Mendillo, M., & Tyler, A. (1983). Geometry of depleted plasma regions in the equatorial ionosphere. *Journal of Geophysical Research: Space Physics*, *88*(A7), 5778–5782. https://doi.org/10.1029/JA088iA07p05778

Ott, E. (1978). Theory of Rayleigh-Taylor bubbles in the equatorial ionosphere. *Journal of Geophysical Research: Space Physics*, *83*(A5), 2066–2070. https://doi.org/10.1029/JA083iA05p02066

Park, S. H., England, S. L., Immel, T. J., Frey, H. U., & Mende, S. B. (2007). A method for determining the drift velocity of plasma depletions in the equatorial ionosphere using far-ultraviolet spacecraft observations. *Journal of Geophysical Research: Space Physics*, *112*(A11). https://doi.org/10.1029/2007JA012327

Rishbeth, H. (1971a). The F region dynamo. *Planet. Space Sci*., *19*, 263-267.

Rishbeth, H. (1971b). Polarization fields produced by winds in the equatorial F-region. *Planetary and Space Science*, *19*(3), 357–369. https://doi.org/10.1016/0032-0633(71)90098-5

Sagawa, E., Immel, T. J., Frey, H. U., & Mende, S. B. (2005). Longitudinal structure of the equatorial anomaly in the nighttime ionosphere observed by IMAGE/FUV. *Journal of Geophysical Research: Space Physics*, *110*(A11). https://doi.org/10.1029/2004JA010848

Sahai, Y., Fagundes, P. R., & Bittencourt, J. A. (2000). Transequatorial F-region ionospheric plasma bubbles: solar cycle effects. *Journal of Atmospheric and Solar-Terrestrial Physics*, *62*(15), 1377–1383. https://doi.org/10.1016/S1364-6826(00)00179-6

SSUSI Data Products Algorithms. (2013) *The Johns Hopkins University Applied Physics Laboratory*.

Strickland, D. J., Evans, J. S., & Paxton, L. J. (1995). Satellite remote sensing of thermospheric O/N2 and solar EUV: 1. Theory. *Journal of Geophysical Research: Space Physics*, *100*(A7), 12217–12226. https://doi.org/10.1029/95JA00574

Su, S.-Y., Chao, C. K., & Liu, C. H. (2008). On monthly/seasonal/longitudinal variations of equatorial irregularity occurrences and their relationship with the postsunset vertical drift velocities: ESF IRREGULARITIES AND VERTICAL DRIFTS. *Journal of Geophysical Research: Space Physics*, *113*(A5), n/a-n/a. https://doi.org/10.1029/2007JA012809

Sultan, P. J. (1996). Linear theory and modeling of the Rayleigh-Taylor instability leading to the occurrence of equatorial spread F. *Journal of Geophysical Research: Space Physics*, *101*(A12), 26875–26891. https://doi.org/10.1029/96JA00682

Tsunoda, R. T. (1980). Magnetic-field-aligned characteristics of plasma bubbles in the nighttime equatorial ionosphere. *Journal of Atmospheric and Terrestrial Physics*, *42*(8), 743–752. https://doi.org/10.1016/0021-9169(80)90057-4

Tsunoda, R. T., Livingston, R. C., McClure, J. P., & Hanson, W. B. (1982). Equatorial plasma bubbles: Vertically elongated wedges from the bottomside *F* layer. *Journal of Geophysical Research*, *87*(A11), 9171. https://doi.org/10.1029/JA087iA11p09171

U.S. Standard Atmosphere, 1976. (1976). Retrieved from https://ntrs.nasa.gov/search.jsp?R=19770009539

Weber, E. J., Buchau, J., Eather, R. H., & Mende, S. B. (1978). North-south aligned equatorial airglow depletions. *Journal of Geophysical Research: Space Physics*, *83*(A2), 712–716. https://doi.org/10.1029/JA083iA02p00712

Wilkins, C. W., Mende, S. B., Frey, H. U., & England, S. L. (2017). Time-delay integration imaging with ICON's Far-Ultraviolet spectrograph. *Space Sci. Rev*.

Zalesak, S. T., Ossakow, S. L., & Chaturvedi, P. K. (1982). Nonlinear equatorial spread F: The effect of neutral winds and background Pedersen conductivity. *Journal of Geophysical Research: Space Physics*, *87*(A1), 151–166. https://doi.org/10.1029/JA087iA01p00151